INTERNATIONAL ATOMIC ENERGY AGENCY
UNITED NATIONS EDUCATIONAL, SCIENTIFIC AND CULTURAL ORGANIZATION

INTERNATIONAL CENTRE FOR THEORETICAL PHYSICS
34100 TRIESTE (ITALY) - P.O.B. 586 - MIRAMARE - STRADA COSTIERA 11 - TELEPHONE: 2240-1
CABLE: CENTRATOM - TELEX 460892-1

H4.SMR/204 - 34

WINTER COLLEGE ON

ATOMIC AND MOLECULAR PHYSICS

(9 March - 3 April 1987)

CHEMICAL PROCESSING WITH LASERS

R. Kullmer

Johannes-Kepler-Universitat Linz
Linz, Osterreich
Austria

Laser - Induced Chemical Processing

- Fundamentals : (1) – (6)

- Examples : Deposition (7)
  Etching
  Surface Modification

Literature :

D. J. Ehrlich, J. Y. Tsao :
J. Vac. Sci. Techn. B1, p 969 (1983)

T. J. Chuang : Surface Science Repl.
3, p. 1 (1983)

H.H. Gilgen et al. : Appl. Phys.
A37, p. 121 (1985)

D. Bäuerle : Chemical Processing
with Lasers
Springer Verlag 1986

Conventional Laser Processing

- pure heat treatment
  → melting, evaporation

- chemically non-reactive environment
  → limits of definition :
  - laser machining in air
  - alloying

- high power lasers : CO_2, Nd : YAG

Advantages of LCP:

→ compared to standard CVD:
- single step process
- contamination is avoided
- not well suited for mass production
  → complementary technique
    - semi-custom IC's
    - repair of IC's
    - repair of photomasks
    - changes during development

→ heating can be restricted or even be eliminated

→ high heating / cooling rates

→ not restricted to planar substrates

→ selective non-thermal excitation schemes by tuning the laser wavelength

③ Determination of temperature for pyrolytic processes

→ large area processing:
pyroelectric thin films

→ localized heating:
thermal deflection
deposition, etching ?

→ pyrometric detection of emitted heat radiation:
emissivity ?
temperature gradients ?
change in surface structure during processing ?
fast process ?

→ steady growth of rods

→ calculation ?

④ · Temperature Calculations

→ heat equation:

$$\frac{\kappa(T)}{D_t(T)} \cdot \frac{\partial T}{\partial t} - \nabla(\kappa(T)\,\nabla T) = Q$$

$$D_t(T) = \frac{\kappa(T)}{\varrho \cdot c}$$

→ Kirchhoff transform:

$$\vartheta(T) = \vartheta(T_0) + \int_{T_0}^{T} \frac{\kappa(T')}{\kappa(T_0')}\, dT'$$

$$\rightarrow \frac{1}{D_t(T(\vartheta))} \frac{\partial \vartheta}{\partial t} - \nabla^2 \vartheta = \frac{Q}{\kappa(T_0)}$$

→ moving substrate / laser spot:

$$\frac{v_s}{D_t(T(\vartheta))} \frac{\partial \vartheta}{\partial x} - \nabla^2 \vartheta = \frac{Q}{\kappa(T_0)}$$

→ source term Q:

$$Q = \frac{2P(1-R)}{\pi \omega_0^2} \cdot \exp\left(-\frac{2r^2}{\omega_0^2}\right) \cdot f(z)$$

→ constant α:

$$f(z) = \alpha \cdot \exp(-\alpha z)$$

High absorption

→ $\alpha > 10^4\ cm^{-1}$ → $f(z) = \delta(z)$

$$\rightarrow \vartheta = \frac{\sqrt{2}\,P(1-R)}{\pi\sqrt{\pi}\,\kappa(T_0)\,\omega_0} \cdot \int_0^\infty g(u)\,du$$

$$g(u) = \frac{1}{1+u^2} \cdot \exp\left\{-2\left[\frac{(X+V_X u^2)^2 + Y^2}{1+u^2} + \frac{Z^2}{u^2}\right]\right\}$$

$$X = \frac{x}{\omega_0}\ ,\ Y = \frac{y}{\omega_0}\ ,\ Z = \frac{z}{\omega_0}$$

$$V = \frac{v_s}{\omega_0}$$

$$\chi(T(\vartheta)) = \frac{\omega_0^2}{8\sqrt{2}\,D_t(T(\vartheta))}$$

$$R = R(T(\vartheta))$$

→ static case: $v_s = 0$

→ $R = R(T_0)$, $\kappa = \kappa(T_0)$

$$T_c = T_0 + \frac{P(1-R)}{\sqrt{2\pi}\,\kappa(T_0)\,\omega_0}$$

silicon, $P = 0.575\,W$, $2\omega_0 = 5\mu m$, $T_0 = 300K$

→ $T_c = 700K$

→ $R = R(T_0)$, $\kappa = \kappa(T)$

silicon: $\kappa(T) = \frac{293\,W/cm}{T - 93K}$

→ $T_c = 1650\,K$

→ $R = R(T)$, $\kappa = \kappa(T)$

→ dynamic case: CW irradiation, $v_s \neq 0$

- $v_s < 10$ mm/sec

  ⇒ $T_c \approx T_c(v_s = 0)$

- $v_s > 1$ m/sec

  ⇒ T_c drops with increasing v_s

→ dynamic case: pulsed irradiation, $v_s = 0$

- rectangular temporal pulse profile
  gaussian beam
  $R = R(T_0)$, $\mu = \mu(T_0)$
- heating phase:

$$T_c = T_0 + \frac{\sqrt{2}\, P(1-R)}{\pi^{3/2} \mu(T_0)\, \omega_0} \cdot \arctan \gamma$$

$$\gamma = \frac{2\sqrt{2 D_0 \cdot t}}{\omega_0}$$

- cooling phase:

$$T_c = T_0 + \frac{\sqrt{2}\, P(1-R)}{\pi^{3/2} \mu(T_0)\, \omega_0} \cdot \left(\arctan \frac{\gamma - \zeta}{1 + \gamma\zeta} \right)$$

$$\zeta = \frac{2\sqrt{2 D_0 (t-\tau)}}{\omega_0}$$

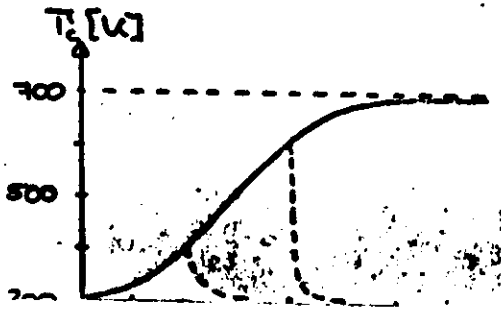

silicon,
same parameters
(Piglmayer et al.)

→ finite absorption:

- $f(z) = \alpha \cdot \exp(-\alpha z)$
- $\alpha = \alpha(T) = \alpha(T(z))$

$$f(z) = \alpha(T(z)) \cdot \exp\left\{ - \int_0^z \alpha(T(z'))\, dz' \right\}$$

silicon: $\alpha(T) = 5.02 \cdot 10^3 \text{cm}^{-1} \cdot \exp\left(\frac{T}{430\,\text{K}}\right)$

- dynamic feedback
- pulsed irradiation of silicon

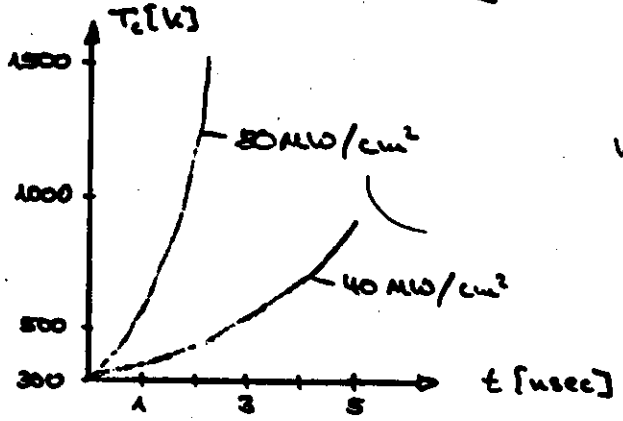

Kwong et al.

$\Phi_m = 0.20$ J/cm² $\quad I = 100$ MW/cm²

$= 0.42$ J/cm² $\quad = 20$ MW/cm²

⑤ Photolytic Processes

→ direct breaking of chemical bonds by laser light

- in the substrate
  - → electron - hole pair generation in semiconductors
- in the gas phase
  - → dissociative electronic excitation
  - → multiphoton vibrational excitation
- in the adsorbate - substrate system
  - → formation of reaction products
  - → desorption of reaction products
  - → dissociation of adsorbed species

Dissociative Electronic Excitations

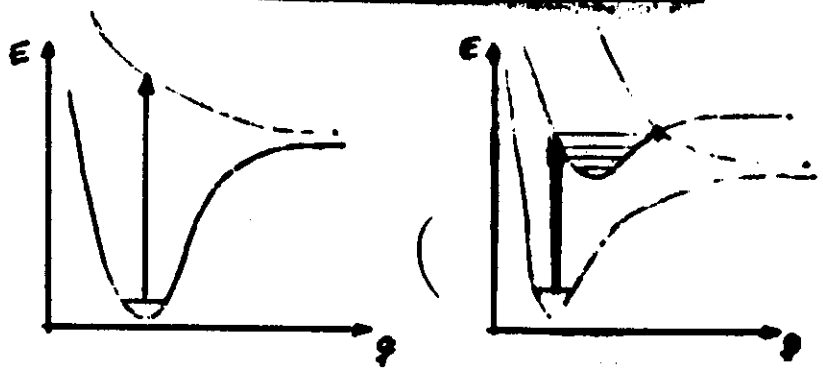

→ in most cases relevant for LCP: near UV light
- excimer laser
- SHG Ar^+ laser, SHG dye laser
- THG, FHG Nd:YAG

→ dissociation of adsorbed molecules: wavelength shift

→ $Me(CH_3)_m$ Me = Cd, Al, Zn → metal deposition
$Me(CO)_m$ Me = Cr, Fe, Mo, W, Ni

→ halides, halogen containing compounds:
Cl_2, Br_2, COF_2, SF_6, XeF_2, ... → etching

→ hydrides:
AsH_3, B_2H_6, PH_3 → doping
$SiH_4 + NO_2$ → SiO_2 deposition

→ $Ga(CH_3)_3$
$P(CH_3)_3$
$Zn(CH_3)_2$
$(CH_3)_2InP(CH_3)_2$ → deposition of compound semiconductors

Infrared Vibrational Excitations

→ stepwise multiphoton excitation

→ problems: thermalization
anharmonicity

→ high power lasers: CO_2 laser
parallel incidence

→ few examples of a real photolytic process (no gas phase heating)

$SF_6 + h\nu \rightarrow SF^*$

$SF_6^* + Si \rightarrow$ etching (Chuang et al.)

Consecutive reaction steps:

- transport of reactants into the reaction volume
- adsorption of reactants on the surface
- pyrolytic or photolytic activation of the system
- transport of product atoms // molecules to the surface, possible recombination or secondary reactions on the way
- condensation of product atoms / molecules on the surface, possible further reactions
- desorption of reaction products
- transport of reaction products out of the reaction volume

Adsorbed Layers

→ chemisorption : $E_B = 0.5 \ldots 5\,eV$

physisorption : $E_B = 0.05 \ldots 0.5\,eV$

→ adsorbate - substrate system in vacuum

- pyrolytic activation:

$$\omega \sim N_{ad}(T(r,t)) \cdot \exp\left(-\frac{\Delta E}{RT(r,t)}\right)$$

- photolytic activation:

$$\omega \sim N_{ad}(T_0) \cdot \frac{\sigma_{ad} \cdot p}{\hbar\omega\,(\omega_0^2)} \cdot \exp\left(-\frac{z-z^2}{\omega_0^2}\right)$$

→ adsorbate - substrate system in equilibrium with the gas phase

$$N_{ad}(p,T) = \vartheta(p,T) \cdot N_L$$

ϑ : surface coverage

Gas - Solid - Interactions

Kinetically Controlled Regime

→ pyrolytic LCP:

$$\omega = A \cdot k_0(p_i,T) \cdot \exp\left(-\frac{\Delta E}{R \cdot T(r,t)}\right)$$

- flat structures:

$$h(r,t_i) = A \int_{t_n}^{t_i} dt\; k_0(p_i,T) \cdot \exp\left(-\frac{\Delta E}{RT(r,t)}\right)$$

- comparison to standard CVD
  - higher temperatures and / or gas pressures possible
  - three - dimensional flow of reactants and reaction products

⇒ higher deposition rates

→ photolytic LCP:

- cylindrical symmetry : $z_0 = \frac{\pi \omega_0^2}{\lambda} \gg \omega_0$

  → density of excited reactants:

  $$s = \frac{N_0 \cdot \sigma_R}{h\nu} \cdot I(r')$$

- reactant flux to the surface

  $$\Rightarrow \omega(r) = B \cdot \frac{s N_0 \sigma_R P}{h\nu\, \omega_0^2} \cdot \int dy' \int dz' \int r' dr' \frac{z'}{d^3(r, r', y', z')} \cdot \exp\left(-\frac{2r'^2}{\omega_0^2}\right)$$

  $$\omega(r=0) = B \cdot \frac{s N_0 \sigma_R P}{h\nu\, \omega_0}$$

- recombination, collisional deactivation ?

Mass Transport Limited Region

→ hemispherical geometry

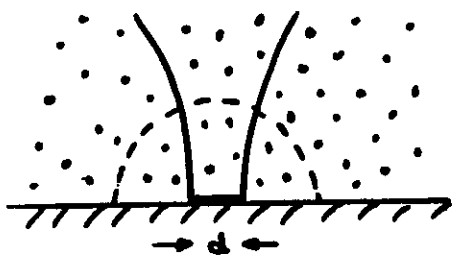

→ surface flux :

$$j(t) = \frac{2D \cdot c_\infty}{r_0 + d} \left\{ 1 + \frac{d}{r_0} \cdot \exp\left(\frac{t}{\tau_0}\right) \cdot \operatorname{erfc}\sqrt{\frac{t}{\tau_0}} \right\}$$

$$\tau_0 = \left(4D\left(\frac{1}{r_0} + \frac{1}{d}\right)\right)^{-1}$$

$$r_0 = \frac{4D}{\gamma' v_m}$$

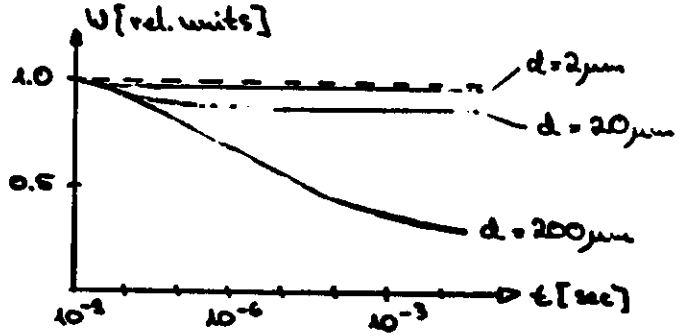

(Eveliche et al.

→ steady-state surface flux:

$$j(t \to \infty) = \frac{2D n_\infty}{r_0 + d}$$

$r_0 \sim D$, $D \sim \frac{1}{p}$] $d \ll r_0$: $j \sim p$

$d \gg r_0$: $j \to$ const.

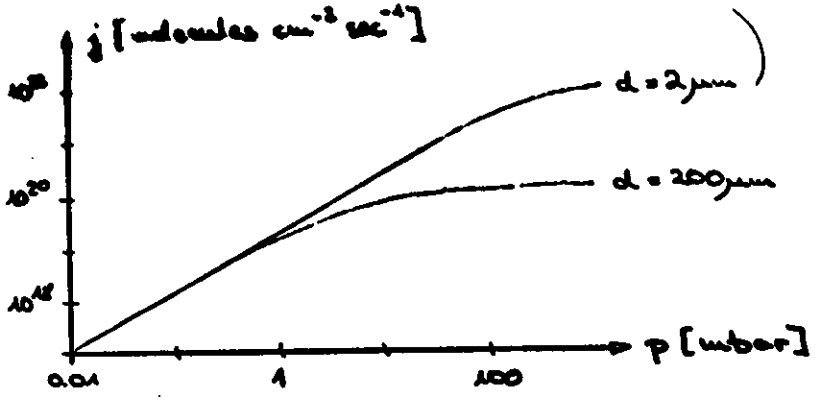

(Ehrlich et al.)

→ $j \geq 10^{22}$ molecules $cm^{-2} sec^{-1}$

→ ω on the order of several mm/sec

Spatial Resolution

→ gaussian beam:

$$2\omega_0 = \frac{4 \cdot f \cdot \lambda}{\pi \cdot a}$$

$\frac{f}{a} = 1.5 \Rightarrow 2\omega_0 \approx 2 \cdot \lambda$

$\lambda = 500$ nm $\Rightarrow 2\omega_0 = 1\,\mu m$

→ nonlinearities in pyrolytic LCP

→ photolytic LCP:

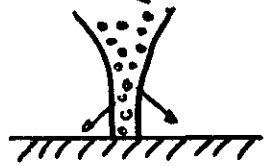

diffusion of reactants → buffer gas

→ nucleation sites generated photolytically by dissociation of adsorbates

→ photoexcitation of a semiconductor: diffusion of electron-hole pairs

4. Experimental Techniques

This chapter is intended to give an overview of the main experimental components and aspects of LCP. Section 4.1 describes different experimental setups for laser microchemical and large-area chemical processing. Section 4.2 comments on lasers that are typically used in LCP. Techniques of measuring deposition and etch rates are outlined in Sect.4.3. Section 4.4 briefly describes different possibilities of in situ temperature measurements.

4.1 Typical Setups

The main components of an experimental setup for LCP consist of a laser and a reaction chamber. The latter contains the reactive species and the substrate. The laser light can be incident perpendicular and/or parallel to the surface of the substrate [4.1,2]. The reaction chamber is often operated with a constant flow of the reacting gaseous or liquid species with or without a carrier. In microchemical processing, the reaction chamber can be sealed off in many cases, because of the small amount of species consumed in most of the reactions.

For microchemical processing, the laser beam, in general a cw laser (Sect.4.2), is expanded and then focused at normal incidence onto the substrate surface. A typical setup is shown schematically in Fig.4.1. Laser beam illumination times are electronically controlled with an electrooptical modulator. The eyepiece is used for direct observation of patterns. The position of the objective is optically and electronically controlled (autofocus). Direct writing of micrometer-sized surface patterns is accomplished by translating the substrate perpendicular to the focused laser beam (Fig.4.2a).

Large-area processing can be performed with an experimental arrangement that, apart from some changes in the optics, is similar to that shown in Fig.4.1. The main difference is that the laser beam is scanned over the

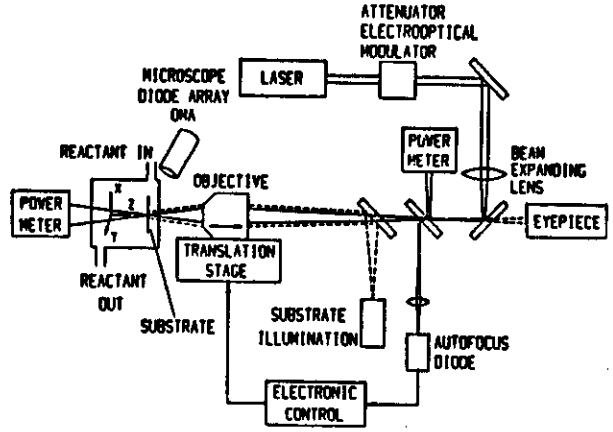

Fig.4.1. Schematic of a typical experimental setup for microchemical processing. The substrate is mounted on an xyz stage. The position of the objective is optically and electrically controlled (autofocus). The eyepiece (or a TV camera together with a monitor) is used for direct observation of patterns

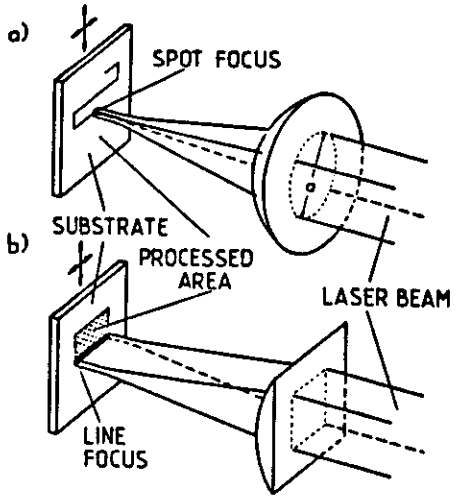

Fig.4.2. Schematic showing the focusing in microchemical (a) and large-area chemical (b) processing in perpendicular configuration (after [4.1])

substrate either unfocused or defocused or focused to a line by means of a cylindrical lens (Fig.4.2b). Another type of experimental setup used in large-area processing is shown in Fig.4.3. Here, a collimated beam is passed, at a certain distance, parallel to the surface of the substrate. Combined parallel and perpendicular irradiation is achieved either by directing the emerging beam onto the surface of the substrate in an arrangement as shown in

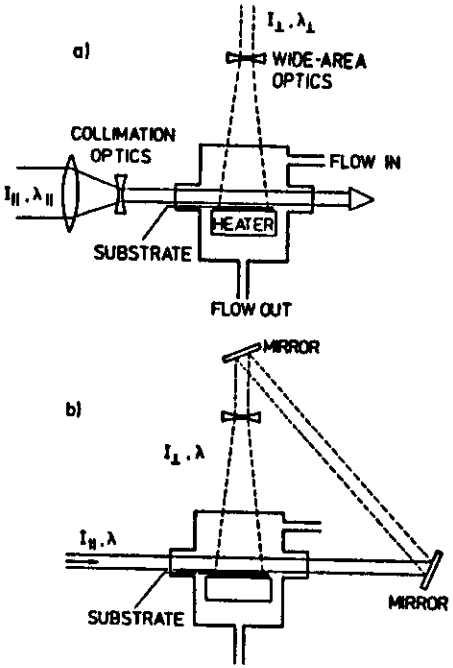

Fig.4.3. Optics for parallel (beams shown by solid lines) and combined parallel/perpendicular (beams shown by solid and dashed lines) laser irradiation used in large-area chemical processing

Fig.4.3b, or by using two lasers, perhaps at different wavelengths. In the latter case, one can separately optimize homogeneous and heterogeneous pyrolytic and/or photolytic reactions by proper selections of $I_\parallel$, $\lambda_\parallel$ and $I_\perp$, $\lambda_\perp$, respectively.

In laser-enhanced electrochemical plating (etching), the substrate is negatively (positively) biased with respect to a counterelectrode [4.3.4]. The applied voltages are typically 1-2 V. Figure 4.4 shows an apparatus for laser-enhanced jet-plating, which is the most recent development in this area. In this technique, the mass transport to the substrate is increasec by a jet (typical flow velocities are 10^3 cm/s). The laser beam (in most experiments an Ar^+ or Kr^+ laser was used) is focused at the center of the orifice of the jet and is maintained within the liquid column by total internal reflection until impingement on the cathode occurs. In these experiments, the potentiostat is set to deliver constant current, i.e. to plate galvanostatically. In earlier experiments, not using a jet, the substrate was immersed within the liquid electrolyte. Here, the laser beam was directed either through the electrolyte to directly illuminate the electrolyte-substrate interface from the front or, in the case of transparent substrates coated with metal on one side, through the substrate to illuminate

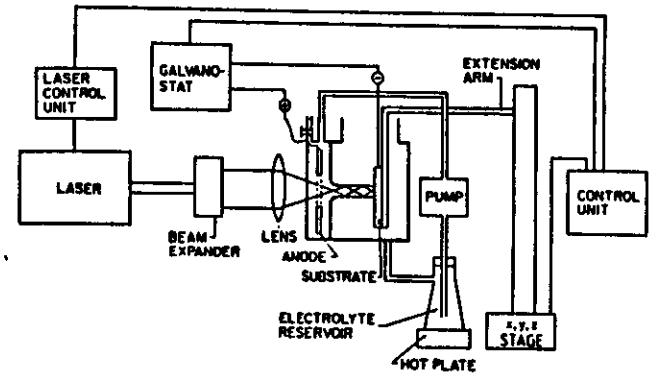

Fig.4.4. Experimental setup for laser-induced electrochemical jet-plating. The laser beam is focused approximately at the center of the jet orifice. The substrate can be moved via the extension arm (after [4.3])

the metal layer from the rear only. These initial experiments simply used a dropping resistor to measure the current flow with and without laser beam illumination. Both continuous and pulsed plating (etching) were demonstrated by modulating the external voltage source, the laser output power, or both synchronously. Both, Ar^+ and Kr^+ lasers were used with power densities ranging from 10^2 to 10^6 W/cm^2. The plating (etching) mechanisms and experimental results are described in Sects.3.3 and 5.2.3, respectively.

4.2 Lasers

The lasers that are most commonly used in LCP are listed in Table 4.1, together with some of their characteristic features. Micrometer-sized structures are mainly produced with cw lasers, such as Ar^+ or Kr^+ lasers, including frequency-doubled lines. The reason is the tight focusability and good stability of such lasers with respect to the beam profile and the output power. These are prior conditions in direct writing of microstructures with constant and well-defined morphology (Sect.5.2). The TEM_{00} mode, which has been used in most of the experiments, is of Gaussian shape. Then, the incident laser irradiance within the focal plane can be written in the form

$$I(r) = I(0)\exp(-2r^2/w_0^2) , \qquad (4.1)$$

where w_0 is defined by $I(w_0) = I(0)/e^2$ and is given by approximately (see, for example, [4.5-7])

the damage to materials - from ion or electron bombardment or from overall vacuum ultraviolet radiation - which is inherent to conventional low-temperature techniques such as plasma processing and ion- or electron-beam processing. Laser processing is, of course, not limited to planar substrates and allows three-dimensional fabrication as well.

The present book concentrates on the new field of laser-induced chemical processing of materials as defined just above. As already mentioned in the Preface, the intention is to give scientists, engineers and manufacturers an overview of the extent to which the technique is understood at present, and of the various possibilities and limitations it has.

Determining the scope of this book was, naturally, very difficult and in some cases somewhat arbitrary. For example, we have paid little or no attention to problems related to laser machining taking place in air, where oxidation or nitridation reactions may play an important role as well. Furthermore, laser-induced structural transformations, or laser alloying, are often accompanied by a precipitation of new compounds within the surface of the material, and such cases could equally well be incorporated into the book. We also exclude the wide field of homogeneous laser photochemistry. Here, the basic interaction mechanisms between molecules and laser light are investigated, and materials are produced homogeneously in the gas or liquid phase [1.45-50]. Sometimes such reactions also take place in the presence of solid surfaces that catalyze the laser-induced reaction. Finally, no medical applications have been included, even though these tend to be based on mainly photothermal or photochemical reactions, in the same way as the cases discussed in this book [1.51-55].

The book is divided into nine chapters. Chapters 2 and 3 are devoted to the fundamental mechanisms in pyrolytic and photolytic chemical processing and to the kinetics of laser-induced chemical reactions at or near solid surfaces. Experimental techniques are briefly described in Chap.4. Chapter 5 outlines laser-assisted deposition of materials in the form of microstructures and thin extended films. Laser-induced surface modifications are described in Chap.6. The formation of stoichiometric compounds is covered in Chap.7. Chapter 8 deals with laser-induced chemical etching of materials. In Chap.9 actual and potential applications of LCP in micromechanics, microelectronis, integrated optics and chemical technology are summarized. The main abbreviations and symbols used throughout are listed at the end of the book.

2. Fundamental Excitation Mechanisms

Laser-induced chemical reactions can be based on several fundamentally different microscopic mechanisms. In the following we shall classify reactions into those which are governed by *mainly* pyrolytic (photothermal) or by *mainly* photolytic (photochemical) processes. We shall call a reaction pyrolytic if the thermalization of the laser excitation is fast compared to the reaction, and photolytic if this is not the case, i.e. when the constituents of the reaction are in nonequilibrium states. The laser excitation can take place within the ambient gaseous or liquid medium and/or directly within the surface of the solid material (substrate) to be processed. In many cases the different mechanisms and possibilities of excitation contribute simultaneously to the reaction, but often one of them dominates. There are also many examples where, for example, a reaction is initiated photolytically and proceeds pyrolytically, or vice versa.

In this chapter, we will outline a phenomenological treatment of laser-induced temperature distributions for semiinfinite substrates (Sect.2.1.1) and compare it to model structures that are relevant in LCP (Sect.2.1.2). Sections 2.2.1 and 2.2.2 deal with dissociative single-photon and multiphoton electronic excitations and with the dissociation of molecules by photosensitization. The fundamentals of selective infrared vibrational excitations are outlined in Sect.2.2.3.

2.1 Pyrolytic Processing

In pyrolytic laser-induced chemical processing, the laser serves as a heat source and gives rise to thermochemistry. The absorbed laser light may heat either the substrate, or the ambient gaseous or liquid medium, or both. High temperatures are reached, e.g. by one-photon absorption processes, if the frequency of the laser light matches a strong vibrational absorption in a particular molecule, or any optically active elementary excitation in the solid. In solids or in single, isolated polyatomic molecules, this excitation

molecular densities used in LCP, randomization of energy *between* single molecules occurs via collisional energy transfer, typically within 10^{-12} - 10^{-7} s. In spite of their thermal character, such laser-driven reactions may be very different from those traditionally initiated by a conventional heat source in which an equivalent amount of thermal energy is deposited. This is because of the much higher temperatures (~ 10^4 K) obtainable in the small reaction volume defined by a focused laser beam. Therefore, novel reaction products due to different reaction pathways may occur.

Single-step production of spatially well-defined structures is usually performed by local substrate heating using laser light that is *not* absorbed by the ambient gaseous or liquid medium. In this case the chemical reaction is essentially confined to the hot spot that is induced on the substrate by the absorbed laser light. Because of the large variety of optically active elementary excitations in solids, and because of the rapid dissipation of the excitation energy, it is clear that in the case of local substrate heating the dependence of the reaction rate on the frequency of the laser radiation is less pronounced than in the case of gas-phase heating mentioned above.

A quantitative analysis of pyrolytic processing based on local substrate heating requires a detailed knowledge of the laser-induced temperature distributions. Direct temperature measurements have been performed with a reliable degree of accuracy in only a very few cases. In many cases the measurement techniques (Sect.4.4) cannot be satisfactorily applied for practical reasons, and so a method of calculating the laser-induced temperatures is desirable. In fact, many features in pyrolytic processing can be qualitatively and in some cases even quantitatively understood from calculated temperature distributions.

The temperature distribution induced by the absorbed laser light depends on the absorption coefficient $\alpha(\lambda,T)$ within the processed area, on the transport of heat, which is determined by the thermal diffusivity $D_t(T)$, on chemical reaction energies (exothermal or endothermal), and on transformation energies for crystallization, melting, boiling, etc., where relevant. Here, λ is the laser wavelength and $T(r,t)$ the laser-induced temperature distribution, which is a function of both the distance r from the center of the beam and of the time t. Note, however, that in laser-induced chemical processing, the quantities α and D_t do *not* refer just to the substrate material. In fact, these quantities are strongly changed by the deposition, surface modification, compound formation or etching process itself [2.1-6]. Let us consider this, for example, in the case of laser-induced deposition

from the gas phase when the substrate and the laser beam are static. Before nucleation takes place, α and D_t refer to the substrate. However, when nucleation commences, these quantities will change rapidly with the density of the nuclei and therefore with time. When a compact film is formed, e.g. a metal film, and if the penetration depth of the laser light is smaller than the film thickness, α will refer only to this deposited film. Similarly, the thermal conductivity will be quite different for such a combined structure and for a simple homogeneous plane substrate. The situation is very similar in laser-induced compound formation and etching.

We will now discuss these problems in greater detail and compare laser-induced temperature distributions on semiinfinite substrates with those induced on structures that are relevant in laser-induced chemical processing.

2.1.1 Semiinfinite Substrates

Temperature distributions induced on semiinfinite substrates have been calculated for static and scanned cw [2.1,2,5,7-18] and pulsed [2.12-16,23-26] laser beams. Similar calculations have also been performed for semiinfinite multilayer structures [2.27,28]. Here, in many cases, analytic solutions are possible. In the following we will outline some of the essential features for cw laser and pulsed laser heating of solids. Continuous-wave laser heating is the predominant mode in laser-induced microchemical processing, while pulsed laser heating is mainly applied for large-area chemical processing and for projection patterning (Sect.4.2).

In the following analysis we shall consider the flow of heat by conduction into the bulk of a material irradiated by a slowly moving laser beam. Heat losses into the surrounding medium by thermal conduction, convection, or blackbody radiation are not taken into consideration. The temperature distribution induced by the absorbed laser light can be calculated from the heat equation, which can be written as

$$\frac{\kappa(T)}{D_t(T)}\,\frac{\partial T}{\partial t} - \nabla[\kappa(T)\nabla T] = Q \,. \qquad (2.1)$$

Here, $\kappa(T)$ and $D_t(T)$ are the temperature-dependent thermal conductivity and thermal diffusivity of the irradiated material. The thermal diffusivity is given by $D_t(T) = \kappa(T)/\rho_m c_p$, where ρ_m is the mass density and c_p the specific heat at constant pressure. The term Q is the source term arising from the incident laser light. The temperature-dependent thermal conductivity $\kappa(T)$ can be eliminated from the heat equation by performing a Kirchhoff transform [2.29]. The Kirchhoff transform requires the introduction of a linearized

temperature θ, which is defined as

$$\theta(T) = \theta(T_0) + \int_{T_0}^{T} \frac{\kappa(T')}{\kappa(T_0)}\, dT' \,, \tag{2.2}$$

where $\theta(T_0)$ is a constant, and T_0 the temperature at infinity. In terms of the linearized temperature, the heat equation can be written as

$$\frac{1}{D_t(T(\theta))}\,\frac{\partial\theta}{\partial t} - \nabla^2\theta = \frac{Q}{\kappa(T_0)} \,. \tag{2.3}$$

In a reference frame that is moving with the laser beam, say in x-direction, and in which the temperature distribution is stationary, the heat equation becomes

$$\frac{v_s}{D_t(T(\theta))}\,\frac{\partial\theta}{\partial x} - \nabla^2\theta = \frac{Q}{\kappa(T_0)} \,, \tag{2.4}$$

where v_s is the velocity of the substrate relative to the reference frame. For a Gaussian beam at normal incidence to the substrate, Q is given by

$$Q = \frac{2P(1-R)}{\pi w_0^2}\exp(-2r^2/w_0^2) f(z) \quad \text{with} \tag{2.5}$$

$$f(z) = \alpha \exp(-\alpha z) \,, \tag{2.6}$$

if α is constant. P is the incident laser power, R the reflectivity of the substrate, and $2w_0$ the diameter of the laser focus (Sect.4.2). In the following we shall discuss various different approximations.

a) High Absorption

In the case of high absorption ($\alpha > 10^4$ cm^{-1}) with *no* appreciable light penetration into the material, the source term Q vanishes except at the irradiated surface, where it is given by the effective absorbed irradiance. This assumption holds, for example, for metals, and in good approximation also for Si for visible Ar^+ or Kr^+ laser light, especially at elevated temperatures (see below). In this case, we can write

$$f(z) = \delta(z) \,. \tag{2.6'}$$

Using the source term (2.5) together with (2.6'), the general solution of

(2.4) is obtained by a Green's function method [2.29]. It is given by

$$\theta = \frac{2^{1/2}\,P(1-R)}{\pi^{3/2}\,\kappa(T_0) w_0} \int_0^\infty g(u)\, du \,, \quad \text{where} \tag{2.7}$$

$$g(u) = (1+u^2)^{-1} \exp\left[-2\left[\frac{(X + v_x u^2)^2 + Y^2}{1+u^2} + \frac{Z^2}{u^2}\right]\right] \quad \text{with} \tag{2.8}$$

$$X = x/w_0,\ Y = y/w_0,\ Z = z/w_0,$$
$$v = v_s/w_0,\ x(T) = w_0^2/[8(2^{1/2})D_t]. \tag{2.9}$$

Because $T = T(\theta)$, and because R and D_t are temperature dependent for most materials, (2.7) is an implicit equation for the linearized temperature θ. The above treatment cannot be used, however, when D_t depends very strongly on temperature and when phase changes occur. In this case, a more complex formulation of the problem based on numerical methods is required.

We now compare calculated temperature distributions, still assuming $f(z) = \delta(z)$, for various different cases.

The Static Case

In the static case, i.e. for cw laser irradiation and $v_s = 0$, equation (2.7) no longer depends on the diffusivity D_t.

In the first approximation, we also neglect the temperature dependences of parameters. The assumption of a temperature independent thermal conductivity

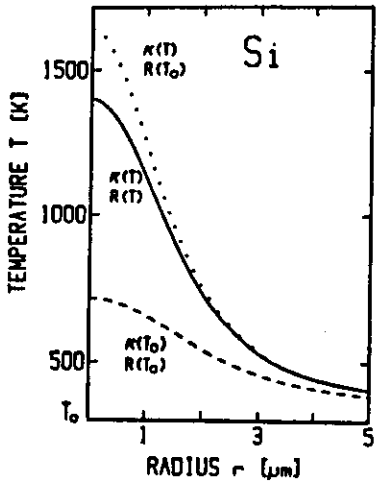

Fig.2.1. Temperature distribution induced by a static Gaussian laser beam at normal incidence. P = 0.575 W, $2w_0$ = 5 μm, T_0 = 300 K. The radius is measured from the center of the laser beam. The parameters correspond to Si. Dashed curve: $\kappa = \kappa(Si,T_0)$, $R = R(Si,T_0)$. Dotted curve: $\kappa = \kappa(Si,T)$, $R = R(Si,T_0)$. Full curve: $\kappa = \kappa(Si,T)$, $R = R(Si,T)$ (after [2.5])

greater than the Debye temperature. This follows from the Wiedemann-Franz law $\kappa = \pi^2 k_B^2 T\sigma/3e^2$ and the temperature dependence of the high temperature electrical conductivity $\sigma \sim T^{-1}$ [2.30]. The dashed curve in Fig.2.1, which is calculated from (2.7), applies to this case (note that for $\kappa = \text{const}(T)$ the temperatures θ and T are equal). In order to compare these results with those presented below, we have chosen values for the parameters which correspond to those of crystalline Si at room temperature. The maximum temperature rise in the center of the spot is

$$\Delta T_c = T_c - T_0 = \frac{P(1-R)}{(2\pi)^{1/2}\,\kappa(T_0)w_0}\,. \qquad (2.10)$$

Next, we take into account the temperature dependence of the thermal conductivity. For crystalline semiconductors and insulators, the high temperature thermal conductivity can be described, in many cases, by $\kappa \sim T^{-1}$. For Si, a fit to experimental data yields [2.31]

$$\kappa(T) = k(T - T_k)^{-1}; \quad k = 299\ \text{W/cm},\ T_k = 99\ \text{K}. \qquad (2.11)$$

With (2.2) and (2.7) the temperature can then be expressed analytically by

$$T(\vartheta) = T_k + (T_0 - T_k)\exp[\vartheta/(T_0 - T_k)]. \qquad (2.12)$$

The dotted curve in Fig.2.1 is calculated for this case.

Finally, we also consider the temperature dependence of the reflectivity. For Si, this temperature dependence can be approximated between room temperature and its melting point (1690 K) [2.18-22] by

$$R(T) = 0.324 + 4\cdot10^{-5}\,T \qquad (T < 1000\ \text{K}) \qquad (2.13a)$$

$$= 0.584 - 4.8\cdot10^{-4}\,T + 2.6\cdot10^{-7}\,T^2 \qquad (T > 1000\ \text{K})\,. \qquad (2.13b)$$

The full curve in Fig.2.1 applies to this case. The increase in reflectivity with temperature reduces the temperature at the center of the irradiated zone by approximately 13%.

The Dynamic Case

We are now interested in the influence of the *scanning* velocity on the temperature distribution. This can be calculated from (2.7) and (2.2) as long as D_t is independent or only slightly dependent on temperature. This assumption is invalid for Si, for which the thermal diffusivity depends strongly on temperature and can be approximated by [2.31]

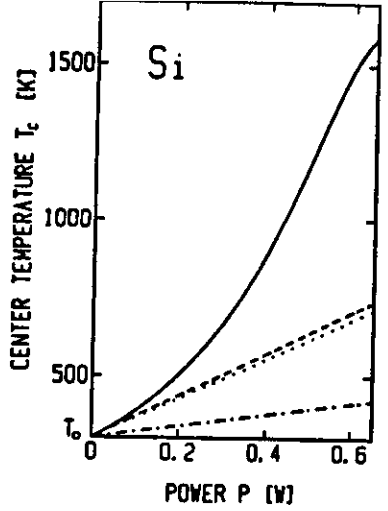

Fig.2.2. Laser-induced center temperature T_c as a function of laser power for different scanning velocities. $2w_0 = 5\ \mu m$, $T_0 = 300$ K. Dashed curve: $v_s = 0$. Dotted curve: $v_s = 1$ m/s. Dash-dotted curve: $v_s = 100$ m/s. In all three cases $\kappa = \kappa(Si,T_0)$, $R = R(Si,T_0)$, $D_t = D_t(Si,1680\ K)$. The full curve was calculated for $v_s = 0$ and $\kappa = \kappa(Si,T)$ and $R = R(Si,T)$ (after [2.5])

$$D_t(T) = d(T - T_d)^{-1}; \quad d = 128\ \text{cm}^2\text{K/s},\ T_d = 159\ \text{K}\,. \qquad (2.14)$$

In such a case, a numerical solution of the heat equation must be employed. For simplicity, however, we shall confine ourselves to an upper estimate and take the value for the diffusivity near the melting point of Si, i.e. $D_t = D_t(Si,1680\ K)$, instead of (2.14). Figure 2.2 shows the center temperature as a function of laser power for different scanning velocities v_s (dashed, dotted and dash-dotted curves). It becomes evident from the figure that in solid-phase processing such as laser annealing [2.33-40] or laser synthesis (Chap.7), where scanning velocities of up to several meters per second are common, the influence of the scanning velocity on the center temperature must be taken into account. On the other hand, in processing cases where $v_s < 10^4$ μm/s, the center temperature is essentially unaffected by v_s. The latter approximation also holds in direct writing of patterns by LCVD, if $\kappa_D/\kappa_S = 1$ (Sect.2.1.2). The full curve in Fig.2.2 shows the dependence of the center temperature for $v_s = 0$, but for temperature-dependent $\kappa(T)$ and $R(T)$.

For *pulsed* laser irradiation, an approach similar to that presented at the beginning of this section can be made for $v_s = 0$. Assuming again a Gaussian beam profile and no light penetration into the solid, i.e. $f(z) = \delta(z)$, a simple integration of the Green's function allows one to obtain the center temperature rise at the surface, i.e. the rise for $r = 0$ and $z = 0$. For temperature independent parameters and radial heat flow, this temperature rise can be written as

$$\Delta T_c = \frac{2^{1/2}\,P(1-R)}{\pi^{3/2}\,\kappa\,w_0}\,\arctan\,\gamma \qquad (2.15)$$

with $\gamma \equiv 2(2D_t t)^{1/2}/w_0$ and $t < \tau$; t is the time from the beginning of the (rectangular) pulse and τ is the pulse duration. For $\gamma \ll 1$, i.e. for very short times t, (2.15) yields

$$\Delta T_c = \frac{4P(1-R)t^{1/2}}{\pi(\pi\kappa\rho\, c_p)^{1/2}\,w_0^{\,2}}\,, \qquad (2.16)$$

while for very long times (2.15) approaches the limit (2.10). The cooling cycle can be described, in the same approximation as (2.15), by

$$\Delta T_c = \frac{2^{1/2}\,P(1-R)}{\pi^{3/2}\,\kappa w_0}\,\arctan\left(\frac{\gamma-\zeta}{1+\gamma\zeta}\right) \qquad (2.17)$$

with $\zeta = 2[2D_t(t-\tau)]^{1/2}/w_0$ and $t > \tau$.

Figure 2.3 shows the evolution of the normalized center temperature for the heating (full curve) and cooling (dashed curves) cycle and for different laser pulse lengths τ. Figure 2.4 shows the radial temperature distribution for various laser beam illumination times.

Fig. 2.3

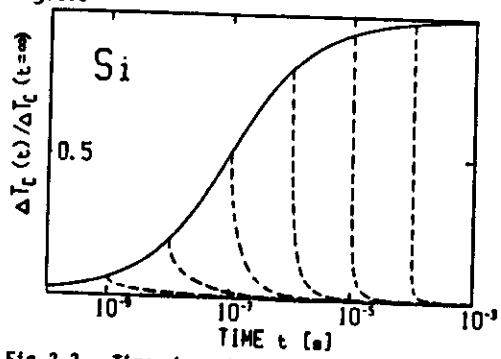

Fig. 2.4

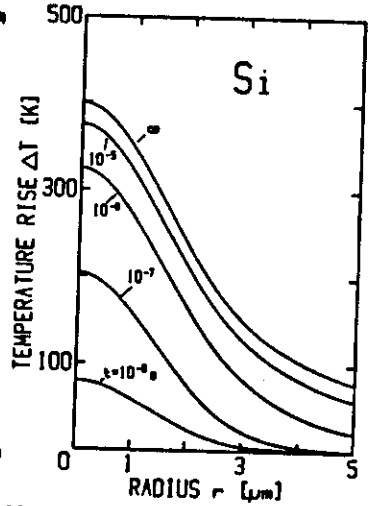

Fig. 2.3. Time dependence of the increase (full curve) and decrease (dashed curves) in center temperature rise normalized to the value for continuous irradiation ($t = \infty$). $P = 0.6$ W, $2w_0 = 5$ μm, $T_0 = 300$ K, $\kappa = \kappa(Si,T_0)$, $R = R(Si,T_0)$, $D_t = D_t(Si,1680\ K)$ (after [2.5])

Fig. 2.4. Distribution of temperature rise for various durations of laser light irradiation. $P = 0.6$ W, $2w_0 = 5$ μm, $T_0 = 300$ K, $\kappa = \kappa(Si,T_0)$, $R = R(Si,T_0)$, $v_s = 0$ (after [2.5])

b) Finite Absorption

Modeling the laser-induced temperature rise is a little more complicated in cases where the laser light has a finite penetration depth and where the function $f(z)$, which enters the source term Q, must be described by $f(z) = \alpha \exp(-\alpha z)$ instead of by a delta function. The situation becomes even more complicated when the absorption coefficient α is not a constant but a strong function of temperature. This is the case for Si. Here, the absorption coefficient for photon energies below 3 eV, i.e. above about 410 nm, increases exponentially with temperature and can be fitted, within the range $300\ K < T < 1000\ K$ [2.41-43] by

$$\alpha(T) = \alpha_0 \exp(T/T_R)\,. \qquad (2.18)$$

The parameters α_0 and T_R are listed in Table 2.1. Because of the drastic increase of absorption coefficent with temperature, the penetration depth α^{-1} shrinks rapidly, and this effect is even further increased by the decrease in $D_t(T)$ with increasing temperature, see (2.14).

Let us consider this in more detail for CO_2 laser and visible laser radiation. At 300 K, the infrared light of a CO_2 laser ($\lambda \sim 10$ μm, corresponding to a photon energy of about 0.12 eV) is only weakly absorbed in pure crystalline Si (c-Si; note that we frequently denote crystalline Si simply by Si, while amorphous Si is always denoted by a-Si), which has a band

Table 2.1. Parameters determining the temperature dependence of the absorption coefficent (2.18) for Si

λ [nm]	α_0 [$10^3\,cm^{-1}$]	T_R [K]	Ref.
10000	2×10^{-5}	110	[2.42]
694	1.34	427	[2.41]
633	2.08	447	[2.41]
532	5.02	430	[2.41]
515	6.28	433	[2.41]
488	9.07	438	[2.41]
485	9.31	434	[2.41]
458	14.5	429	[2.41]
405	55.1	420	[2.41]
308	1400 ($T \leq 1100$ K) 1800 ($T > 1100$ K)	4545	[2.43]

gap of about 1.1 eV at this temperature. In undoped material the absorption coefficient can be as low as 0.3 cm^{-1} (300 K), but it can rise to more than 10^3 cm^{-1} (300 K) in heavily doped c-Si. The absorption is due to the excitation of free carriers in the conduction band. The excitation energy is transferred rapidly to the lattice via electron-phonon scattering mechanisms, which are extremely fast, typically of the order of 10^{-12} to 10^{-13} s. As a result, the lattice is locally heated, even at low to medium laser irradiances, and the absorption coefficient thereby increases according to (2.18). Simultaneously, $D_t(T)$ is decreased. This dynamic feedback due to the coupling of the optical absorption and thermal conduction rapidly increases the heating rate.

When one uses visible laser radiation, electron-hole pairs are generated. In this case, the time for energy transfer to the lattice depends strongly on carrier density, doping level, defect density, etc., and varies, typically, from 10^{-13} to 10^{-6} s. In most laser processing situations, however, recombination by Auger processes can occur, and the time of energy transfer to the lattice is again very rapid, typically of the order of some picoseconds [2.44]. In other words, the situation is similar to that described for infrared radiation. For cw laser irradiation, a steady state between the supply and loss of energy within the irradiated region is obtained.

The effect of dynamic feedback is more pronounced for pulsed laser irradiation. A detailed theoretical treatment for Si and visible pulsed laser irradiation was devised by KWONG and KIM [2.23-26]. The calculations use a parametrized perturbation scheme and assume one-dimensional heat flow. The rapid increase in absorption and decrease in diffusivity with pulse duration is treated in terms of effective values. The main results are summarized in Figs.2.5 and 2.6. Figure 2.5 shows the rise in center temperature for different laser pulse intensities. At 10 MW/cm^2, the effective thermal diffusion time $\tau_D = 4\alpha_0^2 D_{to} t$ (α_0 and D_{to} are the effective values of the absorption coefficient and the thermal diffusivity, respectively) is long enough to increase the heated volume beyond the energy deposition depth α^{-1}. Therefore, the temperature rise near the surface is small. With increasing pulse intensity, that is with increasing heating rate, however, the reduction of D_{to} and the shrinking of α^{-1} confine the deposited energy more and more near the surface. Figure 2.6 shows the threshold laser energy for the onset of surface melting of Si as a function of pulse intensity for different laser wavelengths. At a wavelength of 694 nm and 20 MW/cm^2, for example, the energy needed to melt the Si surface is about 0.42 J/cm^2, while at 100 MW/cm^2 only

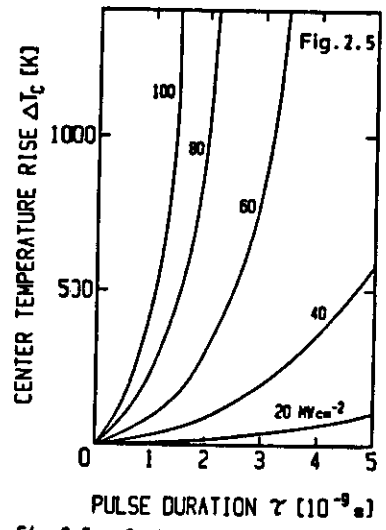

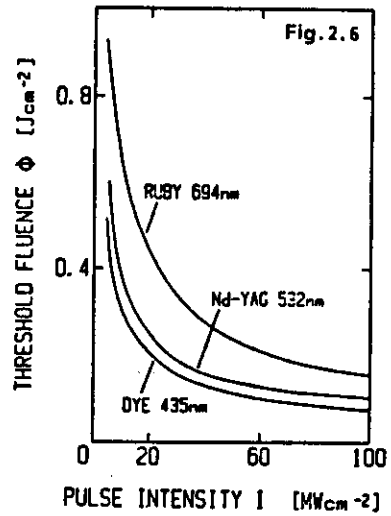

Fig.2.5. Center temperature rise for Si versus pulse duration for different pulse intensities at λ = 694 nm (after [2.23])

Fig.2.6. Threshold fluence for surface melting of Si versus pulse intensity for different laser wavelengths (after [2.23])

0.2 J/cm^2 are needed. The figure also shows the decrease in threshold pulse energy with decreasing wavelength. This effect is most pronounced in the low intensity region. It should be emphasized, however, that the calculations [2.23] did not incorporate the jump in surface reflectivity which occurs at the melting point. This may raise the threshold pulse energies for the onset of melting by a factor of approximately 2 relative to Fig.2.6.

2.1.2 Models for Deposition and Etching

As already mentioned at the beginning of this chapter, the calculation of temperature distributions for LCP is much more complicated than for the semiinfinite substrate: the temperature within the processed area will change strongly, even at constant laser irradiance, due to material parameter changes originating from the deposition, transformation or etching process itself. The essential features can be directly understood by comparing temperature distributions induced on semiinfinite substrates with those induced on structures that are relevant in LCP. Figures 2.7-9 show model structures for the deposition of circular spots, for direct writing of stripes, and for the etching of holes or grooves. For such structures,

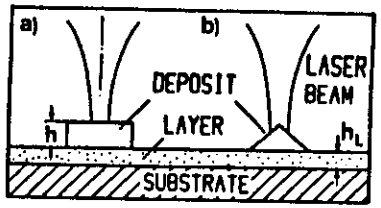

Fig.2.7

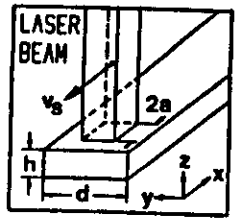

Fig.2.8

Fig.2.7a,b. Model structures for the deposition of spots. (a) circular cylinder (b) circular cone. The diameter of the spot at the substrate surface is d. An intermediate layer of thickness h_L is indicated

Fig.2.8. Model structure for steady growth of stripes. For simplicity, a rectangular laser beam with constant intensity has been assumed

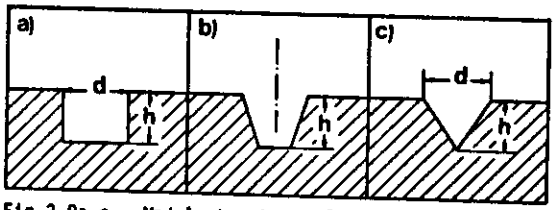

Fig.2.9a-c. Model structures for the etching of holes. Here, d is cefined as the width at the substrate surface

analytic solutions of the heat equation (2.1) are, in general, not possible. Therefore, numerical methods such as finite difference or finite element procedures must be employed [2.45,46]. The first calculations of this kind were performed by PIGLMAYER et al. [2.1-5]. The boundary conditions were similar to those used in the preceding section. The approximation was made that at sufficiently large distances from the irradiated surface, the temperature rise ΔT becomes radially symmetric with respect to the center of the laser spot.

Let us commence by simulating the deposition of circular *spots*. Here, we do not consider the problems in the phase of nucleation, as discussed in Sect.5.1, but assume that after a time t_m the semiinfinite plane substrate is already covered with a thin circular film of the deposited material within the area exposed to the focused laser beam. In Fig.2.7a, the deposit is represented by a circular disc of diameter d and height h. For greater generality, the semiinfinite substrate is assumed to be covered with a thin extended layer of thickness h_L. The thermal conductivities of the deposit, the thin layer and the substrate are κ_D, κ_L and κ_S. For simplicity we ignore the temperature dependence of these material parameters, and also heat losses to the gas phase and latent heat effects (heats of formation). The laser beam is assumed to be Gaussian and normally incident at the center of the deposit.

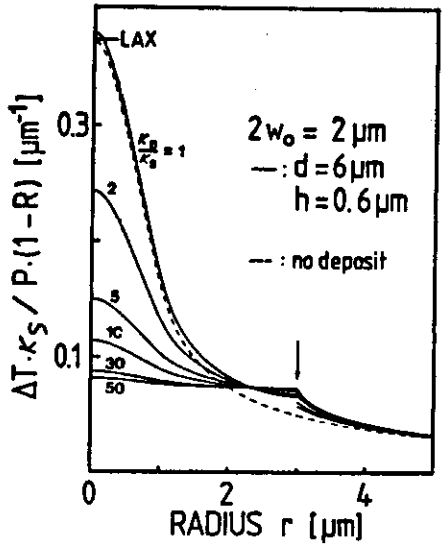

Fig.2.10. Laser-induced temperature distributions for a circular cylinder (Fig.2.7a) calculated for different ratios of thermal conductivities κ_D and κ_S. The arrow marks the edge of the disc. The dashed curve represents the temperature distribution for a semiinfinite substrate. The center temperature according to analytical calculations by LAX [2.7] is also marked (after [2.2])

First, we make the following further assumptions: the diameter of the disc is larger than the laser focus ($d > 2w_0$); no light penetrates into the deposit [$f(z) = \delta(z)$]; the thermal conductivities of the thin layer and the substrate are equal ($\kappa_L = \kappa_S$). Under these conditions, the temperature distribution can be calculated from (2.4,5) together with (2.6') and $v_s = 0$. The only difference from the semiinfinite substrate appears in the source term Q. Here, the reflectivity of the substrate must be replaced by the reflectivity of the deposited material, and the thermal conductivity now refers to both the substrate *and* the deposit, i.e. κ assumes the values κ_D and κ_S in the deposit and the substrate, respectively. Figure 2.10 shows the results of numerical calculations for various ratios of the thermal conductivities κ_D and κ_S ($d = 6$ μm, $h = 0.6$ μm, $2w_0 = 2$ μm). The edge of the deposit is indicated in the figure by the arrow. It can be seen from the figure that the center temperature scales approximately with κ_D/κ_S. This holds also for $\kappa_D < \kappa_S$, a case that under certain circumstances applies to Si deposition on Si substrates [see (2.11)]. For $\kappa_D = \kappa_S$, the temperature distribution within the deposit is close to that for the plane substrate (dashed curve); the center temperature taken from the analytical calculations by LAX [2.7] is indicated. Significant differences from the semiinfinite substrate occur only near the edge of the disc. With increasing κ_D/κ_S the temperature distribution on the disc flattens. In the limit $\kappa_D \gg \kappa_S$ the temperature is almost constant over the disc. This latter case applies, for

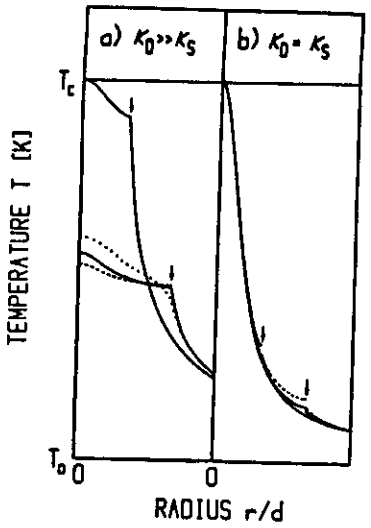

Fig.2.11a,b. Temperature distributions calculated for different geometries of circular deposits. The dotted curve refers to a circular cone (Fig.2.7b), all other curves to circular cylinders (Fig.2.7a). Arrows indicate edges of deposits. Full curves: h = d/20, $2w_o$ = d/3 (for the upper full curves the values for h and d are half as large as for the lower ones). Dashed curve: h = d/10, $2w_o$ = d/3. Dotted curve: h = d/20, $2w_o$ = d/3. (a) κ_D = 70 W/mK, κ_S = 1.3 W/mK; (b) $\kappa_D = \kappa_S$ = 70 W/mK. T_o = 300 K (after [2.1])

example, to metal deposits on insulating substrates. The temperature distribution outside of the deposit, i.e. for r > d/2, is only slightly influenced by the value of the ratio κ_D/κ_S.

Next, we consider temperature distributions for different geometries of circular deposits. They are shown in Figs.2.11a,b for two different ratios of thermal conductivities κ_D and κ_S. The value for κ_D corresponds to a typical metal such as Ni [κ_D(Ni) = 70 W/mK]. The substrates are glass [κ_S(glass) = 1.3 W/mK] and Si [κ_S(Si) = κ_D(Ni)] in Figs.2.11a and b, respectively. All curves except the dotted one refer to the model of the circular cylinder (Fig.2.7a). The dotted curve is the temperature profile for a circular cone (Fig.2.7b) with height h = d/20 (in Fig.2.11b the curves would be almost indistinguishable). Figure 2.11a shows that for constant spot diameter d, the temperature at the edge of the deposit, T(d/2), depends only very slightly on its geometry, i.e. on its height and exact shape (compare full, broken and dotted curves). Actually, if $\kappa_D \gg \kappa_S$, the temperature rise $\Delta T(d/2)$ scales approximately inversely with d (compare full curves) and can be described to a good approximation by the simple equation [2.29]

$$\Delta T(d/2) = P\,(1-R_D)/(2d\kappa_S)\ . \qquad (2.19)$$

It is therefore not surprising that $\Delta T(d/2)$ is not very sensitive to changes in κ_D as long as $\kappa_D \gg \kappa_S$; e.g., when we use a value of κ_D = 30 W/mK instead of κ_D = 70 W/mK, $\Delta T(d/2)$ decreases by only about 5%. In Fig.2.11b the

temperature distribution is nearly independent of the diameter, height and shape of the deposit and is very similar to that for a plane substrate; significant differences occur only near the edge of the deposit.

Figure 2.12 shows the influence of the laser focus on the temperature distribution for three different ratios of thermal conductivities κ_D, κ_L and κ_S. The values used for κ_D and κ_S are the same as those used in Figs.2.11a,b. Figure 2.12b represents an intermediate case where the Si substrate is covered with a layer of h_L = 4000 Å a-SiO_2 [$\kappa_L(SiO_2) = \kappa$(glass)]. The full curves were calculated for equal center temperature T_c = 530 K, which of course requires different absorbed laser powers, namely 10, 56 and 120 mW in cases a, b and c, respectively. A doubling (dash-dotted curves) of the laser focus changes the center temperature much more dramatically in b and c than in a. As long as d > $2w_o$, the temperature $\Delta T(d/2)$ at the edge of the deposit remains nearly unaffected in all three cases.

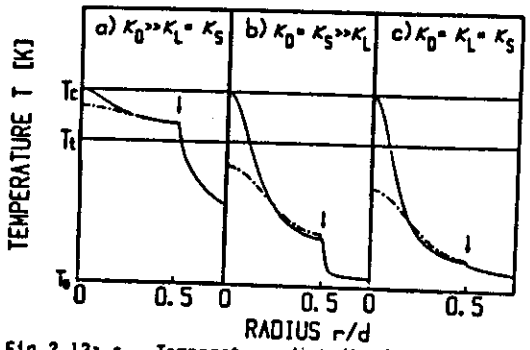

Fig.2.12a-c. Temperature distributions calculated for model structure shown in Fig.2.7a with three different ratios of thermal conductivities and two different radii of the laser focus. Full curves have been calculated for equal center temperature with h = d/20, $2w_o$ = d/3. Dash-dotted curves: h = d/20, $2w_o$ = 2d/3. Values for κ_D and κ_S correspond to those in Fig.2.11. h_L = 4000 Å, T_o = 300 K, T_c = 530 K. T_t schematically indicates a threshold temperature (after [2.1])

We now proceed to a model for *direct writing* (see Chap.5). The shape of the stripe, shown in Fig.2.8, has been chosen for mathematical convenience; for the same reason, the intensity of the incident beam is assumed in this case to be constant over its square cross section. Relative to the scanning beam the shape of the infinitely long stripe is taken to be static; in a reference frame where the laser beam and thereby the stripe are at rest the substrate moves with velocity v_s. Temperature profiles calculated for κ_D = $30\kappa_S$ and $\kappa_D = \kappa_S$ are shown in Fig.2.13. For $\kappa_D = \kappa_S$, the temperature

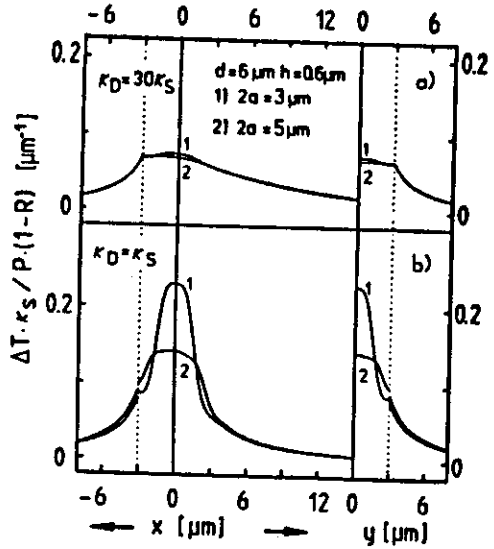

Fig.2.13. Calculated temperature distributions for stripes along the coordinate axes of the model structure shown in Fig.2.8. v_s/D_t < 0.5 µm^{-1} (after [2.2])

distribution is again not significantly affected by the deposit and is almost symmetric. For $\kappa_D > \kappa_S$, the general trend is the same as for the discs. For realistic geometrical parameters for the width d and the thickness h of stripes, and for v_s/D_t small compared to a typical parameter ν_α, the temperature profiles are essentially unaffected by the velocity of the laser beam. For example, for parameters d = 6 µm, h = 0.6 µm we obtain v_α = 0.5 µm^{-1}, which corresponds to scanning velocities of 50 m/s on Si and 0.50 m/s on glass. These values exceed realistic scanning velocities in laser-induced deposition by several orders of magnitude. The temperature profiles shown in Fig.2.13 are therefore very similar to those shown in Fig.2.12. The main differences in Fig.2.13 result from the heat transport along the stripe (positive x-direction), which yields a reduction of the center temperature with increasing cross section of the stripe. This effect is especially significant for $\kappa_D >> \kappa_S$ (Fig.2.14). The temperature distributions shown in Figs.2.10-14 will be further discussed in Chap.5.

For the model structures shown in Figs.2.9a-c, which are relevant in laser-induced *etching*, only preliminary calculations have been performed [2.5,6]. The case of Fig.2.9a is very simple as long as d > $2w_0$. Under this condition, the temperature distribution is similar to that of a semiinfinite

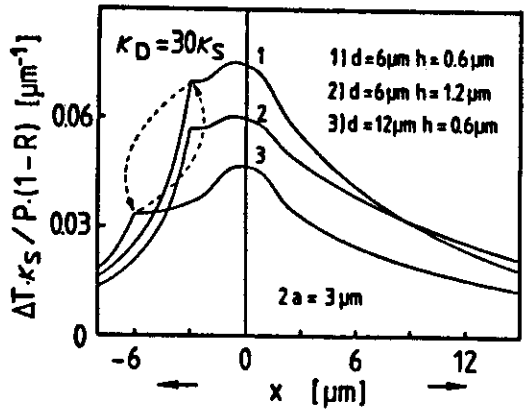

Fig.2.14. Influence of the cross section of stripes on the temperature profile. The meaning of the dashed arrows is explained in Sect.5.2.5 (after [2.2])

substrate. The situation becomes much more difficult when the width d becomes comparable to the laser focus $2w_0$. For the case of the V-shaped hole shown in Fig.2.9c, the calculations are more complicated even for d > $2w_0$. If we neglect multiple reflections of the laser light within the hole, we obtain a temperature distribution that shows a marked dip at the center of the hole, i.e. for r = 0. This would imply, of course, that further laser beam illumination would change the shape of the hole. This contradicts the experimental results in Chap.8. To maintain the maximum temperature rise at the center, one has to take into account the dependence of the reflection and absorption coefficients on the angle of incidence and, additionally, multiple reflections of the laser light inside the hole. A comparison with the experimental results in Chap.8 requires consideration of another point. While the depths h of holes increase continuously with laser beam illumination time t_i, the widths d remain about constant. Consequently, the angle of incidence of both the incoming laser light and the internally reflected laser light will also change with time. Similar difficulties arise for the model in Fig.2.9a if d becomes < $2w_0$, and also for the intermediate case shown in Fig.2.9b. Therefore, the distribution of the absorbed laser power within the hole becomes very complicated and differs significantly from the intensity distribution within the laser beam. In most cases, the real situation in laser-induced etching is even more complex. The material that is ejected out of the hole during the etching process scatters and/or partially absorbs the incoming and internally reflected laser light. These difficulties may explain why calculated temperature distributions for the modeling of laser-induced

etching have not so far proved very enlightening. This is quite different from the case of laser-induced deposition, where many experimental results can be understood from the calculations outlined above.

The accuracy of the model calculations is closely related to the knowledge of the parameters R, κ, α, etc. that enter these calculations. These parameters often depend on the temperature itself; one must then perform calculations self-consistently. Additionally, these parameters may change with the laser wavelength, the microstructure and morphology of the material within the processed area, the film thickness, impurities, etc. It is therefore desirable to measure these quantities, or at least some of them, in situ, i.e. during the deposition or etching process. For a few model systems such measurements have in fact been performed for R and α. In some cases, additional estimations can be made. For example, the reflectivity of rough surfaces does not depend upon the depth or the spatial period of the roughness independently, but rather upon their ratio. This has been studied by KIVAISI and STENSLAND [2.47]. By comparing morphologies of deposits derived from scanning electron micrographs with the results in [2.47], additional information on the value of R may be obtained.

2.2 Photolytic Processing

In photolytic (photochemical) processing, the laser light breaks chemical bonds directly within the surface of the material itself, within adspecies or within the surrounding gaseous or liquid medium. Photochemical bond-breaking can be based on dissociative electronic excitations, which are located in the visible and ultraviolet spectral region, or on *selective* multiphoton vibrational excitations by means of infrared radiation. An indirect mechanism is to transfer the bond-breaking energy via an intermediate species as, for example, in photosensitization. Clearly, single- or multiphoton dissociation of molecules based on direct or indirect electronic excitation is a nonthermal and very common process. Photochemical dissociation of molecules based on selective multiphoton vibrational excitations is not as common and in fact very rare in LCP. The fine details of the different fundamental mechanisms have been extensively studied for model systems and frequently discussed in a great variety of monographs and conference proceedings (see e.g. [2.48-61]). On the other hand, apart from a very few exceptions, only little is known about the photochemistry of those molecules that are relevant in LCP. Additionally, in most LCP situations, the physical conditions with respect to molecular densities, temperatures, the great variety of species,

the presence of interfaces or acceptors, etc., differ significantly from those generally chosen for separating and investigating single interaction mechanisms. Selective bond breaking in the condensed phase is not yet well understood and difficult to realize because of line broadenings and fast vibrational relaxations into heat, typically within 10^{-13} - 10^{-11} s. In the following outline we will confine ourselves to some fundamentals, with special emphasis on the literature on those gas-phase molecules that are used as precursors in LCP. Solid-phase excitation will be discussed further in Chap.3.

2.2.1 Dissociative Electronic Excitations

Electronic dissociation of molecules can be based on single- or multiphoton processes. Such processes are, in general, accompanied by simultaneous excitations of vibrational and rotational transitions (see e.g. [2.48-64]).

Let us start with four characteristic cases of dissociative single-photon excitations. Figure 2.15 shows schematically potential energy curves for the electronic ground state and excited states of different molecules. For simplicity, vibrational and rotational energy levels are not included. According to the Franck-Condon principle, transitions always occur vertically between maxima in $|\Psi_1|^2$ and $|\Psi_2|^2$, where the Ψ_i are the corresponding vibrational wave functions in the lower and upper electronic states. In the

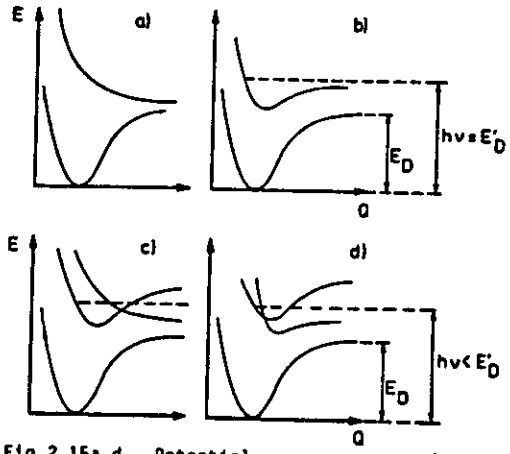

Fig.2.15a-d. Potential energy curves for the electronic ground state and excited states showing different cases of dissociation. Here, E_D is the energy of dissociation and hν the photon energy. Vibrational and rotational energy levels are not included in the curves

after having been brought into the unstable excited state, typically dissociates within 10^{-13} - 10^{-14} s. Clearly, relaxation and energy transfer between gas-phase molecules is unlikely within such a short time. In the case of Fig.2.15b the excited electronic state is stable and dissociation only occurs for photon energies $h\nu > E_D'$. However, in many cases dissociation is even observed for $h\nu < E_D'$ (Figs.2.15c,d). This phenomenon is called spontaneous predissociation. Here, dissociation occurs before the dissociation limit of the initially excited electronic state by transitions to another unstable (Fig.2.15c) or less stable (Fig.2.15d) electronic state. Another mechanism is dissociation by internal conversion into vibrational states of the electronic ground state having an energy above E_D. Such transitions become possible if a mixing of states near crossings of potential curves occurs. Predissociation is therefore much more frequent in polyatomic molecules than in diatomic molecules. The typical time scale for predissociaton extends from 10^{-6} to 10^{-12} s. For low light intensities the average number of dissociated molecules N_d is proportional to the laser fluence ϕ and is given in good approximation by $N_d = \sigma_d^{eff} N \phi/h\nu$, where N is the total number of molecules within the interaction volume and $\phi = I\tau$, I being the laser light intensity and τ the laser beam illumination time. The effective cross section for dissociation is $\sigma_d^{eff} = \eta\sigma_d$. The dissociation yield η depends on the gas pressure, the type of reactant and buffer gas molecules, etc. Under collisionless conditions, $\eta = 1$. For $h\nu > E_D'$ and negligible fluorescence, the dissociation and absorption cross sections are equal, i.e. $\sigma_d = \sigma_a$. In the case of linear interaction, this number of excited or dissociated molecules is independent of whether irradiation is pulsed or continuous.

The main limitation of single-photon decomposition processes relevant to laser-induced chemical processing is the lack of flexibility of available lasers in the medium to far ultraviolet spectral region. Multiphoton processes impose less severe wavelength restrictions on the absorption continuum of the reactive species than single-photon processes. However, in this case the number of excited molecules depends nonlinearly on the photon flux, and hence on the excitation conditions. Efficient processing can only be performed with high power pulsed lasers. Here, other problems may arise in many processing applications (Sect.4.2).

In the following, we will become more specific and concentrate on the *homogeneous* photochemistry of molecules that are most commonly used in deposition, surface modification and etching reactions. A brief glance at

Table 2.2. Dissociation (d) and absorption (a) cross sections σ_d^{eff} and σ_a for parent molecules used in LCP

Molecule	σ [$\times 10^{-18}$ cm^2]	λ [nm]	Ref.
$Al_2(CH_3)_6$	20 (a)	193	[2.75]
	0.002 (a)	257	[2.75]
AsH_3	18 (a)	193	[2.66]
B_2H_6	0.2 (a)	193	[2.66]
$Cd(CH_3)_2$	2 (a)	257	[2.75]
$Cr(CO)_6$	12 (a)	193	[2.72]
	33 (a)	249	[2.72]
	5.2 (a)	308	[2.72]
$Fe(CO)_5$	240 (a)	193	[2.67]
	27 (a)	248	[2.67]
	1.3 (a)	355	[2.67]
$Ga(CH_3)_3$	5.4 (a)	193	[2.68]
	0.09 (a)	257	[2.68]
GeH_4	0.0035 (a)	193	[2.32]
InI	<7 (d)	193	[2.69]
$Mo(CO)_6$	60 (a)	193	[2.72]
	44 (a)	249	[2.72]
	11 (a)	308	[2.72]
	0.5 (a)	350 – 360	[2.70]
NF_3	0.0053 (a)	193	[2.71]
$Ni(CO)_4$	30 (a)	248	[2.136]
	2.4 (a)	308	
PH_3	13 (a)	193	[2.66]
$Pt(PF_3)_4$	0.19 (a)	248	[2.73]
Pt(HFAcAc)[a]	100 (a)		[2.74]
SiH_4	0.0012 (a)	193	[2.66]
TlBr	22 (d)	193	[2.69]
TlI	24 (d)	193	[2.69]
	2.6 (d)	248	[2.69]
$W(CO)_6$	12 (a)	193	[2.72]
	4.5 (a)	249	[2.72]
	2.4 (a)	308	[2.72]
	0.5 (a)	350 – 360	[2.70]

[a] HFAcAc is $CF_3COCHCOCF_3$ i.e. the 1,1,1,5,5,5 hexafluoro-2,4-pentane-dionate anion, which is also known as the hexafluoroacetylacetonate anion.

Tables 5.1, 6.2 and 8.1 reveals that the most important precursor molecules involve alkyls, carbonyls, halides and hydrides. Table 2.2 summarizes dissociation (d) and absorption (a) cross sections for certain compounds at specific laser wavelengths. It becomes evident that the values of σ may differ, at a certain wavelength, by several orders of magnitude. For example, for $Cd(CH_3)_2$ and $Al_2(CH_3)_6$ (the molecule is dimerized at 300 K and pressures of several millibars) the absorption cross sections at λ = 257 nm differ by a factor of about 10^3. This can be derived from the UV absorption spectra presented in [2.75]. Efficient dissociation of $Al_2(CH_3)_6$ requires irradiation at a shorter laser wavelength. It is absolutely essential to note that the dissociation yield depends strongly on gas pressure and on possible admixtures. Furthermore, LCP is often performed not homogeneously, but at gas-solid or liquid-solid interfaces. Therefore, laser-molecule-surface interactions are of great importance. As a consequence, the photodissociation yield may change by orders of magnitude with respect to collisionless unimolecular reactions or homogeneous collision-induced reactions within the gas or liquid phase. Various light-molecule-surface interaction mechanisms are discussed in Chap.3.

Metal alkyls, such as $Al_2(CH_3)_6$, $Cd(CH_3)_2$, $Zn(CH_3)_2$, have been used for the deposition of the corresponding metals (Sects.5.2 and 5.3) and, additionally, as doping gases (Sect.6.3). Admixtures of these molecules with N_2O or NO_2 allow formation of oxide layers (Sects.5.3.2 and 5.3.3). The molecules $Ga(CH_3)_3$, $P(CH_3)_3$, $Zn(CH_3)_2$, $(CH_3)_3InP(CH_3)_3$, etc. are precursors for the deposition of compound semiconductors (Sect.5.3.2), and many of them show dissociative continua in the near to medium ultraviolet, which can easily be reached with available laser sources. The photothermal and photochemical decomposition kinetics of many metal alkyls and carbonyls has been reviewed by PRICE [2.64]. For most of the metal alkyls, however, little is known about the details of the various photofragmentation channels. An exception is $Cd(CH_3)_2$, which has been studied both theoretically [2.76] and experimentally [2.77]. According to these investigations, single-photon absorption near 257 nm (frequency-doubled Ar^+ laser radiation) results in dissociation into ground state Cd and CH_3 according to

$$Cd(CH_3)_2 + h\nu(257\ nm) \longrightarrow Cd(^1S_0) + 2CH_3 \ . \qquad (2.20)$$

Dissociation is asymmetric, with one CH_3 group leaving at least half a period of vibration later than the first. The free methyl radicals subsequently react to form volatile hydrocarbons such as ethane.

Metal carbonyls, such as $Ni(CO)_4$, $Fe(CO)_5$, $Cr(CO)_6$, $Mo(CO)_6$, and $W(CO)_6$, were used for metal deposition in the form of both microstructures and extended thin films. The photodissociation dynamics of these molecules has been studied in some detail [2.64,67,78-84]. For many metal carbonyls, molecular fragmentation begins to occur in the near UV region at wavelengths λ < 350 nm. For cw and pulsed laser irradiation at low power densities, decomposition seems to be based on *sequential* elimination of CO ligands by single photon processes, such as

$$Me(CO)_m + h\nu \longrightarrow Me(CO)^*_{m-1} + CO \ , \qquad (2.21a)$$

$$Me(CO)^*_{m-1} + h\nu \longrightarrow Me(CO)^*_{m-2} + CO \ , \qquad (2.21b)$$

$$\vdots \qquad \vdots \qquad \vdots \qquad \vdots$$

$$Me(CO)^* + h\nu \longrightarrow Me^* + CO \ , \qquad (2.22)$$

where * indicates internal vibrational and possibly electronic excitation. Because of the high gas pressures used in LCP, stripping of the remaining ligands, for example after absorption of two photons according to (2.21a) and (2.21b), can also occur by subsequent collisional events. YARDLEY et al. [2.67] have investigated the photolysis of $Fe(CO)_5$ at 352 nm (TH Nd:YAG), 218 nm(KrF) and 193 nm (ArF). At low laser fluences and gas pressures below 130 mbar, the primary fragmentation into $Fe(CO)_{5-n}$ with $1 \leq n \leq 4$ proceeded via one-photon absorption. A large fraction of the initial energy was found to have been retained as internal electronic and vibrational energy in the metal-containing fragment. The photofragmentation of $Cr(CO)_6$ has been studied recently by SEDER et al. [2.79]. Under 351 nm XeF laser radiation the major photolysis product was $Cr(CO)_5$. The large relative yield of $Cr(CO)_5$ is consistent with the observations of BRECKENRIDGE and SINAI [2.80] who used 355 nm frequency-tripled pulsed Nd:YAG laser radiation. Focused high power pulsed laser excitation may favor *coherent* multiphoton rather than sequential single-photon photochemistry. FISANICK et al. [2.83] have studied the multiphoton dissociation (MPD) and ionization (MPI) of $Cr(CO)_6$ and related compounds. Different fragmentation channels have been observed for parent molecule excitation below and above the ionization limit corresponding to a wavelength of about 400 nm.

The photochemistry of organometallic coordination complexes has recently become the object of great interest. Such compounds have been successfully

used as precursors for noble metal deposition. Initial investigations on the generation of Cu atoms from the photodissociation of $Cu(HFAcAc)_2$ have been performed by MARINERO and JONES [2.85]. Transition metal complexes such as CrO_2Cl_2, OsO_4 and $Pt(PF_3)_4$ have been investigated by SCHRODER et al. [2.73,86].

Halides like Cl_2, Br_2, I_2, etc. show strong continua in the visible and ultraviolet region. They result at least in part from the allowed dissociative transition $^1\Pi_u \leftarrow {}^1\Sigma_g$, for example

$$Cl_2 + h\nu \ (\lesssim 500 \text{ nm}) \longrightarrow 2Cl \ . \qquad (2.23)$$

For Cl_2, the maximum in the dissociative continuum occurs at about 330 nm. At wavelengths $\lambda > 480$ nm, the continuum is very weak and has vibrational structure superimposed on it, resulting from transitions into the bound $^3\Pi(0_u^+)$ state. If absorption occurs at a wavelength short enough to break the bond ($\lambda < 498.9$ nm), this bound state predissociates with near unity yield by crossing over to a repulsive state [2.87,88]. For Br_2 and I_2, wavelengths below 628.4 nm and 803.7 nm are necessary to dissociate or predissociate the molecule. The halogen radicals are very aggressive. They strongly chemisorb on many surfaces and may thereby break surface chemical bonds. Photoreactions such as (2.23) are therefore often used in materials etching (Chap.8). Similarly, photochemical etching is also often performed with halogen compounds such as COF_2, CF_2Cl_2, CF_2Br_2, CF_3Br, CF_3I, CF_3NO, $CO(CF_3)_2$. These molecules can be photodissociated with ArF or KrF excimer laser radiation resulting in highly reactive radicals such as F, Cl, CF_2, CF_3 [2.48,52,57,89,90-92]. Ultraviolet absorption spectra of many of these compounds are shown in [2.90-92]. The pyrolytic and photolytic decomposition kinetics of many halides has been reviewed by ARMSTRONG and HOLMES [2.93]. Admixtures of metal halides and hydrogen are used for metal deposition. The most important precursor molecule so far is WF_6. This molecule is most commonly used for photodeposition of extended thin films of W, mainly by means of ArF excimer laser radiation. DEUTSCH and RATHMAN [2.94,95] suggest that the ArF laser radiation initially produces WF_n ($n = 1-5$) radicals which further react with hydrogen (Sect.5.3.1).

Hydrides such as SiH_4, Si_2H_6, GeH_4, CH_4, C_2H_2 are used for deposition of Si, Ge and C. Photolysis of admixtures of SiH_4 with N_2O is important in thin film formation of SiO_2 (Sect.5.3.3). AsH_3, B_2H_6, and PH_3 are used as precursors for silicon doping. Direct photochemical decomposition of silicon hydrides can occur only for wavelengths of less than 200 nm. PERKINS et al. [2.96] have studied the 147 nm photolysis of SiH_4, using a Xe resonance lamp.

Two primary decomposition processes have been revealed

$$SiH_4 + h\nu \longrightarrow SiH_2 + 2H \qquad (2.24)$$

and

$$SiH_4 + h\nu \longrightarrow SiH_3 + H \ . \qquad (2.25)$$

The final products of the photodecomposition reaction were H_2, Si_2H_6, Si_3H_8 and a film of hydrogenated amorphous silicon (a-Si:H; see also Sect.5.3.2). The shortest laser wavelength that has been used for the decomposition of SiH_4 is 193 nm, the ArF excimer laser line; no experiments with 157 nm F_2 laser radiation are known (Table 4.1). At 193 nm, SiH_4 has negligible linear absorption. However, the molecule can be dissociated at this wavelength with relatively low fluences (< 10 MW/cm^2) by multiphoton excitation. ArF laser photolysis of C_2H_2 has been investigated by IRION and KOMPA [2.97].

At wavelengths less than 200 nm, the primary photolysis steps for AsH_3, B_2H_6 and PH_3 are thought to include production of AsH_2, B_2H_5, PH_2 and atomic H [2.66]. In the presence of SiH_4, the H atoms may react with SiH_4 according to

$$SiH_4 + H \longrightarrow SiH_3 + H_2 \ . \qquad (2.26)$$

The photochemistry of N_2O and NH_3 has met with increasing interest in connection with the deposition of extended thin films of oxides and nitrides (Sect.5.3.3). For N_2O the quantum yield for dissociation is about 1 in the wavelength region 138 - 210 nm [2.98]. Its photochemistry has been well categorized for single-photon excitation [2.98-103]. The primary reactive product under ArF excimer laser irradiation [2.103] is excited atomic oxygen

$$N_2O + h\nu(193 \text{ nm}) \longrightarrow N_2 + O(^1D) \ . \qquad (2.27)$$

The photodissociation of NH_3 under 193 nm ArF laser irradiation has been investigated by DONNELLY et al. [2.104]. The primary photoproduct is ground state NH_2, which is formed with nearly unit efficiency.

2.2.2 Photosensitization

In photosensitization the photons are directly absorbed by intermediate species which then deexcite by collisional transfer of the appropriate energy to the acceptor molecules (see e.g. [2.57]). For example, direct photolysis of CH_4 is only possible below 144 nm

$$CH_4 + h\nu(<144\ nm) \longrightarrow CH_2 + H_2 \ , \qquad (2.28)$$

while the Hg-photosensitized reaction can take place at a longer wavelength

$$Hg(^1S_0) + h\nu(253.7\ nm) \longrightarrow Hg(^3P_1) \ , \qquad (2.29)$$

$$Hg(^3P_1) + CH_4 \longrightarrow Hg(^1S_0) + CH_3 + H \ . \qquad (2.30)$$

As can be seen from this example, the products of these photoreactions may differ greatly in both cases. Mercury-photosensitized decomposition of SiH_4 and GeH_4 has been studied by NIKI and MAINS [2.105] and by ROUSSEAU and MAINS [2.106], respectively. Photosensitized reactions are very common in photochemical studies, but are not favored for localized microchemistry due to the reaction-spreading properties intrinsic to the process (see also Chap.9). However, the technique can be used for large-area processing. Examples are the low temperature growth of epitaxial layers of HgTe [2.107,108] and etching reactions with CF_3, produced from $CO(CF_3)_2$ via photosensitization of C_6H_5F by KrF excimer laser light [2.90-92].

2.2.3 Infrared Vibrational Excitations

In this section we will briefly outline some fundamentals of laser-induced vibrational excitations of free molecules in the electronic ground state. Several reviews have appeared in this field in the last few years [2.48-52, 58-61,109-111]. Here, we again put special emphasis on molecules and aspects that are relevant to LCP.

Let us commence by defining terms: We will henceforth call gas- or liquid-phase reactions thermal if the absorbed laser energy is at least locally thermalized between the different degrees of freedom. On the other hand, we will call reactions nonthermal if there are molecules participating in them that are not in local thermal equilibrium. We will use the term nonthermal or photochemical reaction even in cases where the laser light induces a local temperature rise but without complete thermalization, e.g. between vibrational and translational degrees of freedom.

Classification can be performed according to the relaxation times $\tau_{v\text{-}v}^{intra}$, $\tau_{v\text{-}v}^{inter}$, $\tau_{v\text{-}T}$, and the rate of vibrational excitation W_e. The first quantity, $\tau_{v\text{-}v}^{intra}$, is the time for intramolecular transfer of vibrational energy between different vibrational modes of the molecule being excited. This time increases with decreasing vibrational anharmonicity and is typically of the order of 10^{-12} to 10^{-11} s. The second, $\tau_{v\text{-}v}^{inter}$, is the

time for intermolecular transfer of vibrational energy between molecules of the same kind or of different kinds within a gas or a liquid. Finally, $\tau_{v\text{-}T}$ is the relaxation time for molecular vibrational energy to be transferred to translational degrees of freedom - which is the time for thermal equilibrium to be reached in the molecular mixture. Clearly, the times $\tau_{v\text{-}v}^{inter}$ and $\tau_{v\text{-}T}$ vary with experimental conditions such as the molecular density, temperature and type of admixtures or solvents. For gases such as NH_3 or BCl_3 at 1000 mbar, $\tau_{v\text{-}v}^{inter}$ is typically of the order of 10^{-9} s. The value of W_e will depend on the radiation intensity and the cross section of the specific vibrational transition. For further details see, for example, the monographs by BEN-SHAUL et al. [2.48] and LETOKHOV [2.52].

Mode- or *bond*-selective multiphoton excitation requires an excitation rate that is large compared to the rate of intramolecular vibrational energy transfer. This would need laser pumping in a mode fairly isolated from the other vibrational modes and high laser intensity picosecond or subpicosecond excitation. While the first condition is well fulfilled for diatomic molecules, which have only one vibrational degree of freedom, collisionless multiphoton dissociation by monochromatic infrared radiation seems to be impossible in this case because of the energy mismatch between the photon energy and the vibrational energy levels, which, because of the anharmonicity in the potential, are not equally spaced. This latter restriction is relaxed in the case of polyatomic molecules (see below). Nevertheless, bond-selective dissociation has not yet been convincingly demonstrated even in a collisionless environment.

In the following we consider three different cases that can be realized under conditions used in LCP. First, if

$$1/\tau_{v\text{-}v}^{intra} >> W_e >> 1/\tau_{v\text{-}v}^{inter} \ , \qquad (2.31)$$

molecule-selective excitation is possible. While the vibrational energy within the molecule interacting with the infrared field is in equilibrium, there is no vibrational equilibrium among the molecules in the mixture. In other words, molecules in resonance with the laser frequency acquire a higher vibrational temperature than all the other molecules. Molecule-selective excitation and dissociation according to (2.31) is of considerable practical interest, e.g. in laser isotope separation, and it has been studied in great detail. In order to separate single effects, many of the fundamental investigations have been performed in the collisionless environment of a molecular beam. Under this condition, $\tau_{v\text{-}v}^{inter}$ approaches infinity. For this case, we will briefly describe the dissociation process. In contrast to

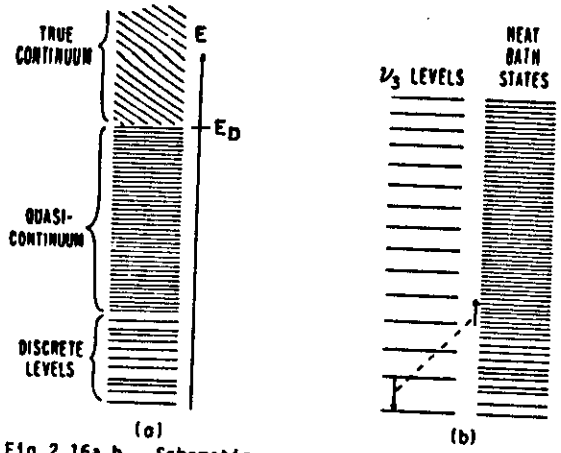

Fig.2.16a,b. Schematic representation of vibrational energy levels in a polyatomic molecule. (a) shows three regimes of energy levels. (b) shows the levels for the selectively driven mode ν_3, and the ensemble of other vibrational levels. Energy transfer and relaxation are caused by anharmonic coupling of modes

diatomic molecules, polyatomic molecules can absorb a great number of monochromatic photons [2.48-52,59-61,109-114]. This can be made plausible from the schematic of vibrational energy levels shown in Fig.2.16. At very low energies the energy levels are discrete. With increasing vibrational energy and number of atoms of the polyatomic molecule, the complexity of the energy levels increases very rapidly. The energy states become very dense. This region is called the quasi-continuum, which merges into a true continuum above the dissociation limit. The quasi-continuum typically starts at the level of 1 vibrational quantum (for complex molecules and molecules with heavy atoms) to 3-10 vibrational quanta (for simple polyatomic molecules). It can be described as a heat bath of states formed by the other vibrational degrees of freedom. The dissociation process involves an initial, selective excitation of the infrared driven mode into the quasi-continuum region, followed by energy absorption by the quasi-continuum until the lowest dissociation channel is reached. Collisionless infrared multiphoton excitation and dissociation of many molecules, including SF_6, BCl_3, $CO(CF_3)_2$, CF_3I and CDF_3, which are also used in LCP, is consistent with this model. Clearly, this model describes the situation in gas mixtures equally well, as long as condition (2.31) is fulfilled. The average number of IR photons absorbed by a molecule is $\langle n \rangle = \sigma\Phi/h\nu$, where Φ is the laser fluence and σ the absorption cross section. In general, σ is not a constant but itself changes

with laser fluence and within the time τ of the laser pulse. The value of Φ for which $\langle n \rangle \gg 1$ ranges from 10^{-3} J/cm^2 for complex molecules to tens of J/cm^2 for simpler molecules with large rotational constants [2.52].

Second, we consider the condition

$$1/\tau^{inter}_{v-v} \gg W_e \gg 1/\tau_{v-T} \,. \tag{2.32}$$

Here, the vibrational equilibrium among all the molecules in the mixture is stronger, but the system is still not in thermal equilibrium. Condition (2.32) can only be fulfilled if the gas mixture does not contain any component with fast v-T relaxation. Because of the difference between vibrational and translational temperature, nonselective vibrational photochemistry is possible when reactions with a minimum energy barrier take place in a time not greater than about τ_{v-T}.

The last condition is characterized by

$$W_e \ll 1/\tau_{v-T} \,. \tag{2.33}$$

In this case, all the molecules within the reaction volume defined by the laser beam are in thermal equilibrium. The vibrational energy is immediately thermalized through bi- or multimolecular collisional channels. The reaction is purely thermal. Nevertheless, laser-induced gas- or liquid-phase heating may significantly differ from traditional heating, e.g. via thermalization at or near the surface of a heated substrate. This has already been mentioned at the beginning of Sect.2.1.

After these very general remarks, we will become more specific and discuss some reactions that are of special importance in LCP. First of all, we should be aware that for the complex molecules and molecular mixtures commonly used in LCP, very little is known about the various v $\longrightarrow$ v and v $\longrightarrow$ T relaxation pathways. However, because of the complexity and variety of the molecules involved and also on account of the high molecular densities used, we can speculate that condition (2.32), and to an even greater extent condition (2.33), will apply in most cases. An important example in LCP that seems to belong to this case is the deposition of hydrogenated amorphous Si from SiH_4 by means of CO_2 laser radiation incident parallel to the substrate (see Fig.4.3 and Sect.5.3). It has been shown by MEUNIER et al. [2.115] that the deposition rate follows an Arrhenius type behavior where the temperature corresponds to the gas temperature T_g induced by single-photon vibrational absorption of SiH_4 and collisional redistribution within the volume of the incident laser beam. This interpretation is supported by the comparison of

relaxation times. For typical conditions (an absorbed laser power of 1 W/cm^2, a gas pressure of $p(SiH_4)$ = 10 mbar and a gas temperature of 10^3 K) the excitation rate for a molecule is about $W_e = 10^3\ s^{-1}$; and the average time between collisions about 10^{-8} s. The vibrational-translational relaxation rate is about $1/\tau_{V-T} = 10^4\ s^{-1}$. Therefore, (2.33) seems to be readily fulfilled. Nevertheless, the detailed dissociation mechanism is still under discussion [2.116-119].

In spite of the fact that in LCP most reactions induced by infrared laser light are nonselective, there are some clear exceptions. Among these are gas-phase etching reactions (Chap.8) that are based on multiphoton vibrational excitation and dissociation (MPD) of precursor molecules such as SF_6, CF_3Br, CDF_3. It is SF_6 that has been most extensively studied with respect to both its fundamental excitation mechanisms [2.58-60,109,110,112-114, 121-128] *and* its etching characteristics [2.129-133] under pulsed CO_2 laser irradiation. For low laser fluences ranging from about 0.1 to 1 J/cm^2 (2-20 MW/cm^2) non-dissociative coherent excitation occurs according to

$$SF_6 + nh\nu(CO_2) \longrightarrow SF_6^* \ , \qquad (2.34)$$

where n may be greater than 3. The * indicates the vibrational excitation of the molecule. The difference between SF_6 and SiH_4 in the initial stages of absorption is probably due to the extremely dense rotational structure that generally makes compensation of anharmonicity effects in heavy polyatomic molecules more probable. In other words, contrary to SiH_4, pumping of SF_6 into the quasi-continuum is possible without intermediate collisions. On focusing the laser light to power densities of 5 to 10 J/cm^2, multiphoton dissociation of the SF_6 molecule is observed. This may be symbolically described by

$$SF_6 + Nh\nu(CO_2) \longrightarrow SF_5 + F \ , \qquad (2.35)$$

where N is usually 30 or greater. SF_5 is unstable and further decomposes into SF_4 and another F atom.

Multiphoton absorption spectra show a number of characteristic features: a distinct resonance behavior, a broadening and shifting of the resonance to lower frequencies with increasing laser fluence and a strong dependence of the intensity on laser fluence. For SF_6, these characteristics have been studied by BAGRATASHVILI et al. [2.125]. They compare favorably with laser etching experiments performed in a SF_6 atmosphere (Chap.8). A further point to consider for selective infrared LCP is the dependence of the dissociation yield on gas pressure (see e.g. [2.52] and references therein). For many

monomolecular gases, the dissociation yield is independent of the gas pressure, within a certain range. In the case of SF_6 this has been demonstrated for the range 0.1 mbar < $p(SF_6)$ < 5 mbar [2.135]. This behavior is related to the fact that the v-v exchange between molecules of the same type can take place without a reduction of the average vibrational energy. Collisions between *different* types of molecules can result in a decrease or an increase in dissociation yield. For SF_6 [2.124], CF_3I [2.134], etc., an admixture of monoatomic buffer gases decreases the dissociation yield. For other molecules such as CDF_3, C_2H_4, $C_2H_2F_2$, however, the dissociation yield shows a pronounced maximum when the buffer gas pressure is increased. In the case of CDF_3 [2.135] with Ar, this maximum occurs at a pressure of p(Ar) = 25 mbar and exceeds the monomolecular yield by a factor of about 45. The influence of admixtures on the dissociation yield depends on the types of interacting molecules, the gas pressure, the laser fluence, etc. Vibrational energy transfer requires energy matching between vibrational modes, and will be more efficient with complex polyatomic molecules than with simple molecular or monoatomic species.

3. Laser-Induced Chemical Reactions

Laser light can induce chemical reactions either homogeneously within the gas or liquid phase, or heterogeneously at molecule-solid or solid-solid interfaces. In LCP, homogeneously activated reactions are induced near substrate surfaces with the laser beam at parallel incidence (see Fig.4.3). The photoproducts that diffuse to the substrate surface may give rise to extended thin film deposition (Sect.5.3), or to *nonlocal* etching of the material surface (Chap.8). Heterogeneously activated reactions are generally performed at normal incidence of the laser light. As shown schematically in Fig.3.1, such reactions can take place in adsorbed layers, at gas-solid or

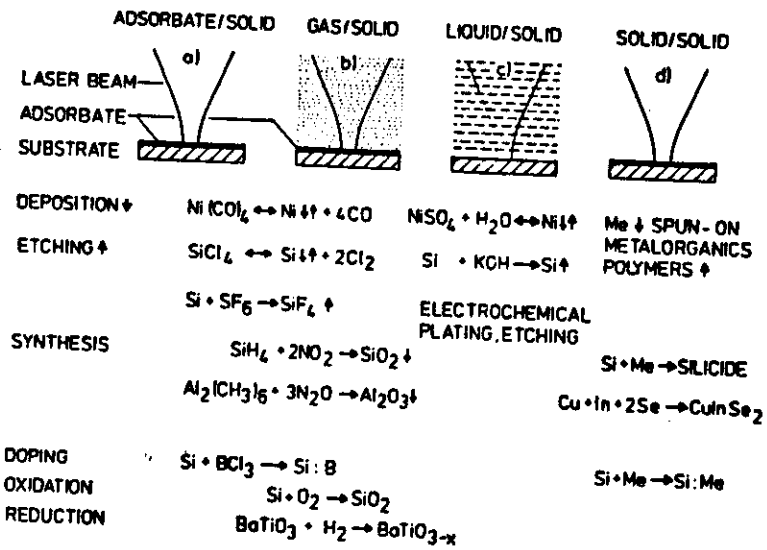

Fig.3.1. Examples of laser-induced chemical reactions at interfaces. For simplicity, not all reaction products are included in the formulas. The arrows refer to deposition (↓) and etching (↑). Me stands for metal. ⟷ means that the reaction can be turned around by simply shifting the chemical equilibrium to the other side

liquid-solid interfaces or within the surface of the material itself. Examples of such reactions that result in local material deposition, etching, surface modification or compound formation are included in the figure. Clearly, homogeneous and heterogeneous laser-induced chemical reactions may be activated both pyrolytically and/or photolytically, depending on the interaction mechanisms discussed in Chap.2. Nevertheless, the reaction rates and pathways can be quite different for homogeneous and heterogeneous reactions. In part this originates from the influence of additional light-molecule-surface interactions: Surface adsorption may change the cross section for photodissociation of molecules by several orders of magnitude. Solid surfaces may promote decomposition of partly (homogeneously) dissociated molecules. Laser light may change the properties of surfaces by lattice phonon excitations, electron-hole pair generation, electron emission, etc.

In this chapter we shall outline some fundamentals of the reaction kinetics, mainly for heterogeneously activated reactions, and discuss some of the additional interaction mechanisms mentioned above.

In general, laser-induced reactions consist of a number of consecutive steps:

1. Transport of reactants into the reaction volume
2. Adsorption of one or more reactants onto the substrate
3. Pyrolytic or photolytic activation of molecules near or at the substrate surface
4. Transport of product atoms or molecules to the surface, with possible recombination or secondary reactions on the way
5. Condensation or further reactions of the products of 3 on the surface
6. Desorption of reaction products from the substrate
7. Transport of reaction products out of the reaction volume

Clearly, in different types of LCP, one or more of these steps will either not occur at all or else will differ significantly. The rate-limiting step will depend on the activation mechanisms (photothermal and/or photochemical), the type of reaction (Figs.3.1a-d), the reaction volume, the density of the reactant medium, the physical and chemical properties of the substrate material, the laser power, wavelength, irradiation time, etc.

The different types of reactions shown in Fig.3.1 will now be discussed in Sects.3.1-4 in more detail. Section 3.5 deals with the spatial confinement of laser-induced heterogeneous reactions.

3.1 Adsorbed Layers

Laser-induced chemical processing may be strongly influenced by the adsorption of reactants, reaction products or impurities. Adsorbates may control reaction rates, the spatial resolution of structures and, in the case of deposition or compound formation, nucleation times and the composition and morphology of films.

Molecules on solid surfaces may be adsorbed either physically or chemically. The bond energies of physisorbed molecules are typically 1-10 kcal/mole (binding energies ≈ 0.05-0.5 eV). For chemisorbed molecules the bond energies are of the same magnitude as those of intramolecular bonds, and typically range from 10 to 100 kcal/mole (≈ 0.5-5 eV). The statics and dynamics of the interactions between atoms or molecules and solid surfaces have been extensively studied [3.1-5,38]. Most of these investigations were performed under ultrahigh-vacuum (UHV) conditions. Here, atom- or molecule-surface interactions are studied for low surface coverages or for particle beams at physically well-defined solid surfaces. In this section we will briefly mention only those aspects that are relevant to LCP: The number of molecules being adsorbed depends on the energy with which they are bound to the substrate surface, on their interaction with each other (e.g. by dipole-dipole coupling), on the substrate temperature and on the molecular density of the surrounding medium. The strength of these interactions also determines the extent of changes in the electronic and vibrational properties of adsorbed molecules with respect to free molecules. In any case, adsorption may result in shifts and broadenings of electronic and vibrational energy levels and in relaxation of selection rules for interaction with light. Therefore, the cross section for photoexcitation at a particular wavelength may differ significantly for adsorbed and gas-phase molecules [3.4-6]. Contrary to investigations on basic molecule-surface interactions, LCP is generally performed only in high-vacuum (HV) reaction chambers that can be pumped out to between 10^{-6} and a few 10^{-7} mbar. Additionally, substrates are in most cases only chemically cleaned according to standard procedures. As a consequence, substrate surfaces may be contaminated with water vapor, organic molecules, etc., which may change the aforementioned interactions and photochemical properties of adsorbed reactant molecules.

In the following we first discuss adsorbate-adsorbent systems in a vacuum (Fig.3.1a) and then those in a dynamic equilibrium with a surrounding gaseous atmosphere consisting of the gaseous form of the adspecies (Fig.3.1b).

In the first case, the substrate is first exposed to the gaseous reactant, which, after some time of influence, is pumped off. Laser light irradiation

may result in selective electronic or vibrational (intramolecular bond or adsorptive bond) excitations of the molecules and/or in charge transfer reactions within the adsorbate-adsorbent complex. For a particular molecular species the excitation probability is determined not only by the physical properties of the substrate, but also by its microscopic surface morphology, e.g. its roughness. For example, a strong increase in surface excitation may be observed when a molecular resonance overlaps with optically active surface resonances such as surface plasmons [3.7,8]. The influence of the surface morphology on light-molecule-surface interactions has been clearly demonstrated, e.g. in surface enhanced Raman scattering (SERS) [3.4]. Besides direct excitation, laser light may also interact with adsorbates indirectly via local substrate heating. Due to direct or indirect interaction with laser light, adsorbed molecules may desorb from the surface, migrate across the surface, change the nature of bonding to the surface (e.g. from physical to chemical), diffuse into the bulk, or decompose at or react with the solid surface [3.4,5,7-15]. The latter cases result in deposition, etching, doping, or compound formation. Examples of some reactions are included in Fig.3.1a.

For pyrolytic laser-induced processes the reaction rate achieved within the adlayer is given by

$$W(r,t) = A_{ad}\, N_{ad}(T(r,t)) \exp\left[-\Delta E/RT(r,t)\right] , \qquad (3.1)$$

where A_{ad} is a constant, N_{ad} the temperature-dependent number of adsorbed molecules per unit area and ΔE the apparent chemical activation energy that characterizes the slowest step in the chain of chemical reactions involved. The temperature distribution is given by $T(r,t) = T_0 + \Delta T(r,t)$. Here, T_0 is the overall substrate temperature and ΔT the laser-induced temperature rise (Sect.2.1).

For single-photon photolytic processes, the reaction rate achieved within the adlayer can be described by

$$W(r) = B_{ad} \frac{N_{ad}(T_0)\sigma_{ad}\, P}{h\nu w_0^2} \exp(-2r^2/w_0^2) , \qquad (3.2)$$

where B_{ad} is again a constant, σ_{ad} the dissociation cross section of the adspecies, w_0 the radius of the laser focus and P the effective laser power (Sect.4.2). The value of N_{ad} may be decreased with respect to the unirradiated case due to bond-selective excitation that may result in photodesorption [3.12-15].

It is clear that because of the small number of molecules adsorbed on the solid surface, the amount of deposited, etched or doped material is very small. Because of the exponential decrease of N_{ad} with temperature, this is even more pronounced when the incident laser light heats the substrate. On the other hand, molecules may diffuse along the surface and may thereby modify the effective factor N_{ad} in (3.1) and (3.2). The diffusion length within the time τ is given by $l \approx (2D\tau)^{1/2}$ (the exact result depends on the geometry and size of the reaction zone) with the diffusion coefficient $D = D_0 \exp(-\Delta E_d/RT)$. In the initial phase of laser irradiation, replenishment of reactant molecules may occur quickly by surface diffusion from nearby regions; therefore depletion of reactants will be unimportant, and the reaction rate is mainly determined by the photodecomposition rate within the reaction zone. At later times, however, reactant molecules must diffuse from further away, and ultimately the rate at which this diffusion occurs determines the reaction rate. Clearly, these regimes will also depend on the incident laser power. Examples of LCP from adlayers are given in Chaps.5 and 8.

The role of adsorbed layers may be quite different in laser-induced chemical processing from the gas phase. Because such experiments are usually performed at pressures ranging from 10^{-2} mbar up to more than 10^3 mbar, multiple-layer molecular films are formed on top of the more strongly bound first molecular monolayer. The total number of adsorbed molecules depends on the strength of bonding, the temperature, and the gas pressure. In gas-solid systems where the gas pressure p is near to the vapor pressure p_c, the density of such layers is similar to that of the condensed phase. An empirical equation that provides a good fit to the isotherms of many physisorbed systems having a uniform temperature T [3.1,2] is

$$\Theta(p,T) = cp/[(p_0-p)[1 + (c-1)p/p_0]] , \tag{3.3}$$

where $\Theta(p,T)$ is the amount of adsorbed material with respect to a monolayer coverage. In other words, the total number of adsorbed particles is

$$N_a(p,T) = \Theta(p,T)N_L , \tag{3.4}$$

where N_L is the number of adsorption sites on the substrate. In (3.3), c is a temperature-dependent constant. From (3.3) it is evident that the surface density varies (unlike the gas-phase density) nonlinearly with pressure. The surface coverage is also a sensitive function of temperature, primarily through the variation of the vapor pressure p_0 with temperature. The change

in Θ with even slight changes in temperature is a consequence of the relatively weak binding of physisorbed layers.

Laser radiation may again interact with the adsorbed species as already described above. The coverage of the reactant - and thereby the reaction rate - may be changed if the laser light selectively desorbs one of the components involved in the chemical reaction. Additionally, electronic or vibrational excitation of gas-phase species may change their sticking coefficient. For example, halogen radicals, produced by photodissociation of the corresponding gas-phase molecules, strongly physisorb or chemisorb on semiconductor surfaces, while the corresponding parent molecules are only weakly bound. Another example is the increase in sticking coefficient of vibrationally excited SF_6^* molecules with respect to SF_6 in the vibrational ground state, on semiconductor surfaces (see Sect.2.2 and Chap.8). Adsorption may also change significantly as a result of nonthermal photoexcitation of the substrate surface. Different mechanisms of this type are outlined in Sect.3.2 and Chaps.5-8.

Because of the great thickness of adlayers which are in a dynamical equilibrium with the surrounding gas phase, their influence on reaction rates can become important and, under certain circumstances, dominant.

3.2 Gas-Solid Interfaces

Irrespective of whether a chemical reaction is activated by mainly pyrolytic or mainly photolytic mechanisms, the reaction rate at low laser powers is determined by the kinetics, while at higher laser powers mass transport is rate limiting.

3.2.1 Kinetically Controlled Region

In pyrolytic LCP, the reaction rate in the kinetically controlled region is

$$W(p_f,T(r,t)) = A_g k_0(p_f,T) \exp[-\Delta E/RT(r,t)] , \tag{3.5}$$

where p_f are the partial pressures of the reactants and reaction products, and ΔE is the apparent chemical activation energy. The pre-exponential factor k_0 also depends, although less strongly, on temperature and, additionally, on the partial pressures p_f [see e.g. (5.2)]; A_g is a constant. Equation (3.5) also applies to homogeneously induced gas-phase reactions. Then T is the laser-induced gas-phase temperature. In the following, however, we shall consider only heterogeneous reactions at gas-solid interfaces. In this case,

$T(r,t)$ is the laser-induced temperature distribution within the processed area of the solid (Sect.2.1). For flat structures, the thickness of the deposited material, or the depth of the etched or transformed pattern, is obtained by integrating (3.5)

$$h(r,t_i) = A_g' \int_{t_n}^{t_i} dt\; k_0(p_i,T(r,t)) \exp[-\Delta E_j/RT(r,t)] \;, \qquad (3.6)$$

where t_i is the laser beam illumination time, and t_n the latent time before the reaction commences. It is important to note that the temperature distribution $T(r,t)$ is an implicit function of the geometry $h(r,t)$, which influences the heat transport from the processed region. The change in temperature during the time t_i may result in a change in the pathway of the chemical reaction, which is then characterized by a different apparent chemical activation energy. This is indicated by the index j in ΔE. In direct writing of patterns, the integral in (3.6) must be extended from $-\infty$ to $+\infty$. However, in most cases, $t_i - t_n$ can be approximated by the dwell time of the laser beam. The absolute value of r in (3.6) is the distance from the center of the cross section of the pattern, while the direction of r is parallel to $v_s \times k_L$ (v_s and k_L are the scanning velocity and the wave vector of the laser beam; as before, we indicate vectors by arrows only if necessary). The influence of scanning on the temperature distribution is not negligible in LCVD, even for small velocities, if $\kappa_D/\kappa_S > 1$. This is due to the interdependence between the geometry of the deposit (which in turn depends on v_s, as shown for example in Fig.5.14) and the temperature distribution, which becomes all the more pronounced with increasing ratio κ_D/κ_S (see Sect.2.1.2). The width of structures can be calculated in analogy to (3.6).

The confinement of the laser-induced temperature distribution, and thereby of the chemical reaction, in pyrolytic microchemical processing, causes some significant differences in comparison to standard large-area processing techniques [3.16]. First, pyrolytic LCP can be performed at much higher partial pressures of reactants. This results in reaction rates that are several orders of magnitude higher than in standard large-area techniques. For example, pyrolytic LCVD can be performed at pressures of up to at least 10^3 mbar (Sect.5.2), while in standard CVD practical partial pressures reach only a few millibars. Due to the uniform heating of the substrate in CVD, higher partial pressures would cause gas-phase nucleation. This would result in uncontrolled deposition. Second, in microchemical processing, three-dimensional diffusion of molecules to and from the reaction zone becomes effective, while in large-area processing only the component normal to the

substrate is relevant. Therefore, transport limitations in LCP will arise only at much higher temperatures, i.e. (3.5) will be valid over a wider temperature range. Clearly, these differences from large-area techniques become more significant as the temperature distribution becomes more localized. Finally, it should be mentioned that the aforementioned advantages of microchemical processing also apply, with some restrictions, to laser-induced large-area processing with a line focus (Fig.4.2b).

We now turn to photolytic gas-phase processing. For negligible divergence of the laser beam away from the substrate, we can assume cylindrical symmetry (this holds as long as the Rayleigh length is much greater than w_0; see Chap.4.2). Then, the density of excited atoms or molecules is given by

$$p = (N_g \sigma_g / h\nu)\, I(r') \;, \qquad (3.7)$$

where σ_g is the gas-phase excitation or dissociation cross section, N_g the number of reactant gas molecules per volume and $I(r')$ the laser intensity at r' within the gas phase. The reaction rate at a point r on the substrate surface due to gas-phase decomposition is obtained by integrating the contributions from the decomposition in the entire gas volume above the substrate [3.17,18]

$$W(r,w_0) = B_g' \frac{sN_g\sigma_g P}{h\nu w_0^2} \int d\phi_a \int dz \int r'dr' \,[z/d^3(r)] \exp[-2r'^2/w_0^2] \;. \qquad (3.8)$$

Here, s is the sticking coefficient of the species incident on the substrate, $d(r)$ is the distance of the volume element dV within the gas phase from the point r on the substrate and ϕ_a is the corresponding azimuth angle. Note that (3.8) does not take into account desorbed species that are not deactivated [3.19]. In the center of the laser focus, i.e. for $r = 0$, (3.8) becomes

$$W(0,w_0) = B_g \frac{sN_g\sigma_g P}{h\nu\, w_0} \;. \qquad (3.9)$$

Comparison of (3.9) and (3.2) shows that the photolytic reaction rates for adsorbed- and gas-phase molecules are $W \propto w_0^{-2}$ and $W \propto w_0^{-1}$, respectively. The additional factor w_0 in (3.9) is due to the fact that species created at distances larger than w_0 are distributed over such a large area that they do not contribute appreciably to the deposition rate in the center of the laser focus. These equations also show that in photolysis gas-phase processes should depend linearly on pressure (if we neglect deactivation of species by collisions), while surface-phase processes should follow adsorption

isotherms, which depend nonlinearly on pressure. Surface-phase processes are sensitive to temperature variations, especially near the gas-liquid coexistence curve, due to variations in the surface coverage θ. Gas-phase processes, on the other hand, are not very sensitive to temperature variations, at least not in the linear growth regime. A further point is that photochemical reactions that involve subsequent collisional reaction partners will generally have reaction orders greater than unity. This means that the molecular densities and coverages appearing in (3.9) and (3.2) must be raised to effective powers greater than unity.

Moreover, it is often difficult to reveal the temperature dependence of the reaction rate and thereby the dominant activation mechanism. In such cases, it is often easier and more enlightening to investigate the wavelength dependence of the reaction rate. For materials with constant absorbance in the spectral region under investigation, such as, for example, metals within the visible spectral range, the total laser power absorbed by the substrate, and therefore the temperature distribution, is independent of the laser wavelength. In this case, the rate of a *thermally* controlled reaction at a gas-solid or gas-liquid interface should remain unchanged.

3.2.2 Mass Transport Limited Region

At high laser intensities, the fundamental limits on heterogeneous reaction rates are determined by mass transport. For the pressures normally used in gas-phase LCP, the ultimate rate is determined by a balance between the gas-phase transport by diffusion of reactants and products into and out of the reaction volume. Here, we disregard surface diffusion of species and convective flow. For large-area planar reactions, this balance is obtained by solving the one-dimensional diffusion equation. As outlined above, the situation is different in microchemical processing. Here, the three-dimensional character of the diffusion of reactants and reaction products becomes relevant. In the following we assume a hemispherical geometry for the zone of diffusive molecule transport, as shown schematically in Fig.3.2. The reaction rate is then proportional to the concentration of reactants within this zone. The concentration outside this zone can be assumed to have a constant value, n_∞.

In the simple case where reactant diffusion is slower than product diffusion, such as in the case of SiH_4 decomposition into Si and H_2, the time-dependent surface-reaction flux, $j(t)$, is given by [3.20]

$$j(t) = \frac{2Dn_\infty}{r_0 + d}\left[1 + \frac{d}{r_0}\exp\left[\left(\frac{1}{r_0} + \frac{1}{d}\right)^2 4Dt\right]\operatorname{erfc}\left[\left(\frac{1}{r_0} + \frac{1}{d}\right)(4Dt)^{1/2}\right]\right] , \quad (3.10)$$

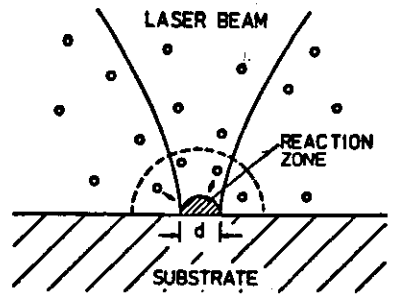

Fig.3.2. Zone of diffusive transport of molecules in laser-induced microchemical processing

where D is the molecular diffusivity, which includes the effect of possible carrier gases. Here, for simplicity, D has been assumed to be constant. In (3.10), $r_0 \equiv 4D/\eta' v_m$ is a length scale proportional to the mean free path in the gas, η' is the reaction efficiency per surface collision, and v_m is the rms velocity of reactant molecules near the surface. Figure 3.3 shows the time evolution of the reaction flux for various values of the reaction zone radius. The conditions chosen are representative for laser-induced CVD and gas-phase etching. The time required to approach steady-state conditions can be specified by

$$\tau_0 = \frac{r_0^2 d^2}{4D(d + r_0)^2} , \quad (3.11)$$

Because $D \sim p^{-1}$, the time τ_0 increases linearly with pressure for small spot sizes, i.e. if $d \ll r_0$, and becomes inversely related to pressure for large spots, i.e. if $d \gg r_0$. The equilibration time τ can be < 10 ns for small spot sizes and moderate pressures (< 1000 mbar). This means that for small spots even pulsed LCP is often in a steady-state condition. Therefore, in

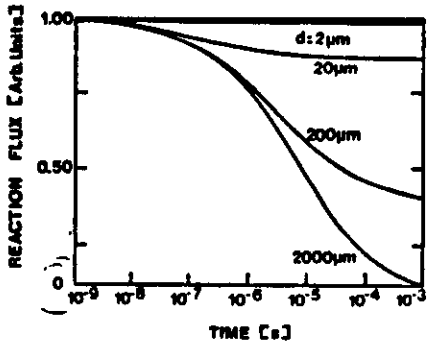

Fig.3.3. Time dependence of the molecular flux into a microreaction zone of width d, p = 133 mbar, T = 1273 K, D = 2.8 cm^2/s, η' = 0.1 (after [3.20])

most cases, deposition or etching is determined by the steady-state solution of the diffusion equation.

The steady-state surface reaction rate is given by

$$j(t \longrightarrow \infty) = 2Dn_\infty /(r_0 + d) \ . \qquad (3.12)$$

If $d \ll r_0$, this rate approaches $2Dn_\infty /r_0 = \eta' v_m n_\infty /2$, i.e. it becomes nearly proportional to pressure, but independent of d. If $d \gg r_0$ the rate saturates and approaches $2Dn_\infty /d$, i.e. it becomes independent of pressure, but decreases with d. The pressure dependence of the steady-state reaction rate is plotted in Fig.3.4 for various radii of the reaction zone. The values chosen are typical for pyrolytic gas-phase processing. The fluxes predicted, e.g. for d = 2 μm and a pressure of 500 mbar, are about 10^{22} molecules/cm^2 s.

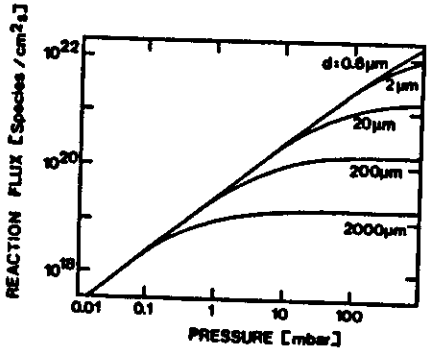

Fig.3.4. Steady-state values for the molecular reaction flux as a function of gas pressure at times $t \gg \tau_0$. $D = \alpha'/p$ with $\alpha' = 2.7 \cdot 10^2$ mbar cm^2/s, $r_0 = \beta'/p$ with $\beta' = 6.7 \cdot 10^{-2}$ mbar cm, $T = 1273$ K, $\eta' = 0.1$ (after [3.20])

This corresponds to a deposition or etch rate of several 10^3 μm/s. This rate is sufficient to explain the tremendous deposition and etch rates achieved in laser-induced microchemical processing (Chaps.5 and 8). It should be mentioned that for a comparison of reaction rates that can be achieved in laser-induced microchemical processing and in standard large-area techniques, one must take into account the fact that standard processing is often performed in flushed reactors. In such cases, diffusive transport need only occur across a thin boundary layer that has a typical width of $\delta = 3$ mm. The enhancement in laser microchemical processing is of the order of $2\delta/d$; for d = 2 μm, this factor is 10^3. It should be noted that at very low partial pressures of reactant molecules the dominant mass transport mechanism need not be gas-phase diffusion, but can instead be diffusion of adsorbed molecules along the substrate surface (Sect.3.1). At very high molecular densities, on the other hand, mass transport by convection may become important (Sect.3.3).

The reaction rates achieved in gas-phase LCP are often well below the transport-limited rates discussed above. This is especially true in photolytic processing when the laser light is absorbed within the gas phase. Here, the rate is commonly restricted by gas-phase nucleation or recombination (see Chaps.5 and 8). Gas-phase nucleation or recombination, however, can only be controlled by reducing the atomic or molecular density. Sometimes the same effect can be achieved by inert-gas buffering. In any case, this results in a lowering of deposition or etch rates. In photolytic LCP the reaction rates may be even further limited by the available laser power and/or the mismatch of the laser wavelength and the maxima in the absorption cross section of reactant molecules.

3.2.3 Solid Surface Excitations

So far we have discussed reaction rates based on laser-induced substrate heating or on direct photochemical dissociation of adsorbed- or gas-phase species. There are, however, a great number of other effects that may significantly influence laser-induced reaction rates at gas-solid interfaces. Among those are autocatalytic effects and dissociative photoelectron capture [3.21]. Both effects have been studied in connection with metal deposition [3.22,23]. In semiconductors and insulators, the excitation of the band gap may cause a nonthermal increase in reaction rates. This effect has been studied in some detail in connection with dry- and wet-etching of Si and GaAs (Chap.8). Another effect, which has already been mentioned in Sect.3.1, is the electromagnetic field enhancement on metal and semiconductor surfaces [3.7-10,24,25]. This effect can significantly alter reaction rates in gas-phase deposition, surface modification and etching reactions. Strong surface electric fields induced by the incident laser radiation may significantly increase surface adsorption and diffusion of species into the solid surface [3.24-26]. This mechanism has been proved to be particularly important in connection with surface oxidation and etching reactions in a halogen atmosphere (Sects.6.1 and 8.2). While some initial studies of these different mechanisms have been performed already, detailed investigations are still lacking. Furthermore, it should be emphasized that a separate discussion of single effects greatly oversimplifies the situation of chemical reactions at gas-solid interfaces. A more satisfactory understanding requires consideration of chemical phenomena in the gas, adsorbed and solid phases and, in addition, the often subtle interactions between these three phases. Furthermore, as already pointed out in various sections, during deposition, doping, etching, etc. the morphology and physical properties of the surface

material. This is generally the case in conventional laser machining (cutting, drilling, etc.) as described in Chap.1. The situation becomes much more complex when a material surface is irradiated with short but very intense laser pulses. Detailed investigations of this kind have been carried out for a great number of materials [3.40-43]. In this regime, laser-induced ablation has been termed laser sputtering. Laser sputtering cannot always be explained on the basis of a thermal model only.

Direct nonthermal bond breaking seems to be the dominating mechanism in ablative photodecomposition (APD) of organic polymers and biological materials under ArF laser irradiation [3.44-50]. For wavelengths $\lambda < 200$ nm, organic polymers have a very high absorption coefficient, which is typically of the order of $5 \cdot 10^3$ to 10^5 cm^{-1}. Therefore, the absorbed energy is essentially deposited within a 2 to 0.1 μm thick layer. The UV radiation may excite the organic molecule to above the dissociation limit (Fig.2.15b) or to an upper bound state from which, due to crossing into another unstable or less stable electronic state, dissociation can occur (Figs.2.15c,d). For wavelengths $\lambda < 200$ nm, the dissociation of bonds is extremely efficient, typically larger than 50%. Nevertheless, intersystem crossing or internal conversion can also lead to electronic deexcitation via vibrational relaxation and thereby to a dissipation of the excitation energy into heat. Ablation of polymers with visible and IR radiation has been demonstrated as well. Here, melting and vaporization of the material seems to be the dominating mechanism.

Laser ablation of organic polymers has been modeled for both photochemical and photothermal processes [3.44-50]. According to the model of GARRISON and SRINIVASAN [3.48], photochemical ablation will occur via fragmentation of the polymer into monomers, which, because of their larger specific volume, interact among themselves and with the remaining material via a repulsive potential. This results in a volume explosion (on a picosecond time scale) without melting. The reaction products will be ejected from the photolyzed area at a very high speed (estimated as 10^5-$2 \cdot 10^5$ cm/s) and into a small solid angle within about 30^0 of the surface normal. For photon energies less than typical bond energies (which are about 6.0 to 2.5 eV for the materials under consideration), corresponding to wavelengths $\lambda > 200$ to 500 nm, single-photon dissociation becomes impossible. Thus, in this wavelength region, ablation may occur either via sequential multiphoton excitation or via heating, melting and evaporation. In the latter case, the predicted angular distribution of the ablated material becomes very broad, out to more than 60^0 from the surface normal. While many characteristics of APD of organic

polymers (Sect.8.4) support a nonthermal bond-breaking mechanism, there are other observations that suggest a mostly statistical thermodynamic process, with transient melting but without complete energy randomization [3.51,52,55]. However, it seems to be clear that the dominating mechanisms depend on the specific material under investigation, as well as on the laser fluence, wavelength and pulse width. In fact, a novel dynamic model has recently been elaborated to allow a consistent analysis of thermal and nonthermal contributions to APD, including the description of fluence thresholds, incubation pulses, fast intra-pulse etching etc. [3.45].

The processes outlined in this section may be performed in a nonreactive atmosphere. Nevertheless, reactive surroundings, for example air or oxygen, may affect the reaction rates and chemistry.

3.5 Spatial Confinement

The spatial confinement of laser-induced chemical reactions at interfaces is determined by

1. The laser beam spot size
2. The spatial confinement of the laser light-induced excitation
3. Laser light-induced disturbances of the surrounding medium
4. The nonlinearity of the surface chemical process itself

The single points will now be discussed in greater detail. Normal incidence of the laser beam onto the substrate is assumed.

For a Gaussian beam, the diffraction-limited diameter of the laser focus is given by $2w_0 = 4f\lambda/\pi a = 1.3\, f\lambda/a$ (Sect.4.2). For $f/a = 1.5$ optics, we obtain $2w_0^{min} = 2\lambda$, i.e. for 500 nm radiation, the minimum laser spot size becomes about 1 μm (index of refraction $n = 1$).

The confinement of the laser-induced excitation within the gas or liquid phase, on the substrate surface and in its bulk, is also of considerable importance. Consider, for example, species that are photoexcited or dissociated within the gas or liquid phase. Such species will randomly diffuse towards the solid surface. Consequently, deposition on, or etching of areas beyond the focal point region will occur. The spatial resolution is thereby decreased. This problem can be overcome, in part, by a careful selection of the processing parameters. In pyrolytic processing from the gas or liquid phase, photothermal or photochemical excitation within the volume of the laser beam can be avoided to a large extent by a proper choice of the laser wavelength and irradiance. In photochemical gas- or liquid-phase

processing, confinement of the reaction to the substrate surface would be possible only if the dissociative continuum of the adsorbed molecules shifted considerably towards red, so that proper selection of the laser wavelength would allow adsorbed-phase but not gas- or liquid-phase photolysis (see Sect.3.1). In spite of the fact that a shift of the dissociative continuum of adsorbed species with respect to gas- or liquid-phase molecules plays an important role in many systems investigated in LCP, photoexcitation or dissociation within the total volume of the incident laser beam was observed in essentially all cases investigated in photolytic LCP. However, tight focusing of the laser beam not only limits the area of excitation on the substrate, but also confines the relevant volume of excitation within the adjacent surrounding medium. See Sect.3.2 and (4.3). Species that are generated at a distance larger than their mean free path for deactivation (by collisional recombination with complementary photofragments, or reactions with parent or other molecules) will not reach the substrate. In other words, the flux of species to the substrate is limited to a small region around the laser spot. The rate of recombination depends not only on the type and density of molecules in the ambient medium but also on the incident light flux. In gas-phase processing, the confinement of the reaction volume can sometimes be further enhanced by proper selection of the type of buffer gas and the respective partial pressures of gaseous constituents. Low partial pressures of reactants and the admixture of adequate buffer gases may improve the localization but decrease the efficiency of the photodeposition or etching process.

Apart from homogeneous gas- or liquid-phase excitations, there are additional mechanisms that may decrease the spatial confinement. Among these are: thermal diffusion and diffusion of photoexcited carriers within the substrate or, in the case of deposition, within the already deposited material; diffusion of adsorbed reactant species or of photofragments produced on the substrate surface itself, etc. For the broad range of experimental conditions used (Chaps.5-8) the corresponding diffusion lengths may be smaller, comparable or larger than $2w_0^{min}$. In any case, these different mechanisms may decrease the spatial confinement of processing, depending on the parameters used. Reliable estimates are very difficult for many reasons, including: the difficulty of ensuring a correct treatment of the strong temperature gradients in pyrolytic LCP; the unknown bulk and surface properties of the material within the processed region; the lack of reliable data on the corresponding parameters such as gas, surface, and bulk diffusion coefficients, characteristic lifetimes, etc.

Laser light induced disturbances within the surrounding medium may substantially decrease the spatial confinement of the reaction. Strong temperature inhomogeneities in pyrolytic LCP may change the optical index of refraction, cause convection, turbulence or even bubbling. These effects are especially pronounced in dense media (Sect.3.3). In photolytic LCP, the formation of clusters and the coating of entrance windows may attenuate and scatter the incident light.

From the above considerations, one would expect that the minimum lateral dimensions, d_{min}, of laser light generated structures to be $d_{min} > 2\,w_0^{min}$. On the other hand, it has been demonstrated that laser direct writing allows one to generate structures with $d < 2w_0$ (Sect.5.2). In other words, it is possible to produce patterns with lateral dimensions smaller than the diffraction-limited diameter of the laser focus. This shows the importance of process nonlinearities, which have been discussed in the foregoing sections.

To illustrate the influence of nonlinearities in pyrolytic LCP, we have plotted in Fig.3.6 a temperature profile (full curve) induced by a Gaussian laser beam (dotted curve) on a semiinfinite substrate. The figure also shows the normalized reaction rates, $W(r) = \exp[-\Delta E/kT(r)]$, for two different chemical activation energies $\Delta E = 22$ kcal/mole (curve a) and $\Delta E = 46.6$ kcal/mole (curve b). These activation energies correspond, for example, to those in laser-induced deposition of Ni and Si from $Ni(CO)_4$ and SiH_4, respectively (Sect.5.2). Note, however, that the influence of the laser-processed feature on the temperature distribution was not taken into account here. In laser-induced deposition, this approximation is valid only if the

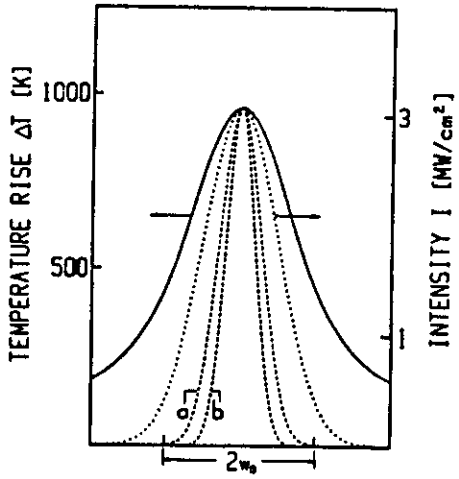

Fig.3.6. Confinement of the chemical reaction in pyrolytic processing. Dotted curve: Profile of the laser beam. Full curve: Temperature rise calculated for $\kappa = 50$ W/mK and an absorbed laser power $P_{abs} = 0.3$ W (surface absorption). The normalized reaction rate is obtained by exponentiating the temperature distribution. Dashed curves refer to apparent chemical activation energies of $\Delta E = 22$ kcal/mole (curve a) and $\Delta E = 46.6$ kcal/mole (curve b)

equal, i.e. if $\kappa_D/\kappa_S = 1$ (see Sect.2.1.2). In spite of this restriction in generality, the figure shows some interesting features. The nonlinear dependence of the reaction rate on temperature causes the lateral variation in W to be substantially narrower than in T. The spatial confinement of the reaction increases with increasing apparent chemical activation energy ΔE (compare the dashed curves a and b). When a particular material has to be deposited, however, there is in many cases no choice of parent molecules. One of the exceptions is Si, which can be deposited from either SiH_4 or $SiCl_4$, which have somewhat different activation energies.

The influence of ΔE and of the center temperature will now be studied in more detail. Let us describe the increase in spatial confinement by the ratio w_0/r_e, where $r_e = d_e/2$ is given by the 1/e point in the reaction rate W(r). For temperature-independent parameters, we obtain from (2.7) and (2.10)

$$T(r) = T_0 + \Delta T(r) = T_0 + \Delta T_c\, f(r) \quad , \quad \text{with} \tag{3.18}$$

$$f(r) = 2\pi^{-1} \int_0^\infty g(u)\, du \quad .$$

The above definition then yields

$$r_e = \tilde{f}\left(\frac{1 - T_0 R(1 + T_0/\Delta T_c)/\Delta E}{1 + T_0 R(1 + \Delta T_c/T_0)/\Delta E} \right) \equiv \tilde{f}(\gamma) \quad , \tag{3.19}$$

where $\tilde{f}(\gamma)$ is the inverse function of f(r). In Fig.3.7 we have plotted the ratio w_0/r_e as a function of ΔT_c for various activation energies ΔE. The figure shows that the confinement increases very rapidly with increasing ΔE at low values of ΔE, and much more slowly at higher values. Furthermore, for a certain value of ΔE, there exists a maximal value of w_0/r_e at a certain center temperature $T_c^m = T_0 + \Delta T_c^m$. Clearly, for efficient processing, the practical center temperature, T_c^p, must be well above the threshold temperature for deposition, etching, etc., because otherwise the reaction rate would be extremely small. In many cases, $T_c^p > T_c^m$ and the confinement will be decreased with respect to the optimal value. Besides the mechanisms which decrease the spatial confinement with respect to that expected from Fig.3.7, and which have been discussed above, there are additional fundamental mechanisms that also limit the ultimate resolution of structures. These will be discussed in Sect.5.2.5 in connection with laser direct writing.

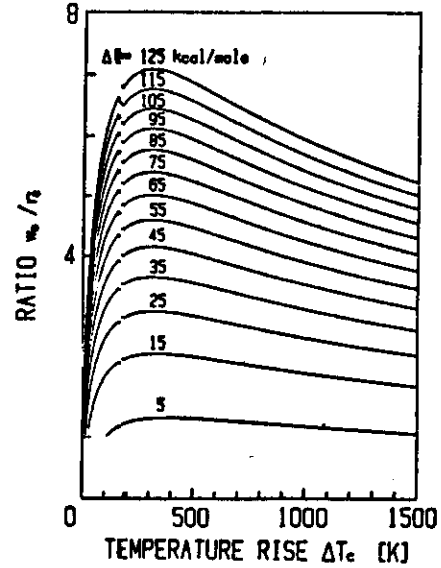

Fig.3.7. Ratio w_0/r_e, r_e is defined by the 1/e point in reaction rate W(r), plotted as a function of the laser-induced center temperature rise for various activation energies ΔE. Note that changes in geometry, for example due to deposition or etching, and/or in physical parameters are not taken into account (after [3.53])

In laser photolysis, based on multiphoton dissociation of adsorbed molecules, the reaction rate is given by $W \propto P^n$, where n is the number of coherently absorbed photons (Sect.2.2). This nonlinearity increases the confinement in photolytic processing.

Whenever nucleation processes are involved in a particular processing step, such as in deposition or compound formation, they will be of great importance for the confinement of the chemical reaction. The reason is the strong nonlinearity of the nucleation process itself [3.54]. This nonlinearity is, of course, independent of whether species are generated by pyrolytic or photolytic processes. Nucleation processes can take place within the surrounding medium, as in the gas phase, on the substrate surface or, as in compound formation, within solid films. Nucleation will be discussed in Sect.5.1 in more detail.

The analysis of the microscopic mechanisms in the initial phase of growth is very complicated. In the phase of nucleation, we have to consider two cases: First, strongly absorbing substrates, and second, transparent substrates that do not absorb the laser light, or else do so only very slightly.

In the first case the molecules are thermally dissociated near the hot spot that is produced on the substrate by the absorbed laser light. The free atoms form clusters, which provide nucleation centers for further film growth. Under most processing conditions, the time of nucleation t_n is very small compared to the laser beam illumination times t_i that we shall henceforth be considering. The main differences from nucleation in large-area thin film growth techniques such as standard CVD [5.187], arise from the confinement of the temperature distribution and the related strong temperature gradients that are produced on the substrate surface. A further difference from CVD is based on the rapid change in the local laser-induced temperature distribution due to changes in reflectivity and thermal conductivity provided by the nuclei.

For transparent substrates, the situation is even more complex. Here, surface defects such as pinholes and scratches or dust particles may absorb the laser light and thereby allow nucleation to be initiated at certain places on the substrate surface. The mechanism is then very similar to that mentioned in the preceding paragraph. The situation becomes quite different when nucleation is initiated by atoms that result from nonthermal (single- or multiphoton) dissociation of adsorbed molecules (see Fig.5.1). It is clear

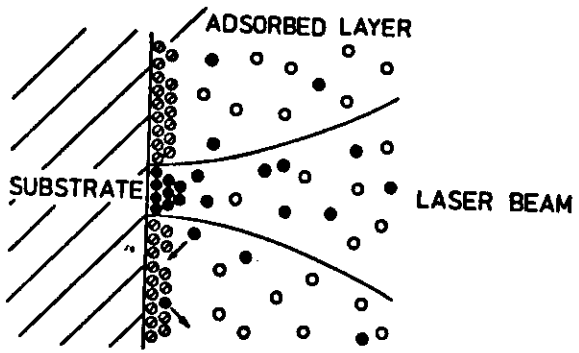

Fig.5.1. Schematic showing the influence of adsorbed-layer photochemistry on nucleation and condensation of gas-phase photofragments. Empty and crossed circles indicate free gas-phase and adsorbed precursor molecules, and full circles photofragments

that in such cases changes in the electronic properties of molecules due to adsorption, especially a shift and a broadening of the dissociative continuum, are of fundamental importance (Sect.3.1). Because of the high density of adsorbed molecules, the free atoms may form clusters, which, even when of subcritical size, may strongly absorb the laser radiation. Such heated clusters will then provide nucleation sites and film growth will proceed mainly thermally. In this case t_n is heavily dependent on the laser wavelength and may last several seconds or even minutes. The first evidence for such processes was obtained during deposition of Cd, Al and Ni from the alkyls and carbonyls, respectively [5.10,14,65,105,106]. In any case, nucleation will cause not only a latent time, but also a threshold intensity for deposition.

In photolytic processing, where further film growth proceeds by mainly nonthermal dissociation of molecules, such multiatom clusters, irrespective of whether they were originally formed by thermal or nonthermal dissociation of species, may serve as nucleation centers for further film growth. An example is the deposition of metal microstructures produced by gas-phase dissociation of the corresponding alkyls or carbonyls by means of UV laser radiation (Sects.2.2.1 and 5.2). Here, in spite of the fact that metal atoms are produced within the total volume of the laser beam, condensation of atoms reaching the solid surface preferentially occurs at the nuclei produced within the area of the laser focus. This is schematically shown in Fig.5.1. Atoms that do not form stable nuclei (for Cd, the critical number of atoms, N_c, that is necessary for a stable nucleus is about 10 at 300 K; for nuclei adsorbed on substrate surfaces, this number also depends on the physical properties of the substrate) or attach themselves to these nucleation centers formed within the area of the laser focus, will diffuse across the surface and then evaporate. If an atom falls within a surface diffusion length $l = (2D\tau)^{1/2}$ (D is the surface diffusion coefficient of the atom and τ the characteristic time of reevaporation; the exact result depends on the size of the nucleus.) of a stable nucleus, it will, on average, be captured by this nucleus; if the atom falls outside this zone, it will reevaporate prior to capture. In other words, the sticking probability for free gas- or liquid-phase atoms or small clusters of atoms impinging on or near the nuclei formed within the irradiated substrate area is much larger than anywhere else on the substrate surface. Thus, nucleation thresholds improve the contrast in photolytic deposition, i.e. isotropic deposition occurs only to a small extent. The foregoing remarks show that we are a long way from an understanding of the initial dissociation and nucleation processes in laser-induced deposition.

In the following sections we will discuss pyrolytic and photolytic deposition of microstructures from adsorbed layers and from the gas, liquid and solid phases. For the reasons outlined in Sect.4.2, most of the experiments have been performed with cw lasers such as Ar^+ and Kr^+ lasers, including their harmonic lines.

5.2.1 Deposition from Adsorbed Layers

Some of the materials listed in Table 5.1 can be photochemically deposited from adsorbate-adsorbent systems under vacuum. Here, strong physisorption of the parent molecules, and little or no substrate heating by the incident laser light is required. Under these conditions, thermal desorption of the adsorbed molecules may be slow enough to allow photodeposition. This was investigated in some detail for Ni, Cd and Al deposited from metal-organic compounds on substrates such as glass, SiO_2 and Al_2O_3.

Nickel has been deposited by irradiating the substrates with 356 nm or 476 nm Kr^+ laser light [5.105,106]. The substrates were first exposed to a $Ni(CO)_4$ atmosphere of several millibars for 5-20 minutes. After this time several cycles of pumping and purging with He or H_2 followed. As expected from the increase in absorption of $Ni(CO)_4$, the latent times were much longer for 476 nm than for 356 nm radiation. Similarly, Cd and Al have been deposited from adsorbed $Cd(CH_3)_2$ and $Al_2(CH_3)_6$. These experiments were mainly performed with 193 nm ArF [5.4], 257 nm frequency-doubled Ar^+ [5.14,60,61], and 356 nm Kr^+ [5.65] laser radiation. Very interesting information on the deposition of Al on c-Al_2O_3 has been obtained from pulsed optoacoustic (IR) spectroscopy [5.4]. These investigations have shown that high quantum yield nonthermal photodesorption of CH_3 groups incorporated in the already deposited Al films can be achieved with 193 nm ArF but not with 248 nm KrF laser radiation. Consequently, Al films grown from adsorbed layers with ArF laser light contain only low amounts of CH_3 contamination and are therefore of high quality. In any case, the thickness of layers deposited from adsorbate-adsorbent systems under vacuum is extremely small.

The contribution to the photodeposition rate of adsorbed layers that are in dynamic equilibrium with a surrounding gas phase has been studied for a number of systems [5.4,16,17,23,188]. As outlined in Sects.3.1 and 3.2, see (3.2) and (3.8,9), the relative importance of adsorbed-phase and gas-phase contributions can be discovered by investigating deposition rates as functions of laser focus diameter, substrate temperature and gas pressure.

has been studied for the deposition of Cd on SiO_2 substrates with 257 nm frequency-doubled Ar^+ laser radiation [5.58,59]. From these investigations it was concluded that the decomposition of $Cd(CH_3)_2$ occurs mainly in the gas phase. For other systems, however, the importance of adsorbed-layer photochemistry for deposition rates was proved from the influence of the substrate temperature. An example is the deposition of Al from $Al_2(CH_3)_6$ on quartz substrates [5.16,17,23]. Between 320 K and 280 K the deposition rate was found to increase with decreasing substrate temperature due to the increase in $Al_2(CH_3)_6$ coverage (Sect.3.1). Below the freezing point of the adsorbed layer, however, a decrease in the photodeposition rate was observed. This was interpreted in terms of an increase in photofragment recombination efficiency and by reduced molecular and atomic surface mobilities. Similar results have been obtained for the deposition of Ti from $TiCl_4$. In this latter system, however, the surface reaction is more complicated and seems to involve autocatalytic effects that arise from the deposited film itself. Further evidence for the importance of adsorbed layer photochemistry was obtained from the dependence of the Ti deposition rate on $TiCl_4$ pressure.

Multimolecular surface photochemistry was investigated for UV laser photopolymerization of methyl methacrylate (MMA) into poly-MMA (PMMA) [5.16,17]. This technique allows local deposition of moderate-molecular-weight PMMA. The photochemical mechanism is a free radical-catalyzed polymerization initiated by absorption of UV laser light by the volatile molecular layers that form on surfaces exposed to an ambient MMA vapor. The rapid collisions of vapor-phase molecules with the surface continually replenish the polymerizing adsorbed MMA and thereby permit rapid PMMA growth.

Photodissociation of adsorbed layers can also be used to prenucleate condensation areas, which are filled up later by large-area standard CVD or by pyrolytic LCVD. This combined technique allows maskless deposition of thin-film microstructures with much higher rates than those achieved in photolytic LCVD. Investigations of this kind have been performed mainly for Al deposited from $Al(C_4H_9)_3$ [5.16,17].

The influence of local electric field enhancement (Sect.3.1) due to surface contouring has been studied in particular for Cd deposition [5.60,61]. These experiments used predeposited Cd spheres on C films. Cadmium was used for contouring because it possesses a plasma resonance in the appropriate ultraviolet spectral region. After covering the surface with a thin adlayer of $Cd(CH_3)_2$, which was in dynamic equilibrium with an atmosphere of 1.33 mbar $Cd(CH_3)_2$ and 1330 mbar Ar, the substrate was irradiated with 257

nm laser light. The growth pattern of the elliptical particles that grew from the spheres is in agreement with the theoretical model also presented in [5.60,61].

5.2.2 Gas-Phase Deposition

In this section we will discuss the production of microstructures in the form of spots, stripes and rods based on pyrolytic and photolytic laser-induced deposition from the gas phase, henceforth denoted by LCVD.

a) Pyrolytic LCVD

Investigations on the pyrolytic growth of spots are the simplest way of testing the adequacy of the model calculations presented in Sect.2.1.2 for the description of pyrolytic LCVD. The results also allow an understanding of the initial phase of the growth of rods (see below). For photolytic deposition, a quantitative or semiquantitative description has not yet been produced. Steady growth of stripes is relevant in pyrolytic and photolytic direct writing of microstructures. The following discussion concentrates on model systems for which the most complete data are available. Similar, but less detailed, investigations have been performed for the other materials listed in Table 5.1.

Deposition of Spots

When a Gaussian laser beam is focused onto an absorbing substrate (Fig.4.2a) that is immersed in one of the compounds listed in Table 5.1, and both the laser beam and the substrate are at rest, one initially observes the deposition of a circular spot. The most-detailed investigations on pyrolytic growth of spots have been performed by BÄUERLE and co-workers for Ni and Si deposited from $Ni(CO)_4$ and SiH_4, respectively.

Figures 5.2a,b show scanning electron micrographs of Ni spots deposited with 647 nm Kr^+ laser radiation. For the series of spots shown in Fig.5.2b, the laser power was held constant while the laser beam illumination time, t_i, was increased for each successive spot, working upwards from the bottom. The substrate material was glass covered with a 1000 Å a-Si layer. Such a substrate strongly absorbs the visible laser radiation and has a much smaller thermal conductivity than the deposit (Fig.2.11a). For such a substrate, the nucleation time t_n is very small compared to the laser beam illumination time t_i, i.e. $t_n \ll t_i$, and the spots grow very rapidly with t_i to radii much larger than the laser focus. Such large spot sizes can easily be measured and the high growth rates enable much data to be accumulated. Such experiments

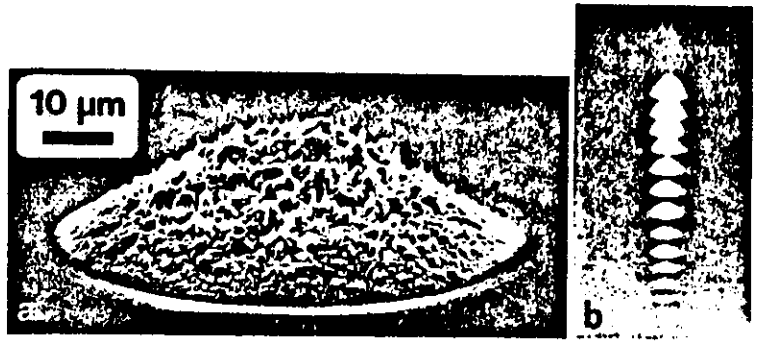

Fig.5.2a,b. Scanning electron micrographs of Ni spots deposited from $Ni(CO)_4$ by 647 nm Kr^+ laser radiation. The substrate was glass covered with a 1000 Å a-Si layer. (a) Typical shape of a spot. (b) Series of spots deposited at constant laser power with increasing laser beam illumination time for each successive spot, working upwards from the bottom. The micrograph was taken at glancing incidence (after [5.48,108])

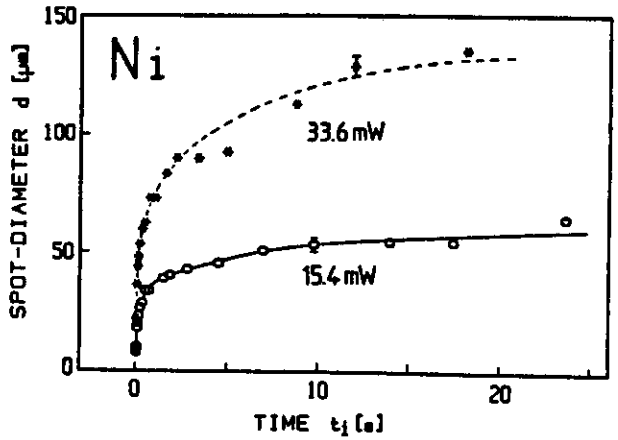

Fig.5.3. Diameter of Ni spots as a function of laser beam illumination time for two powers of the 647 nm Kr^+ laser line. $2w_0 = 6$ µm, $p_{tot} \equiv p(Ni(CO)_4) = 200$ mbar. The broken curve is a guide for the eye. The full curve has been calculated from (5.1) (after [5.48])

are therefore predestinated to be used to investigate the growth kinetics in pyrolytic laser-induced deposition. This will now be outlined in greater detail.

Figure 5.3 shows the diameter of Ni spots as a function of t_i for two laser powers and a total gas pressure $p_{tot} \equiv p(Ni(CO)_4) = 200$ mbar [5.48,108,190]. The figure shows that the condition $d > 2w_0$ (Sect.2.1.2) is

fulfilled for all but the shortest time in the 15.4 mW curve. The spot diameter first increases very rapidly for a few tenths of a second and then nearly saturates for times t_1 ≈ 1 to 10 s, depending on the laser power. Because the temperature rise $\Delta T(d/2)$ decreases approximately inversely with the spot diameter, see (2.19), this saturation can be explained by the exponential dependence of the deposition rate on temperature, which yields an apparent threshold below which deposition is negligible (Sect.3.2). However, this saturation may also be due to a real threshold originating from nucleation processes. The mechanism could be checked by depositing the same material from reactant molecules with different activation energies. An example is Si, which can be deposited either from SiH_4 or from $SiCl_4$.

Experimental results like those presented in Fig.5.3 enable the radial growth rates $v \equiv \Delta d/2\Delta t$ of Ni spots to be calculated by numerical differentiation. It is clear from the shape of the spots that the lateral growth velocity v (oriented within the substrate surface) is not parallel to the deposition rate W (defined as the rate of translation of a surface element along its perpendicular) at the edge of the spot. However, because spots grown with different laser powers remain similar in shape, W and v differ only by a factor which is roughly constant. In any case, the exponential dependence of the growth rate on temperature will dominate any temperature dependence of the pre-exponential factor k_0 in (3.5). In other words, if the growth of Ni spots is *thermally* activated, the lateral growth velocity, v, should follow an Arrhenius type behavior. Figure 5.4 shows such an Arrhenius plot in which additional experimental data for different laser powers and laser focus diameters have been included. The plotted temperature was that at the edge of the deposit, which was calculated as described in Sect.2.1.2. The values used for the thermal conductivities correspond to those in Fig.2.11a. The high temperature region of very fast growth corresponds to small spot sizes, the low temperature region with much smaller growth rates to larger spot sizes. The full line represents a least-squares fit to the low temperature data and shows the exponential dependence of the lateral growth rate on temperature. The apparent activation energy derived from the figure is ΔE_1 = 22 ± 3 kcal/mole. This value is, within the accuracy of the measurements, independent of P and w_0. This supports the idea that the lateral growth rate depends only on the local temperature rise. The main systematic error in the calculated temperatures, and consequently in the activation energy, arises from the uncertainty regarding the reflectivity of the deposited material, R_D, which was measured in situ and found to be R_D = 0.2 ± 0.1. For the limiting values R_D = 0.3 and 0.1 we obtain ΔE_1 = 18 and 31

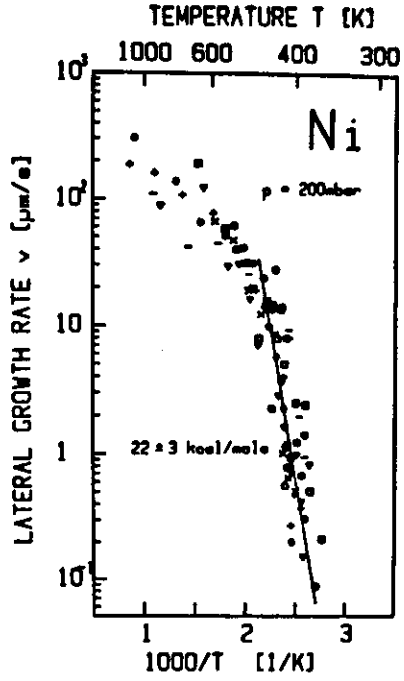

Fig.5.4. Arrhenius plot for lateral growth rate v of Ni spots. The full line is a least-squares fit to the low temperature data. The different symbols refer to different laser powers and focus diameters (after [5.108])

kcal/mole, respectively. These values are within the range of apparent chemical activation energies reported for large-area heterogeneous deposition of Ni from $Ni(CO)_4$ [5.191-194]. The investigations that covered the widest temperature region (350K < T < 430K) gave 22 kcal/mole [5.192]. This latter value effectively corresponds to the energy required for the removal of the first CO group from the $Ni(CO)_4$ molecule and it is in excellent agreement with the activation energy derived from Fig.5.4. The marked decrease in slope appearing in the figure above the temperature T_b ≈ 500 K could have various origins. For example it might indicate the limits of the model calculations, which are adequate only if $d > 2w_0$. Another possibility, which at present seems very likely, is the change in reflectance of the Ni spot that may occur for the very shortest times t_1. However, the decrease in slope could also indicate limitations in the gas-phase transport of reactant molecules or reaction products or in the desorption of CO (Sects.3.1,2). Another reason could be that other chemical reaction pathways, characterized by an apparent activation energy ΔE_2, may become possible at higher temperatures.

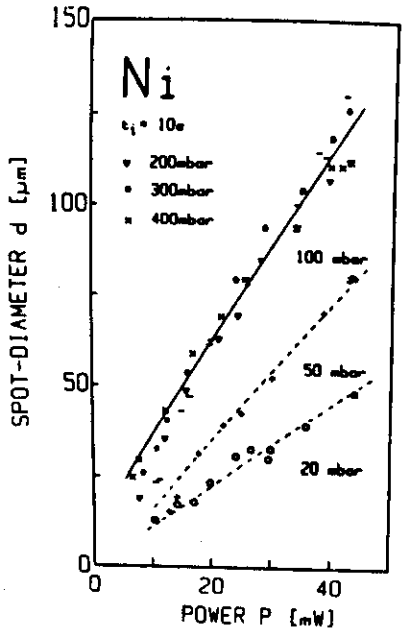

Fig.5.5. Dependence of Ni spot diameter on laser power for various gas pressures and constant laser beam illumination time t_i = 10 s. λ = 647 nm Kr^+, $2w_0$ = 6 µm. The full line was calculated from (5.1). The dashed lines are guides for the eye (after [5.108])

Figure 5.5 shows the diameter of Ni spots for constant laser beam illumination time t_i = 10 s, as a function of laser power and for different gas pressures. The saturation in growth observed for higher gas pressures is expected for a heterogeneous chemical reaction and is described by the pressure dependence of k_0 in (3.5). From Fig.5.5 we find k_0 = 1 for p > 100 mbar. The diameter of Ni spots can be calculated in a comparable way to (3.6) from

$$d(t_i) = d(t_m) + 2A \int_{t_m}^{t_i} dt\, k_0(p,T(t)) \exp[-\Delta E_j/RT(t)] \,. \qquad (5.1)$$

Here, $\Delta E_j \equiv \Delta E_1$ and $\Delta E_j \equiv \Delta E_2$ are the apparent activation energies in the low and high temperature regions, i.e. below and above T_b, respectively. It is clear from Sect.2.1.2 that the temperature T itself depends on the spot diameter and is therefore a function of time. The lower integration limit in (5.1) is the time for which the assumption $d(t_m) > 2w_0$ is fulfilled (Sect.2.1.2). For all but the lowest laser powers we find $t_m << t_i$ = 10 s. For p = 200 mbar, we can derive the activation energies and the constant A from Fig.5.4. Integration of (5.1) can be performed by assuming $d(t_m) = 2w_0$. Note that $d(t_i) >> 2w_0$. The integration shows that d increases quasi-linearly with laser power for P < 60 mW. This result is included in Fig.5.5 by the

full curve. The agreement with the experimental data is excellent and shows the consistency of the procedure. It can easily be shown that contrary to the value of ΔE_1, the (larger) uncertainty in ΔE_2 does not appreciably influence the result. A further proof of the consistency of the procedure is obtained when calculating from (5.1) the time dependence of the spot diameter (full curve in Fig.5.3).

We now compare the pressure dependence of the spot diameter for constant t_i and constant laser power (Fig.5.5) with the reaction kinetics derived by CARLTON and OXLEY [5.192]. Here, it is essential to take into account that in the experiments described above, the partial pressure of CO is negligible compared to that of $Ni(CO)_4$. According to [5.192] the pre-exponential factor in the rate equation (3.5) is then given by

$$k_0(p(Ni(CO)_4),T) = k^2p^2/(1 + kp)^2 \,, \qquad (5.2)$$

with $k = 0.067 \exp(T_1/T)$ mbar^{-1} and T_1 = 352 K. Saturation should occur if kp >> 1. For a laser power of P = 30 mW, saturation of the spot diameter would therefore be expected (within 3%) for a pressure of p = 50 mbar. Clearly, only a qualitative agreement with the experimentally observed pressure dependence shown in Fig.5.5 can be expected, for several reasons: the difference between W and v enters the pre-exponential factor that has been determined only for p = 200 mbar (Fig.5.4); the factor k depends on temperature and thereby on the diameter of the spot. The apparent and perhaps even the true order of reaction may change with pressure - as well as with temperature. This may also explain the considerable differences reported in the literature for the form of k_0 and the entering parameters (see (5.2) and [5.191-194]).

Steady Growth of Rods

As outlined above, radial growth of pyrolytically deposited spots saturates with laser beam illumination time t_i (Fig.5.3). Simultaneously with this saturation, an increase in axial growth is observed. Consequently, for longer times t_i, the growth of a rod along the axis of the laser focus is observed. The growth of rods has been investigated for various different materials by BÄUERLE et al. [5.48,49,51,104,105,123,124,126,170,195]. A typical example of a rod is shown in Fig.5.6 for the case of Si deposited from SiH_4. Two phases of growth can be observed. Near the onset, the deposition rate depends strongly on the physical properties of the substrate. This phase of growth corresponds with the growth of spots and has already been discussed. In steady growth, which is characterized in Fig.5.6 by a constant rod diameter,

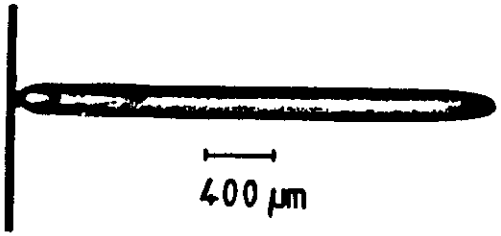

Fig.5.6. Silicon rod grown from SiH_4 with 488 nm Ar^+ laser radiation. P = 400 mW, $p_{tot} \equiv p(SiH_4)$ = 133 mbar (after [5.50])

the deposition rate is independent of the substrate material. Therefore, in contrast to the growth of spots, the temperature profile in the tip of the rod is independent of time, i.e. T = T(r), if the laser irradiance is held constant. The constant rod diameter is a consequence of the threshold in lateral growth - as discussed above. It is clear from the shape of the rod that in steady growth, the maximum growth rate is at the center of the tip and identical with the axial growth velocity. Therefore, the deposition rate can be defined by the growth of the length of the rod per unit time

$$W(T) \equiv v(r = 0,T) = \Delta h(r = 0,T)/\Delta t \ . \qquad (5.3)$$

The surface temperature at the center of the tip of the rod, T, can be measured as described in Sect.4.4 (see also [5.51,196]). Figure 5.7 shows an Arrhenius plot for the deposition of Si from SiH_4. The upper curve refers to data obtained from pyrolytic LCVD of rods. In the kinetically controlled regime, which reaches up to about 1400 K, the deposition rate increases exponentially with temperature and is characterized by an apparent chemical activation energy of ΔE = 44 ± 4 kcal/mole [this value is *not* corrected for the temperature dependence of k_0 (see (3.5) and [5.51])]. The characteristic decrease in slope observed above a certain temperature may indicate that deposition is no longer controlled by the chemical kinetics, but instead becomes limited by transport (Sect.3.2). However, alternative explanations cannot be ruled out (see discussion of Fig.5.4). The lower part of Fig.5.7 shows the deposition rate for Si deposited from SiH_4 - with H_2 as carrier gas [$p(SiH_4)$ = 1 mbar, p_{tot} = 1000 mbar] - according to standard CVD techniques [5.197]. The comparison of LCVD and CVD curves shows the remarkable differences between small- and large-area chemical reactions, as discussed in Sect.3.2.

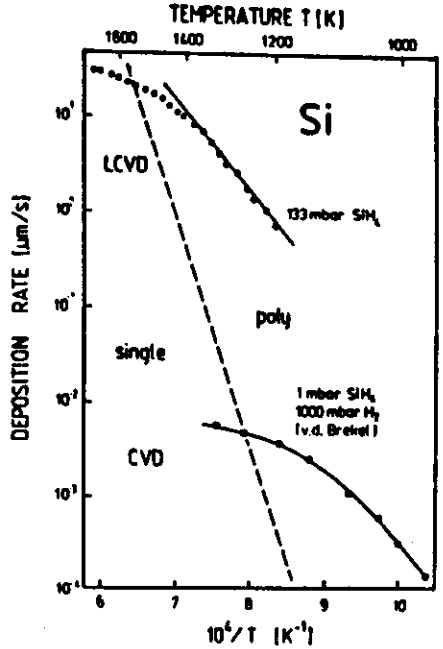

Fig.5.7. Arrhenius plot for deposition of Si from SiH_4 in LCVD and CVD. The broken line separates regions of single- and polycrystalline growth (after [5.104])

It proved possible to vary the diameter of Si rods between 20 µm and 380 µm for effective laser powers of 25 mW and 1.4 W, respectively, of the λ = 488 nm Ar^+ laser line. The lower limit was essentially determined by the mechanical stability of the apparatus, the upper limit by the available laser power. Due to the step-like increase in reflectivity at the melting point, the total absorbed laser power, $P(1-R_D)$, falls dramatically at this temperature.

Similar investigations were performed for the deposition of C from C_2H_2, C_2H_4, C_2H_6 and CH_4 [5.49,51-53]. The apparent chemical activation energy derived for the deposition from C_2H_2 was ΔE = 47.3 ± 0.6 kcal/mole (uncorrected value). This activation energy was independent of the gas pressure and temperature within the investigated ranges of 50 mbar ≤ $p(C_2H_2)$ ≤ 1000 mbar and 1900 K ≤ T ≤ 2450 K. The reaction order was found to be γ = 0.8. The corresponding values for C_2H_4 were ΔE = 58.3 ± 1.3 kcal/mole for 300 mbar ≤ $p(C_2H_4)$ ≤ 1000 mbar, 2000 K ≤ T ≤ 2250 K and γ = 0.8. For C_2H_6, ΔE = 78.9 ± 4 kcal/mole, 300 mbar ≤ $p(C_2H_6)$ ≤ 1000 mbar, 2200 K ≤ T ≤ 2650 K, γ = 2. For CH_4, ΔE = 119 ± 2 kcal/mole for 500 mbar ≤ $p(CH_4)$ ≤ 1000 mbar, 2850 K ≤ T ≤ 3100 K, γ = 1.25, and ΔE = 43.5 ± 1.4 kcal/mole for 500 mbar ≤ $p(CH_4)$ ≤ 1000 mbar, 2400 K ≤ T ≤ 2750 K, γ = 2.2.

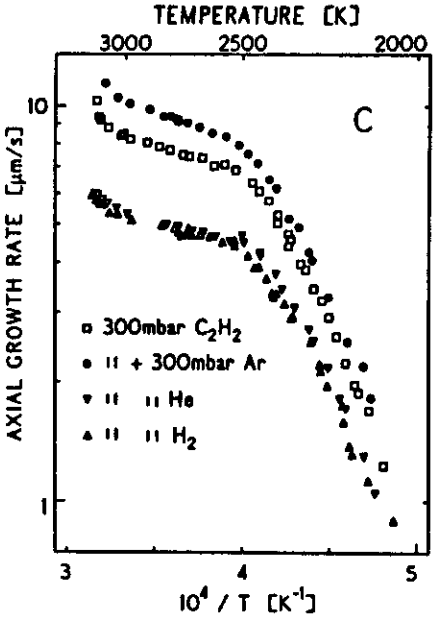

Fig.5.8. Arrhenius plot for the laser-induced deposition of carbon from pure C_2H_2 and from gas mixtures of C_2H_2 with H_2, He and Ar (after [5.53])

The influence of thermal diffusion on the deposition rate of C was investigated in detail for gas mixtures of C_2H_2 with H_2, He and Ar [5.53]. Figure 5.8 shows the results. Due to thermal diffusion, the lighter gases (He and H_2) accumulate near the hot tip of the rod, thus reducing the partial pressure of the reactant and thereby the deposition rate. Ar, on the other hand, has a higher molecular weight than C_2H_2. It is therefore depleted near the hot surface and, consequently, increases the partial pressure of C_2H_2, and thereby the deposition rate. The figure clearly shows that the selection of carrier gases used in LCVD has an important influence on the deposition rates achieved.

Rods of SiO_x and of stoichiometric SiO_2 were grown by using λ = 530.9 nm Kr^+ laser radiation and a mixture of N_2O and SiH_4 [5.170]. The growth of Ni rods from gaseous $Ni(CO)_4$ was investigated for laser powers ranging from about 10 mW up to about 200 mW [5.105]. The deposition rate did not change when Kr^+ laser wavelengths between λ = 476.2 nm and 647.1 nm were used (Table 4.1) - as one would expect for a thermally activated process (see Sect.2.1 and Chap.3). The limit of growth up to which controlled deposition was possible, was set by the occurrence of spontaneous breakdowns, probably due to an autocatalyzed reaction, within the gas phase above the surface of the tip of the rod.

Investigations of the temperature dependence of the deposition rate during the steady growth of rods are the most accurate method so far available for obtaining information on the reaction kinetics in pyrolytic LCVD. Furthermore, because of the extremely high deposition rates together with the possibility of in situ temperature measurements, this technique seems to be unique for rapid and accurate determination of apparent chemical activation energies that are also relevant to CVD and gas-phase epitaxial processes. The determination of such activation energies by the standard techniques is very time-consuming and problematic because a number of parameters, such as substrate temperature, gas velocity and gas mixture, must be held constant over long periods of time, generally several hours, and only small numbers of data points can be generated [5.51].

Other interesting possibilities, such as the growth of complicated three-dimensional structures by interference of laser beams, the production of materials with higher purity and the production of nonequilibrium materials or materials which form only under extreme conditions, can only be speculated upon.

The microstructure of rods has been mainly investigated by optical microscopy, scanning electron microscopy (SEM), X-ray diffraction and Raman scattering. The microstructure depends on the laser-induced temperature and the gas pressure. Rods have been grown in amorphous (SiO_x, SiO_2), polycrystalline (Ni, C, Si) and single-crystalline phases (Si). In this paragraph, we will only discuss further the growth of single-crystal Si rods [5.48,104,124]. Figure 5.9 shows a scanning electron micrograph of the tip of

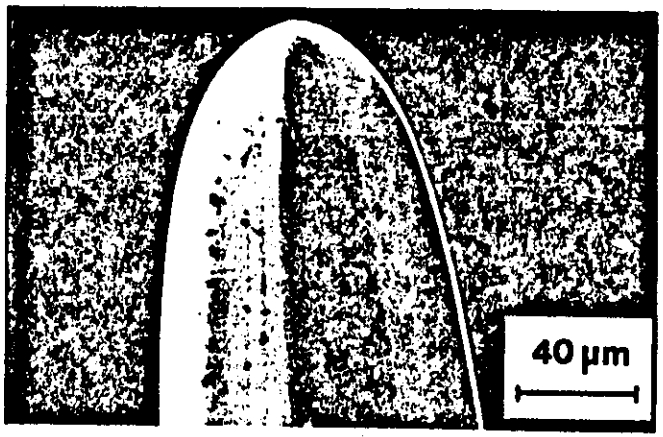

Fig.5.9. Scanning electron micrograph of the tip of a single-crystal Si rod grown at 1650 K with 530.9 nm Kr^+ laser radiation. $p(SiH_4)$ = 133 mbar (after [5.124])

such a rod that was grown from SiH_4 at 1650 K with 530.9 nm Kr^+ laser radiation. The orientation of the axis of such rods was found to be close to either <100> or <110> directions and independent of the substrate. Note that these are the fastest directions of growth in crystalline Si. For the silane pressure used, $p_{tot} \equiv p(SiH_4) = 133$ mbar, single-crystal growth was observed only above 1550 to 1650 K. In this connection it is interesting to recall the microstructure of Si films grown on single-crystal Si substrates by standard CVD techniques. Here, it has been found that the regime of polycrystalline growth is separated from the regime of single-crystal growth by a border line (dashed line in Fig.5.7) which is essentially determined by the ratio of the flux of Si atoms giving rise to the observed growth rate, and the value of the self-diffusion coefficient of Si needed to arrange the arriving atoms on proper lattice sites. Linear extrapolation of this border line to higher temperatures yields an intersection point with the LCVD curve at about 1520 K. This value is in remarkable agreement with the temperature limit we find for single-crystal growth of rods.

Pyrolytic Direct Writing

Pyrolytic direct writing was investigated by translating the substrate in one dimension perpendicular to the focused laser beam. In this case one obtains stripes. The most-detailed investigations have been performed for Ni and Si.

As in the case of spots and rods, the morphology of stripes strongly varies with laser power [5.48,50,104,105,198]. This is shown in Figs.5.10a-d for Si stripes deposited from SiH_4 on Si wafers. Here, 488 nm Ar^+ laser radiation was used. At laser powers corresponding to center temperatures below the melting point of Si, $T_m = 1683$ K, a convex cross section is observed, and the situation is very similar to that discussed below for direct writing of Ni stripes. When the laser power is further increased, a dip in the middle of the stripe (Fig.5.10c) occurs for center temperatures $T > T_m$. This dip further increases with increasing laser power (Fig.5.10d). The dip can be explained by the change in surface tension with temperature, which pulls the liquid away from the valleys. At such laser powers, polysilanes, probably formed in a homogeneous reaction above the surface of the deposit, condense in the region of deposition. Melting of the surface of the stripe is accompanied by the occurrence of a ripple structure with grating vector k parallel to the incident electric field vector F. The formation of ripples and of periodic superstructures that occur under certain experimental conditions will be discussed in Sect.5.2.5.

The influence of melting and changes in the morphology of stripes complicate the understanding of the deposition process. The following

Fig.5.10a-d. Stripes of Si grown on Si wafers with increasing laser power (left to right). $p(SiH_4) = 40$ mbar, $v_s = 10$ μm/s, $\lambda = 488$ nm (after [5.198])

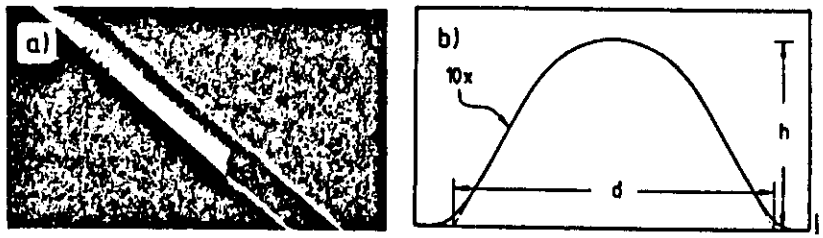

Fig.5.11a,b. (a) Ni stripe grown on glass covered with 1000 Å a-Si. P = 6 mW, $2w_0 = 2.5$ μm, $\lambda = 530.9$ nm, $p(Ni(CO)_4) = 400$ mbar, scanning velocity $v_s = 84$ μm/s. (b) Typical thickness profile of a Ni stripe. The vertical scale is expanded ten times (after [5.105])

analysis of direct writing will therefore be confined to low laser powers where no appreciable changes in the shape of the cross section occur and where, therefore, an unequivocal definition of a stripe width and height is possible. The main experimental results will be outlined in detail for the example of Ni stripes that have been deposited on substrates of different absorbance and thermal conductivity [5.105,106].

A typical Ni stripe together with its interferometrically measured thickness profile, is shown in Fig.5.11. We shall henceforth define the width of the stripes by d, and the thickness by h.

Figure 5.12 shows the width and thickness of Ni stripes as a function of laser power for three different substrate materials. In all cases, the cross section of the stripes is similar to that shown in Fig.5.11. The height, measured in the middle of the stripe, is typically $h \leq (0.05\text{-}0.1)d$. The negligible influence of the laser wavelength (Fig.5.12b) supports the idea that the decomposition mechanism is mainly thermal. Note that the results for the 1000 Å a-Si/glass substrate and the uncovered glass substrate are approximately equal (Figs.5.12a,b). Both substrates have about the same thermal conductivity. However, their absorbances for 530.9 nm Kr^+ laser radiation differ by several orders of magnitude. Therefore, these results strongly suggest that in steady growth of stripes the total laser power

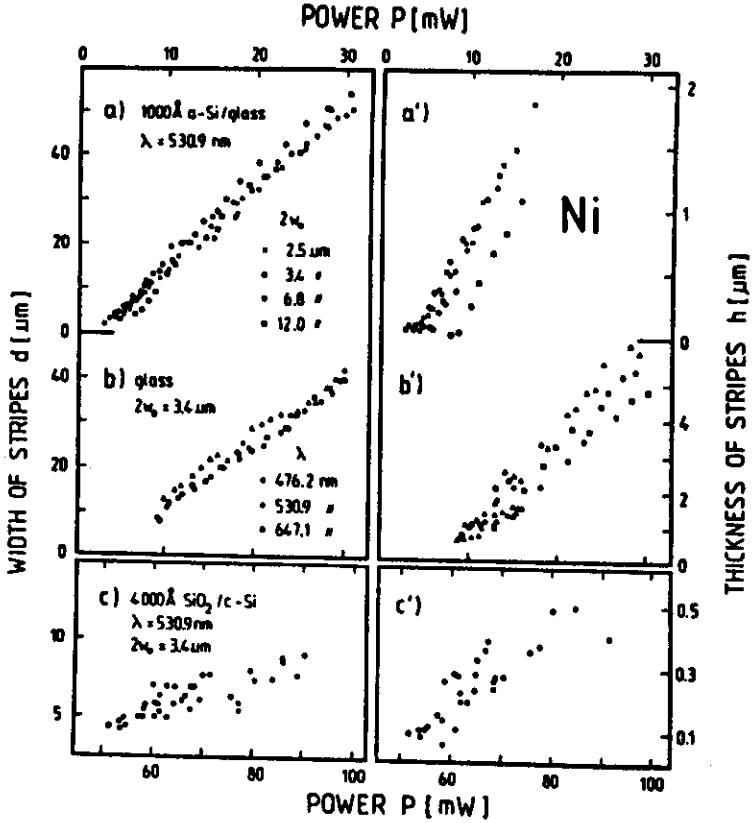

Fig.5.12. Dependence of width and thickness of Ni stripes on total laser power for different focus diameters, wavelengths and substrates. In all cases, the total pressure was $p_{tot} \equiv p(Ni(CO)_4)$ = 400 mbar, and the scanning velocity = 84 µm/s (after [5.105])

absorbed is determined by the absorbance of the already deposited material and is given by $P(1-R_D)$. Apparently, steady growth of stripes occurs as drawn schematically in Fig.5.13. During the dwell time of the laser beam, lateral growth occurs. In steady growth, the lateral growth velocity in the scanning direction, v, must be equal to the scanning velocity of the laser beam, v_s, i.e. $v = v_s$ (this condition does not hold in explosive deposition, which is briefly discussed in Sect.5.2.5). Steady growth of stripes tails off when the scanning velocity of the laser beam exceeds the maximum lateral growth velocity, i.e. if $v_s > v_{max}$. In fact, the maximum lateral growth rates found for the deposition of Ni spots on 1000 A a-Si/glass agree, to within a factor

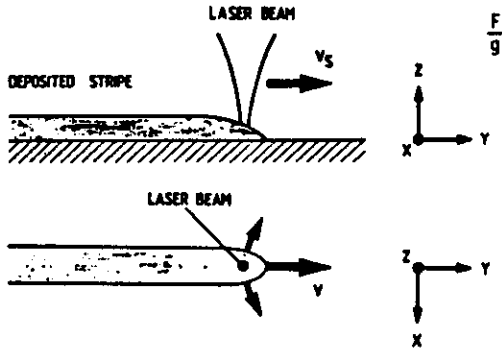

Fig.5.13. Schematic for steady growth of stripes (after [5.48])

of about two, with the maximum scanning velocities obtained for the same system and the same set of parameters (see below).

Comparison with Model Calculations

We now compare the results of Fig.5.12 with model calculations presented in Sect.2.1.2. Assume we produce the same center temperature T_c for all three substrate materials considered. From the full curves in Figs.2.12a-c it then becomes clear that in cases b and c the temperature falls off much faster away from the center than in case a (note that the temperature distributions shown in Fig.2.12 have been calculated for circular cylinders; however, as outlined in Sect.2.1.2, these temperature profiles are very similar to those obtained within cross sections of stripes). Because growth occurs only down to a threshold temperature T_t (see also Sect.5.1), the stripe in Fig.2.12b or c grows to a final width much smaller than that in Fig.2.12a. This explains the different width of stripes in Figs.5.12a-c. For thermally insulating substrates, the width of metallic stripes, here the Ni stripes (Figs.5.12a,b), grow to a final width that is much larger than the laser focus, i.e. $d >> 2w_0$ (except for the lowest laser powers). On the other hand, if the thermal conductivities of the deposit and the substrate are equal, as in the case of Fig.5.12c, the width of stripes remains of the order of the diameter of the laser focus. The results of the model calculations presented in Fig.2.12a also explain another feature in Fig.5.12a. For medium and higher laser powers (for these powers under consideration $T_c < T_m(Ni)$, and no changes in the shape of the cross section have been observed) the widths of stripes are independent of the diameter of the laser focus. Let us consider, for example, the effect on the temperature distribution (dash-dotted curves in Fig.2.12) of doubling the laser focus diameter at constant laser power. In the case of Fig.2.12a, the temperature rise $\Delta T(d/2)$ remains approximately the

same. As a consequence, the width of the stripe is expected to remain unaffected, in agreement with the results of Fig.5.12a. However, in Figs.2.12b,c, deposition becomes impossible when the laser focus is doubled, because even the center temperature T_c decreases below the threshold temperature for deposition. If in the case of Fig.2.12a T_c approaches T_t, deposition will continue to lower laser powers as the diameter of the laser focus becomes smaller. This is reflected also in the experimental results of Fig.5.12a. In other words, the smallest widths of structures that can be achieved, depend on $2w_0$. The fact that stripes can be produced that are narrower than the diffraction limit of the optical system (see Fig.5.12a) originates from the threshold for deposition, discussed above (see also Sects.3.5 and 5.1).

The dependence of the width and thickness of stripes on the scanning velocity is shown in Fig.5.14. For the parameters used in these experiments, the breakoff occurs at about 130 µm/s. When increasing P, under otherwise identical experimental conditions, the scanning velocity can also be increased. The dashed curve in Fig.5.14 was calculated by using $v = v_0 \exp(-\Delta E/RT)$ and $T = T_0 + \Delta T$, together with (2.19) and the steady state

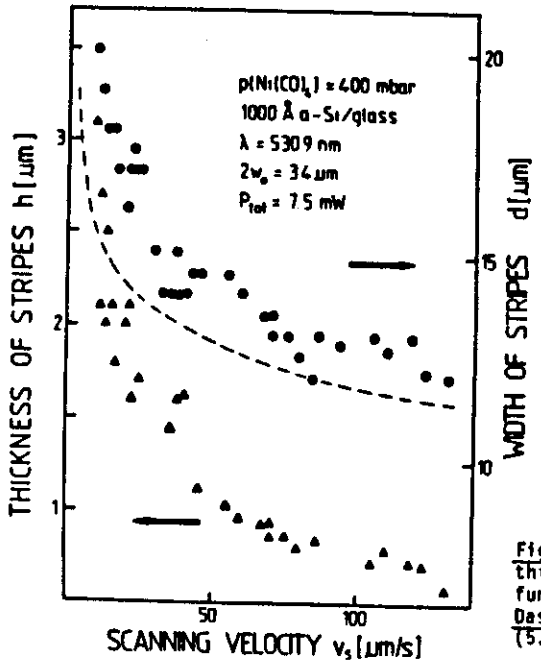

Fig.5.14. Width (•) and thickness (▲) of stripes as a function of scanning velocity. Dashed line is calculated from (5.4) (after [5.105])

condition $v = v_s$, giving

$$d = \frac{P\,(1 - R_0)}{2\kappa_S\,[(\Delta E/R)\,[\ln(v_0/v_s)] - T_0]]} \quad . \tag{5.4}$$

Here, $v_0 = Ak$ has been taken from the Arrhenius plot in Fig.5.4. In other words, the dashed curve in Fig.5.14 contains no additional parameter. Comparison with the experimental data shows that this crude approximation describes the absolute width as well as its dependence on the scanning velocity reasonably well. The explanation of the remaining deviations requires a self-consistent treatment, the consideration of the velocity dependence of the exact position of the laser focus with respect to the tip of the growing stripe and of the heat transport along the stripe (Sect.2.1.2). A more sophisticated model, which takes these effects into account, makes it possible to describe the experimental data quantitatively [5.190].

The foregoing results are by no means specific to direct writing of Ni stripes but are characteristic of pyrolytic LCVD of flat structures in general. Similar results corresponding to the case $\kappa_D >> \kappa_S$, were obtained for the deposition of Al and Si on 1000 Å a-Si/glass [5.125,198], for C on Al_2O_3 [5.49], and with some restrictions, for Cu on Si [5.74]. In addition to the example of Ni on 4000 Å SiO_2/Si (Fig.5.12c), the case $\kappa_D = \kappa_S >> \kappa_L$ (Fig.2.12b) applies also to Si on 4000 Å SiO_2/Si [5.128,129]. The case $\kappa_D = \kappa_S = \kappa_L$ has been verified for Ni on Si [5.106,107] and for Si on Si [5.126,128,129]. In these latter cases the widths of stripes are typically $d \lesssim 2w_0$. This is what Figs.2.12b,c would lead us to expect.

From the above discussion it is clear that many features in direct writing can be qualitatively or semiquantitatively understood from calculated temperature profiles as presented in Sect.2.1.2. The foregoing results also show that in direct writing the range of parameters and therefore the lateral and axial growth rates and the related maximal scanning velocities strongly depend on both the physical properties of the deposited material *and* of the substrate. While the possible range of variation in the width of stripes is very large for $\kappa_D >> \kappa_S$, it is very small for $\kappa_D = \kappa_S$. The upper limit is essentially based on the maximum center temperature at which controlled deposition is possible, i.e. no dramatic changes occur in the geometry of the deposit, there is no damaging of the substrate and no triggering of a homogeneous gas-phase reaction above the surface of the deposit. Furthermore, small changes in $2w_0$ or in the positioning of the substrate or in the laser power (due to systematic uncertainties or due to mechanical or electrical

instabilities) will have a much stronger influence for systems where $\kappa_D \approx \kappa_S$ than for those where $\kappa_D >> \kappa_S$. This may also explain the larger scatter in the data of Fig.5.12c compared to those in Figs.5.12a,b.

Pyrolytic direct writing of electrically highly conducting B dosed Si stripes with linewidths as small as 1 μm was first reported by EHRLICH et al. [5.129]. The dopant gases were BCl_3 and $B(CH_3)_3$. Similar experiments using $Al_2(CH_3)_6$ as dopant were unsatisfactory. The reason is probably the large difference in pyrolytic decomposition rates of $Al_2(CH_3)_6$ and SiH_4. With $B(CH_3)_3$ the best films had resistivities of about $1.5 \cdot 10^{-3}$ Ωcm.

Deposition with IR Lasers

Pyrolytic deposition of structures in the form of spots, rods, and stripes by means of IR light was mainly performed with 10.6 μm cw or pulsed CO_2 laser radiation (Table 5.1). First experiments have been reported for C [5.55] and for Si [5.136]. Detailed investigations on Si deposition have been performed by HANABUSA et al. [5.149,150]. Because the diffraction-limited diameter of the laser focus is proportional to the wavelength of the light λ, see (4.2), the smallest lateral dimensions of deposits are much larger, typically by a factor of 20-50, than those achieved with visible or ultraviolet light (Sect.3.5). Consequently, mass transport will often be determined by one-dimensional diffusion. This significantly reduces the maximum (thickness) deposition rates with respect to those achieved with visible or ultraviolet light. The formation of thin extended films by means of IR laser radiation will be outlined in Sect.5.3.

b) Photolytic LCVD

Production of microstructures by photolytic LCVD based on the excitation of dissociative electronic transitions of parent molecules (Sect.2.2.1) has been studied mainly for metals. The precursors most commonly used are metal-alkyls, metal-carbonyls and metal-fluorides (Table 5.1). The microscopic mechanisms for decomposition are based on single-photon or multiphoton processes.

Single-photon decomposition has been most thoroughly studied for $Cd(CH_3)_2$, and $Al_2(CH_3)_6$ [5.8]. These compounds were preferred because they are readily available, have a relatively high vapor pressure and, very importantly, they show a dissociative continuum in the near to medium UV that can be easily reached by frequency doubling of cw Ar^+ or Kr^+ laser lines, by excimer lasers, or by harmonic lines of Nd:YAG lasers. Furthermore, for $Cd(CH_3)_2$ some of the reaction channels were already known for the homogeneous

photodecomposition process (Sect.2.2.1). Therefore, $Cd(CH_3)_2$ can be considered as a model substance for investigating photolytic deposition based on single-photon decomposition processes. Dissociation of the molecule proceeds according to (2.20), and, of course, takes place within the total volume of the laser beam. This reaction, or ones similar to it, may therefore be used to produce extended thin films at low substrate temperatures by using either perpendicular or parallel laser irradiation (see Sect.5.3 and Figs.4.2b,3). Nevertheless, it has been shown that photolytic processing also allows single-step production of microstructures. The spatial confinement of the deposition process is probably closely related to physisorbed layers of the parent molecules and to the nucleation process itself. This has already been outlined in Sects.3.1, 3.5 and 5.1. In cases where physisorption is very weak, severe problems with the confinement of the reaction may occur [5.72]. On the other hand, it is possible to achieve good localization and feature contrast even in cases such as these by taking a number of experimental precautions - as already discussed in Sect.3.5.

Figure 5.15 shows the (thickness) deposition rate for Cd spots as a function of the intensity of the 257.2 nm frequency-doubled Ar^+ laser line. The linear increase in deposition rate with laser power is expected for single-photon dissociation (Sects.2.2.1 and 3.2). At low laser fluences the threshold for surface nucleation prevents deposition. At much higher laser fluences than those shown in Fig.5.15, the deposition rate saturates due to mass transport limitations. This effect is more pronounced when a buffer gas

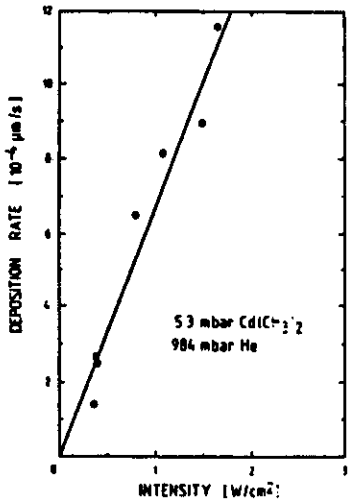

Fig.5.15. Deposition rate for Cd spots versus 257 nm second harmonic Ar^+ laser light intensity. $p(Cd(CH_3)_2)$ = 5.3 mbar. He was used as a buffer (after [5.8])

is used. Mass transport could be increased by forced gas convection or a flow. Deposition rates for Cd of up to 0.1 μm/s have been measured at UV intensities of about 10^4 W/cm^2.

The absolute value of the deposition rate depends on the absorption cross section σ_a of the molecule at the laser wavelength, on the partial gas pressure of the reactant and, when a buffer gas is used, on the total gas pressure. For example, at 257.2 nm the absorption cross section for $Al_2(CH_3)_6$ is smaller than that for $Cd(CH_3)_2$ by more than a factor of 10^3, resulting in a corresponding decrease in deposition rate at otherwise constant conditions (Table 2.1). This example shows one of the main limitations for photolytic LCVD based on single-photon processes. Deposition rates that are attractive for applications of the technique can only be reached when the laser wavelength matches a dissociative transition of the molecule. For many molecules which would be suitable for the deposition of metals, semiconductors, or insulators, these transitions are located in the medium to far ultraviolet, where, at present, only a small number of comparatively intense laser light sources are available (Table 4.1). A more fundamental, and therefore even more severe, limitation is the tendency for homogeneous cluster formation at higher laser irradiances and/or partial pressures of reactants. Clusters may condense everywhere on the substrate surface, the entrance windows, etc. Controlled deposition then becomes impossible. For these reasons, the deposition rates in photolytic LCVD will be always much lower than those achieved in pyrolytic LCVD.

Controlled growth in UV laser photodeposition of metals was observed for laser irradiances of, typically, 1 to 10^4 W/cm^2, and for gas pressures extending from 0.1 to 100 mbar. Typical deposition rates achieved were 10^{-3} to some 0.1 μm/s (Table 5.1). These deposition rates are a factor of 10^4-10^2 smaller than those obtained in pyrolytic LCVD. The main advantages of photolytic LCVD are the lower local processing temperatures and the smaller influence of the physical properties of the substrate. On the other hand, without uniform substrate heating, the microstructure, purity, and electrical properties of photodeposited films are, in many cases, unsatisfactory (Sect.5.4). The lateral resolution achieved in photolytic deposition of stripes was of the order of some 0.1 μm (Sect.3.5).

Coherent multiphoton decomposition processes based on dissociative electronic excitations are only of limited value for controlled deposition of well-defined micrometer-sized structures. The main reasons have already been outlined in Sect.4.2. In fact, detailed investigations into the deposition of Cr from $Cr(CO)_6$ by MAYER et al. [5.72] have illuminated many of these

problems. Additionally, the Cr films had poor adherence and contained a large amount of C. The adherence of films could probably be improved by heating the substrate either during the deposition process or prior to removal from the reaction chamber.

There is as yet *no* clear example of photolytic LCVD based on selective multiphoton *vibrational* excitations with IR laser radiation. The only detailed investigations have concentrated on the deposition of Si from SiH_4 by means of pulsed CO_2 laser radiation [5.137,149,150,153]. However, the decomposition mechanisms seem to be dominated by gas-phase heating and not by multiphoton processes (see also Chap.2 and Sect.5.3).

c) Combined Pyrolytic-Photolytic (Hybrid) LCVD

Pyrolytic and photolytic LCVD have both their characteristic advantages and disadvantages: The deposition rates in pyrolytic LCVD exceed those in photolytic LCVD by several orders of magnitude. Consequently, pyrolytic LCVD allows much higher scanning velocities in direct writing and also the production of three-dimensional structures. The microstructure and the electrical properties of pyrolytically deposited materials are in general superior to those deposited by photolysis (Sect.5.4). Laser pyrolysis is much more universal in the sense that the reaction rate depends only slightly on the exact wavelength of the laser light. For this reason, a great variety of materials can be deposited. The basic advantages of photolytic LCVD are the lower local processing temperatures and the lower sensitivity to the physical properties of the substrate. Therefore, direct writing of patterns over different materials with significantly changing thermal properties can be performed more uniformly.

A possibility that makes the best of the advantages and disadvantages of both pyrolytic and photolytic LCVD is a twin-beam or single-beam combined pyrolytic-photolytic reaction. Initial investigations of this type have been performed for the deposition of Ni from $Ni(CO)_4$ [5.50,104-106]. Here, it was clearly demonstrated that for (visible) laser radiation that is absorbed neither within gaseous $Ni(CO)_4$ nor by the substrate, the latent times for nucleation (Sect.5.1) are significantly reduced when the UV plasma radiation of the laser [this is absorbed by $Ni(CO)_4$] is not blocked but focused onto the substrate together with the laser light. Similar results have been obtained when using 356 nm Kr^+ laser radiation only. This wavelength is slightly absorbed by $Ni(CO)_4$, but not by quartz substrates. In both cases, when nucleation was started, deposition proceeded mainly pyrolytically and

was then essentially equal for the different Kr^+ laser lines between 356 and 647 nm (Table 4.1), and independent of the presence of the plasma radiation. This can be understood from the strong absorption of the deposited Ni, which is approximately constant within this range of wavelengths. Hybrid deposition was recently investigated in greater detail for Mo, W and Pt by GILGEN et al. [5.103]. Here, the UV multiline Ar^+ laser output between 351 and 364 nm was used together with $Mo(CO)_6$, $W(CO)_6$ and Pt(HFAcAc) as parent molecules. These experiments have confirmed that metal films of good morphology and electrical properties (Sect.5.4) can be deposited without uniform substrate heating or curing only by laser pyrolysis. Nevertheless, photolytic mechanisms that also contribute at these laser wavelengths allow direct patterning of transparent substrates such as glass or sapphire, without a measurable initial delay or latent time. Clearly, photolysis is relevant here only for initiation of the deposition process, because afterwards absorption is determined by the already deposited material (see above and Sect.2.1.2).

5.2.3 Liquid-Phase Deposition, Electroplating

Laser-induced deposition from the liquid phase has been demonstrated mainly for metals. KARLICEK et al. [5.42] have deposited Pt, Au, and Ni from aqueous H_2PtCl_6, $HAuCl_4$ and $NiSO_4$ solutions, respectively. Also, Pt and Au were deposited from the corresponding methanol solutions. The substrate materials used were mainly p-type, n-type and undoped (110) and (111) InP and, for Pt deposition, also n-type GaAs. Pulsed dye laser radiation ranging from 580 nm to 720 nm was employed (within this wavelength range, the metal salt solutions are transparent). The light intensities were sufficient to initiate thermal decomposition of the InP surface, but below the threshold at which gross surface damage occurs. Smooth platinum films up to a thickness of 0.5 μm were deposited. The platinum deposits were examined by AES sputter profiling and by electron microprobe analysis. No solution contaminants such as oxygen or chlorine were found. Deposits of Pt and Au on undoped InP exhibited ohmic behavior. In the initial phase of metal deposition, a photothermal chemical reaction between the InP surface and the metal salt seems to be involved. In the interfacial layer, PtP_2, NiP or similar compounds may be formed. Further decomposition seems to occur via pyrolysis at the metal-liquid interface. Attempts to deposit Pt on (111) Si were unsuccessful. An understanding of the deposition process clearly requires further investigations.

Electrochemical laser-enhanced plating has been studied in great detail by VON GUTFELD [5.32,33]. Some of the experimental details have already been outlined in Sect.4.1. The most extensively studied materials were Au, Cu and Ni, which were deposited on a variety of substrates. The substrates were glass and c-Al_2O_3, both covered with 0.1 μm thick films of either Au, Cu, Ni, Mo or W, and, additionally, metals such as Ni and Ni-plated Be-Cu (Table 5.1). The plating mechanism was investigated by illuminating the metallized glass surface from two directions: either from the front through the solution, or from the back through the optically transparent glass. In the latter illumination geometry, no photons reach the electrolyte, because the light is absorbed within 30 to 200 Å of the 0.1 μm thick metal film. Interestingly, the deposition rate was found to be equal for both geometries of illumination. Hence, nonthermal photochemical processes at the liquid-solid interface cannot play an important role. On the other hand, this result is expected for a thermally activated reaction, because the laser-induced temperature distribution within the metal surface is approximately the same for both illumination geometries. Further support for the thermal character of the deposition process was obtained from the comparison of plating results for premetallized c-Al_2O_3 (κ_0 = 20 W/mK) and glass substrates. Under otherwise identical experimental conditions, the depositon rates on c-Al_2O_3 substrates were found to be a factor of 10 smaller than on glass. This can be directly explained by the decrease in center temperature (at constant laser irradiance) with increasing thermal conductivity of the substrate (Sect.2.1.1). The temperature change influences the charge and mass transfer rates within the electrochemical system (with and without an external EMF). The mechanism has already been described in Sect.3.3.

Detailed investigations into electrochemical Au plating have revealed that dense, small-grained, crack-free and uniform deposits of good adhesion are formed at elevated ambient temperatures and at a high density of gold concentration in the electrolyte. The operating potential was of similar importance; this should not exceed the mass-transport limit. Near this limit, Au of good morphology was deposited over areas 500 μm in diameter with rates up to 1 μm/s. Direct writing of Cu lines on premetallized glass substrates was possible with minimal widths of about 2 μm.

A new technique that improves the mass-transport limitation and thereby increases the deposition rate is laser-enhanced jet-plating (Sect.4.1). This technique allows high-quality, rapid, localized plating. The electrochemical and hydrodynamic parameters determining the mechanical and metallurgical properties of the deposits have been investigated, in particular for the model substance Au [5.34,36,222]. For Au, plating rates of up to 12 μm/s have been achieved. The surface smoothness of the Au films increases with

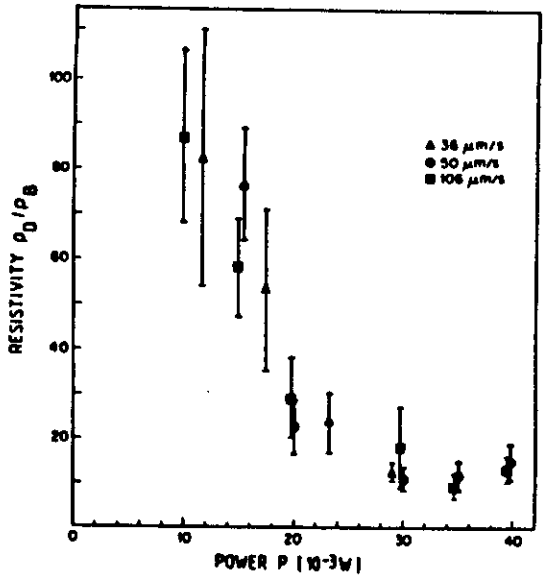

Fig.5.17. Resistivity of Au lines produced as in Fig.5.16 normalized to the bulk value for Au (2.44 Ω cm) (after [5.47])

speed and/or the viscosity of the organosilicate solution. Material not exposed to the laser beam was rinsed off with methanol. The laser-induced reaction probably consists of an initial elimination of the organic liquid and a subsequent release of OH groups. The quality of the SiO_2 films was at least as good as that obtained in thermally cured spun-on glass. The breakdown strength was about $1.6 \cdot 10^6$ V/cm.

5.2.5 Periodic Structures

In pyrolytic direct writing, various different types of periodic structures are observed in a large number of systems for certain ranges of processing parameters.

One type of periodic surface structure, the so-called ripples, which have been observed in laser-deposited thin films, arises from interference effects between the incident and scattered laser fields. Figure 5.18 shows examples for the case of Si deposited from SiH_4 on Si wafer substrates by means of 488 nm Ar^+ laser radiation [5.48,127,128]. These ripples show the characteristic features that have long been observed on many semiinfinite substrates, mainly after pulsed laser irradiation in a *nonreactive* atmosphere [5.202-204]. The

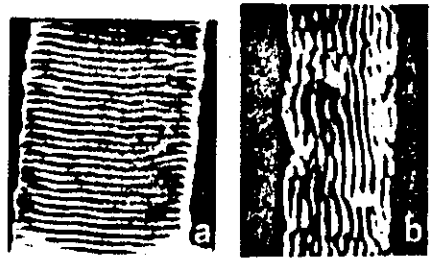

Fig.5.18a,b. Rippling on Si stripes deposited from SiH_4 on Si wafers by means of 488 nm Ar^+ laser radiation. The electric vector of the radiation was parallel (a) and perpendicular (b) to the direction of scanning (after [5.48,128])

ripples are characterized by some experimentally well-proved features: at normal incidence, the ripple spacing is approximately equal to the wavelength of the laser light, and the grating vector is polarized parallel to the incident electric field vector F (see Fig.5.18). These ripples will not be discussed any further in this section.

Another type of periodic structure having periods much longer than the ripples, has been observed in various different systems [5.45-48,83,125,127, 128,201,223]. While the physical microscopic mechanisms are quite different for the various systems so far investigated, these structures seem to be a general phenomenon in laser-induced pyrolytic processing. Some examples will be discussed in the following.

Figures 5.19-20 show the new types of periodic structures for the case of direct writing based on pyrolytic LCVD, and for different systems and processing parameters. As far as is understood at present, these periodic structures are *not* related to the ripples mentioned above. No simple relation exists between the spatial period and the wavelength and the polarization of the laser light. The spacing of the periodic structures shown in the figures, i.e. the distance between the minima in the thickness or the width of the stripes, depends on the laser power, the scanning velocity, and the pressure of the reactant gas. These dependencies have been studied in detail for the deposition of Si on glass substrates covered with a thin layer of a-Si.

Figure 5.21 shows the spacing as a function of the incident laser power for a scanning velocity of v_s = 50 µm/s and a SiH_4 pressure of 200 mbar. While uniform stripes are observed for laser powers around 20 to 30 mW (case a in Fig.5.19, indicated by the crosses in Fig.5.21) periodic structures occur above and below this range of laser powers (the structure formation at lower laser powers seems to be closely related to the a-Si/glass substrate and will be discussed in [5.224]). It becomes evident from Fig.5.21, however, that these limits in laser power are not clear-cut, as overlapping regions exist where stripes are either uniform or show pronounced periodic

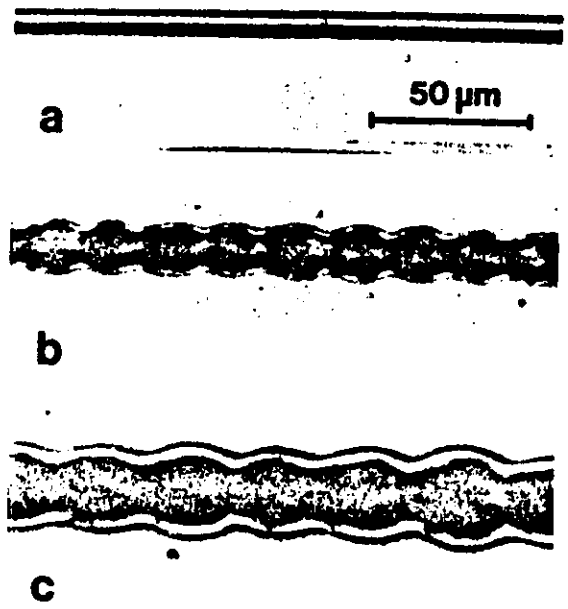

Fig.5.19a,b,c. Stripes of poly-Si deposited from SiH_4 by means of 647 nm Kr^+ laser radiation. The substrate is glass covered with 1200 Å a-Si. $2w_0$ = 7 µm, v_s = 50 µm/s, $p(SiH_4)$ = 200 mbar. (a) P = 34 mW; (b) P = 81 mW; (c) P = 130 mW (after [5.125])

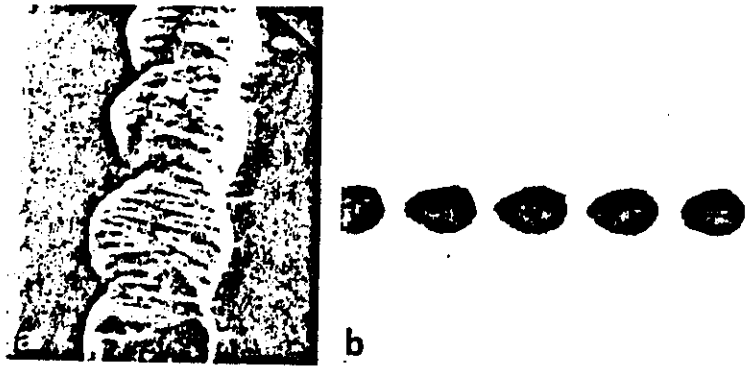

Fig.5.20a,b. Examples of periodic structures. (a) Si deposited on Si wafers (after [5.48,128]). (b) Ni deposited on 1000 Å a-Si/glass substrates (after [5.201])

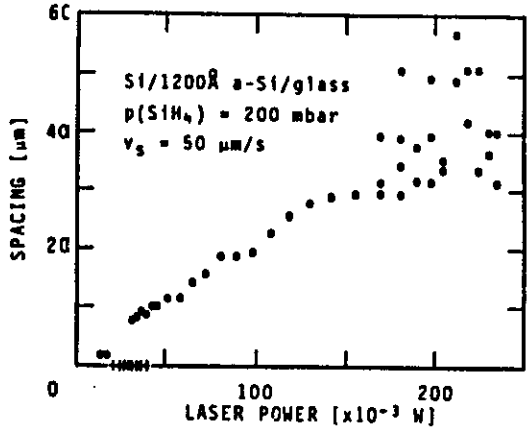

Fig.5 21. Spacing of the periodic structures as a function of the laser power + symbols indicate region of uniform deposition of stripes (after [5.125])

structures. For laser powers 40 mW ≤ P ≤ 150 mW, the spacing is well-defined and increases approximately linearly with laser power. For laser powers in excess of about 150 mW another instability is observed. In this regime a set of various different spacings, including the appearance of uniform structureless stripes, is observed for any given set of parameters. Figures 5.22a b show the minimum (open symbols) and maximum (full symbols) widths of stripes as a function of the laser power for two different ratios $p(SiH_4)/v_s$. It can be seen that the amplitudes of the oscillations increase with increasing laser powers and ratios $p(SiH_4)/v_s$.

The origin of the structure formation remains speculative. First of all, the uniformity, fine reproducibility, and the measured dependencies on experimental parameters lead us to believe that the structure formation is not related to remaining fluctuations in experimental parameters - even in the light of the fact that, for example, minor changes in laser power (which was stabilized to better than 0.2%) and thereby in local temperature can significantly affect the deposition rate within the kinetically controlled region (see, for example, Fig.5.7). Furthermore, one can exclude any explanations that are based on the latent heat released by the SiH_4 decomposition and the concomitant formation of crystalline Si. For typical volumes of deposited material (laser power of 100 mW, SiH_4 pressure of 300 mbar, chemical heat release of 5 kcal/mole [5.205]), one obtains a rate of heat release of the order of 10^{-6} W. This is negligible compared to the power absorbed from the laser beam, which amounts to about 50 mW (for a

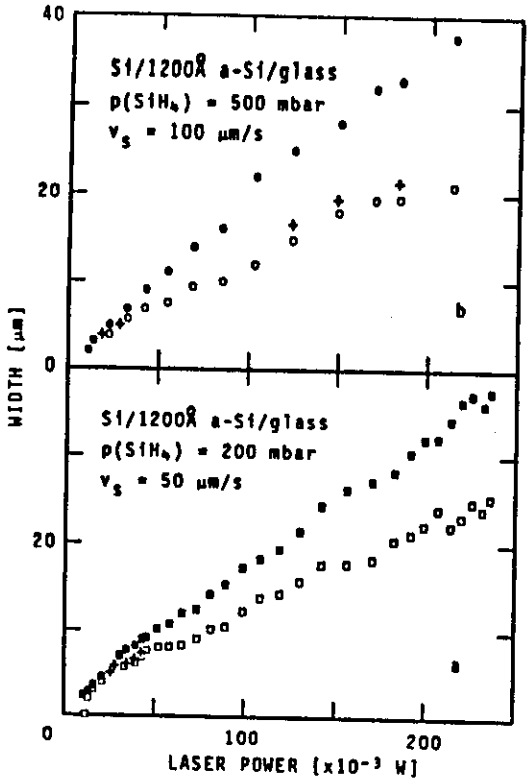

Fig.5.22. Minimum (empty symbols) and maximum (full symbols) widths of stripes as a function of laser power. (a) v_S = 50 µm/s, $p(SiH_4)$ = 200 mbar. (b) v_S = 100 µm/s, $p(SiH_4)$ = 500 mbar. Crosses indicate uniform stripes (after [5.125])

typical reflectivity of 40% - 50%, and a penetration depth below 1 µm for the relevant wavelengths and temperatures), unless one assumes that virtually all deposition takes place during single bursts that together last less than 10^{-4} of the dwell time of the laser beam. The rate of deposition of Si at a given site per unit of SiH_4 pressure is determined by the temperature at that site. In the case of a temperature-independent thermal conductivity κ and reflectivity R, and a high absorption coefficient α, this temperature distribution has been shown in Fig.2.14 for similar, but not identical geometries. From this figure, a qualitative explanation of the periodic structure for continuous stripes (rather than for separated single islands) is possible: Since the thermal conductivity of Si is at least a factor of 30 higher than that of the glass substrate, the heat flow via the stripe will

soon dominate over the direct flow from the zone of deposition into the substrate. Thus, the surface temperature, and thereby also the temperature at the edge of the stripe (see dashed arrow on left hand side of Fig.2.14), will fall rather rapidly as the cross section of the stripe increases. The decrease in temperature leads to a reduction in the deposition rate, and hence to a decrease in the cross section of the stripe. The decrease in cross section, however, leads to an increase in local temperature (see dashed arrow on right hand side of Fig.2.14) etc. Due to the finite extent of the zone of deposition, this feedback mechanism is not instantaneous. The period of oscillations should decrease with increasing strength of the feedback.

The observation of even isolated islands of deposits could be tentatively understood in the following way: the laser light absorbed within the a-Si layer induces a temperature distribution with a center temperature barely exceeding the threshold for deposition. This results in the growth of a spot and a concomitant decrease in temperature. Once deposition has ceased it cannot start again until the overlap of the laser focus with the spot-like heat sink has decreased sufficiently for the threshold temperature for deposition to be attained once more.

The mechanisms outlined above can also explain the structures observed in Ni deposits on glass (Fig.5.20b), but not those seen in Si deposits on Si wafers (Fig.5.20a). In the latter case the thermal conductivity of the deposit is somewhat lower than that of the substrate, due to the higher temperature of the deposit [see (2.11)]. Thus, the surface temperature may be expected to increase with increasing thickness of the stripes. This continues until the surface reaches the melting point. At that point the reflectivity suddenly increases, leading to a lowering of the rate of energy absorption from the laser beam. As a consequence, the temperature and thereby the reflectivity will decrease. This results in an increase in absorbed laser power until the surface melts again.

Another type of periodic structure was recently observed by JACKMAN et al. [5.83] during Ar^+ laser-induced deposition of Fe on SiO_2-glass substrates. Here, the structure formation seems to be related to an oscillation between the endothermic decomposition of $Fe(CO)_5$ and an exothermic solid state reaction between the metal deposit and the SiO_2 substrate. The periodic segregation into Fe and Fe_2SiO_4 phases along the stripe was confirmed by scanning Auger spectroscopy. The spacings were, typically, around 50 µm.

Periodic structures with spatial periods larger than the laser wavelength were also reported to occur in experiments on laser-induced chemical decomposition of metallopolymer films. FISANICK et al. [5.45-47,115]

interpret the periodic structures as a chemical analog of explosive crystallization [5.206,207], i.e. as a process driven by the release of chemical latent heat. On the other hand, the heat flow via the Au or Pd films produced by the reactions studied in [5.45-47,115] appears to be at least comparable to the heat flow directly into the substrate. Thus, the mechanism proposed above may well also play a role in these systems.

Periodic structures have also been observed during rapid-scan synthesis of Ge_xSe_{1-x} from sandwich films of Ge and Se [5.223]. The formation of these structures has been explained in terms of an explosive reaction based on the release of latent heat during synthesis.

The preceding examples have shown that in pyrolytic direct writing of microstructures the local temperature, and thereby the reaction rate, may oscillate, even under stationary conditions, when the process parameters, such as the laser power, scanning velocity, physical properties of the substrate etc., are held constant. Such oscillations may originate from the nonlinear heat transport, the explosive release of heat in a strongly exothermic reaction, or from nonlinearities in the reflection and absorption of the material etc. The oscillations may decrease the ultimate resolution of structures obtainable in direct writing below the value expected for a stationary temperature distribution on the basis of the exponential dependence of the reaction rate on temperature (Sect.3.5). On the other hand, the periodic structures can be suppressed for certain ranges of process parameters, which must be determined experimentally for every system of interest. Clearly, further investigations of both an experimental and a theoretical nature are necessary in order to illuminate the various mechanisms present in different systems, and their importance in direct writing of microstructures.

5.3 Extended Thin Films

Extended thin films of metals, semiconductors and insulators have been deposited with laser beams at both perpendicular and parallel incidence. The different irradiation geometries, focusing possibilities and most commonly used lasers have been described in Sects.4.1 and 4.2.

For perpendicular incidence the situation is very similar to that discussed in Sect.5.2 for pyrolytic and photolytic deposition of microstructures. The main difference is that gas- or liquid-phase transport limitations become important at lower (thickness) deposition rates

(Sect.3.2). For the gas pressures typically used in LCVD, transport will be determined by two-dimensional diffusion if a tight line focus is used (Fig.4.2b), and by one-dimensional diffusion if the laser beam is unfocused or defocused.

For parallel incidence, decomposition can be based either on gas-phase heating (Sect.2.1) or on selective excitations of electronic or vibrational transitions (Sect.2.2). Clearly, excitation or dissociation of species will take place within the total volume of the laser beam.

Laser-induced gas-phase heating (parallel incidence) and laser-induced photolysis (perpendicular or parallel incidence) allow the deposition of thin films at low or moderate substrate temperatures. This is one of the most important advantages over conventional CVD, where uniform substrate temperatures of, typically, 500 - 2000 K are required. Plasma CVD (PCVD), which also allows deposition at lower substrate temperatures, is inherently associated with overall vacuum ultraviolet irradiation and heavy ion bombardment that may damage the substrate and simultaneously result in impurities being incorporated into it.

Therefore, LCP offers the unique possibility of depositing thin films onto substrates which are sensitive to elevated temperatures and/or to particle bombardment. Examples are prefabricated Si wafers, compound semiconductors and polymer foils.

In the following, pyrolytic and photolytic deposition of extended thin films will be discussed separately for metals, semiconductors and insulators. Thin film production by reactive and nonreactive laser sputtering and laser evaporation will be briefly mentioned.

5.3.1 Metals

Thin extended films of metals have been deposited mainly from the corresponding alkyls, carbonyls and fluorides. In most cases investigated, decomposition of these molecules was based on gas-phase photolysis with excimer laser or harmonics of Nd:YAG laser light. Generally, the films deposited at normal incidence have much better mechanical and electrical properties than those deposited at parallel incidence. This difference in physical properties is related to the laser-induced substrate heating which occurs at normal incidence only. However, good quality films can also be produced at parallel incidence when the substrate is preheated. This latter technique allows for proper control of the substrate temperature.

Detailed investigations on large-area metal film deposition have been performed by DEUTSCH and RATHMAN [5.26,180], in particular for W, ArF excimer

laser radiation at parallel incidence has been employed for photolytic decomposition of WF_6 in H_2. Silicon wafers and 4600 Å SiO_2/Si served as substrates. Good adherence and low electrical resistivity (about twice the bulk value) of films was achieved only when the substrate was heated to about 700 K. While this temperature would seem to be rather high, it should be noted that standard CVD of W on SiO_2 substrates is typically performed at about 1000 K. The excellent conformal coverage and surface morphology of laser-deposited W films can be seen from the scanning electron micrographs

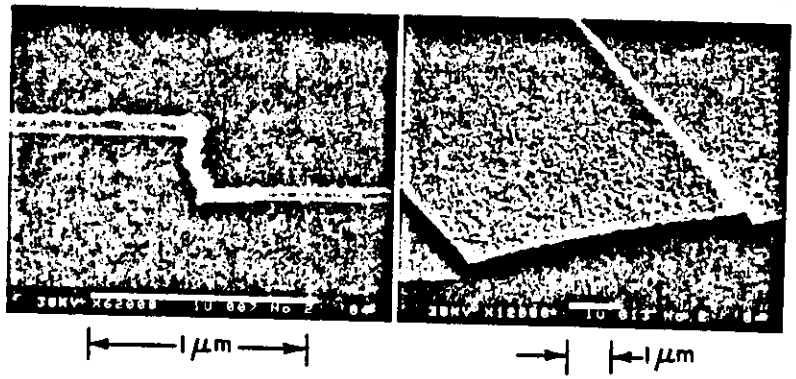

Fig.5.23. Scanning electron micrographs showing a side and top view of a W film over SiO_2 steps on a Si substrate. Deposition was performed with ArF laser radiation from a mixture of WF_6 and H_2. T_s = 560 K (after [5.26,180])

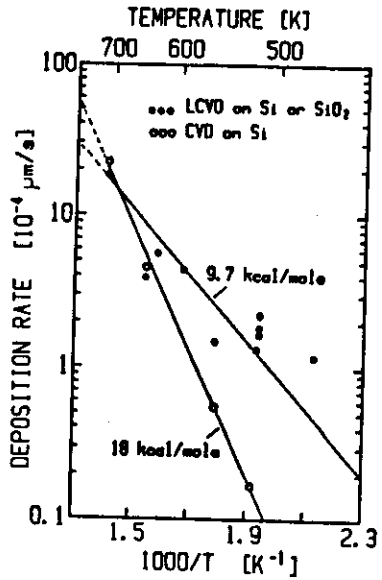

Fig.5.24. Arrhenius plot for the (thickness) deposition rate of W films. The precursor was WF_6 diluted in H_2. •: Deposited by ArF laser radiation on Si and SiO_2/Si substrates (after [5.26,180]); o: Deposited by standard CVD on Si

shown in Fig.5.23. Figure 5.24 shows an Arrhenius plot for the deposition rate. For comparison, corresponding results obtained by standard CVD of W on Si are included. The figure shows that LCVD allows deposition of W on SiO_2 at temperatures where the rates in standard CVD are negligible, and also significantly enhances the rates for Si substrates at temperatures < 600 K. Another important feature seen in the figure is the strong decrease in the apparent chemical activation energy. This clearly shows that laser light irradiation changes the path of chemical reactions involved in the deposition process. It seems remarkable that such changes in the activation energy have not been observed in pyrolytic LCVD.

The following reaction mechanism was suggested: In the initial step the 193 nm ArF excimer laser radiation produces WF_n (n = 1-5) radicals. The F atoms released can react with H_2 in a strongly exothermic reaction according to

$$H_2 + F \longrightarrow HF + H \,. \qquad (5.5)$$

The atomic H can then react with WF_6 and WF_n radicals via a complex series of reactions that result in the deposition of W and in gaseous HF as a reaction product. Such a reaction mechanism would at least qualitatively explain the strong change in activation energy with respect to standard CVD, where the rate-limiting step in the kinetically controlled region is probably determined by the dissociation of adsorbed H_2 molecules.

The laser-deposited W films are of high purity with a concentration of F < 1%. The sharp decrease in resistivities that was observed with increasing substrate temperatures can be explained by a structural change in the W films (see also Sect.5.4). It is well known that W exhibits a small-grain metastable β-W phase which transforms into a large-grain stable α-W phase at temperatures between about 600 and 950 K.

Extended thin films of Al [5.5,6], and Cr, Mo, W [5.6,68,69] have been deposited mainly with ArF and KrF lasers from $Al_2(CH_3)_6$ and from $Me(CO)_6$ (Me = Cr,Mo,W), respectively (Table 5.1). The substrate materials were mainly Pyrex, SiO_2 and Si. With perpendicular incidence, bright silvery metallic films of reasonable quality were obtained. Most of the films showed good adhesion to the substrates (> $5.5 \cdot 10^8$ dynes/cm^2 for SiO_2 substrates). The tensile stresses were between about 10^9 and $7 \cdot 10^9$ dynes/cm^2. Films of Cr and Mo deposited at 300 K had a tendency to peel when exposed to air. This could be avoided by heating the substrate to about 420 K either during deposition or prior to removal from the cell. Except for Al, the film resistivities were about 20 times higher than the corresponding bulk values (Table 5.1). These

high film resistivities are probably due to C and C_xO_y impurities (see also Sect.5.4). Parallel laser beam irradiation led to grey or black particulate films with even higher carbon content.

Production of thin extended metal films should also be possible from the solid-phase, for example by transforming spun-on metallopolymers (Sect.5.2.4) over large areas, by using an optical configuration such as shown in Fig.4.2b.

5.3.2 Semiconductors

Thin films of semiconductors have been deposited on various substrates by laser irradiation at normal and parallel incidence (Sect.4.1). Mainly cw and pulsed CO_2 lasers, frequency-doubled Nd:YAG lasers and excimer lasers have been used in these experiments. The materials studied in most detail were Si, Ge and some compound semiconductors. The substrates used were mainly SiO_2, different types of glasses with complex composition and c-Si (Table 5.1).

a) Silicon, Germanium

By far the major part of the work has concentrated on thin films of amorphous hydrogenated Si (a-Si:H) deposited mainly by means of cw or pulsed CO_2 lasers. The most commonly used parent molecules are SiH_4 and Si_2H_6, which are often diluted with different buffer gases.

The enormous interest in a-Si:H arises from the fact that this material has become a leading candidate for low cost solar cell [5.208-212] and thin film transistor [5.210] applications. Hydrogen incorporation is necessary in a-Si, because it saturates Si dangling bonds and relieves strains, resulting in a reduced defect level and the ability to modulate the Fermi level by substitutional doping. Currently, a-Si:H is mainly produced by glow-discharge decomposition of SiH_4 or by reactive sputtering in argon-hydrogen mixtures [5.208-212]. Structurally superior amorphous films are produced by standard CVD. However, because CVD requires substrate temperatures of at least 900 K in order to obtain reasonable deposition rates, the films contain an insufficient amount of hydrogen (< 1 at. %) to achieve good electronic properties. Therefore, production of a-Si:H films by LCVD, which yields reasonable deposition rates at lower substrate temperatures, seems to be a promising alternative to the techniques currently employed.

CO_2 Laser-Induced Deposition

For CO_2 laser irradiation at normal incidence, deposition of Si on SiO_2 is dominated by pyrolysis at the gas-solid interface (SiO_2 strongly absorbs CO_2 laser light). Nevertheless, a wavelength dependence of the deposition rate that correlates with the absorption of gaseous SiH_4 was observed. This indicates that gas-phase heating is important even at normal incidence. The laser-deposited films were about 1 cm in diameter. Maximum deposition rates were about $2 \cdot 10^{-3}$ μm/s with SiH_4, and about 10 times faster with Si_2H_6 [5.149,150]. For Si_2H_6 the laser-induced threshold temperature for deposition was about 600 K.

Production of high-quality a-Si:H films with parallel incidence of the CO_2 laser light requires uniform substrate heating to, typically, 500 - 700 K. Deposition rates are much smaller than for normal incidence, even when significantly higher laser powers are used. For SiH_4, for example, typical values are $2 \cdot 10^{-4}$-$5 \cdot 10^{-4}$ μm/s. However, the uniformity of films is superior to those produced at normal incidence. Films with excellent adherence were deposited over areas up to 80 cm^2 [5.135,151,153,154,157,158,161].

Decomposition of SiH_4 seems to occur in two steps [5.213-216]. In the first step, which is considered as the rate-limiting process, SiH_2 radicals and H_2 are produced by gas-phase heating (Chap.2). This means that SiH_4 molecules are first vibrationally excited in a single-photon absorption process (indicated by *) and then transfer their energy via collisions. This first step can be schematically described by

$$SiH_4(g) + h\nu \longrightarrow SiH_4^* \longrightarrow \ldots \longrightarrow SiH_2(g) + H_2(g) \ . \qquad (5.6)$$

This initial step is especially effective if the CO_2 laser frequency matches a strong vibrational transition of the SiH_4 molecule. This has been demonstrated by tuning the CO_2 laser wavelength - at constant laser power and under otherwise identical experimental conditions - from the 10.59 μm P(20) laser line, which is strongly absorbed by the ν_4-mode of the SiH_4 molecule, to the weakly absorbed 10.22 μm R(24) laser line. The difference in the laser-induced gas-phase temperatures for these two wavelengths, measured by N_2 CARS thermometry, was about 240 K [5.149,150]. The second step depends on the silane gas pressure and the laser fluence. At high pressures and/or laser fluences, SiH_2 molecules may react homogeneously with other SiH_2 or SiH_4 molecules to produce particles within the gas phase [5.216]. At lower pressures and laser fluences, diffusion of SiH_2 molecules into the substrate dominates and a thin film of a-Si:H will grow, following the reaction

$$SiH_2(g) \longrightarrow SiH_y(s) + (1-y/2)\ H_2(g) \ , \qquad (5.7)$$

where y denotes the hydrogen concentration within the film.

possess good coherence, low pinhole density, low compressive stress, and excellent step coverage. The dielectric properties of the LCVD films, however, are not yet satisfactory. Table 5.4 summarizes some typical properties of films.

5.4 Morphology and Physical Properties of Deposits

Throughout this chapter many remarks on the morphology and the physical properties of deposits in the form of microstructures and extended thin films have been made. In this section, we shall confine ourselves to summarizing some of the common features.

Most of the materials deposited by the various techniques were polycrystalline. Epitaxial and single-crystalline growth has been demonstrated in only a very few exceptional cases (see Table 5.1). For pyrolytically deposited films, the grain sizes increase with increasing laser power. This was studied in some detail for Ni [5.50,105]. Photolytically deposited films show, in general, smaller grain sizes than pyrolytically deposited films. The adherence of films depends strongly on the substrate material, the foregoing cleaning procedure, and the laser power and wavelength. For example, good adherence was found for pyrolytically deposited Ni stripes on all substrate materials investigated, except for 1000 A a-Si/glass substrates and laser powers > 20 mW. The adherence of the Ni stripes increased with decreasing laser wavelength. Photolytically deposited films show good adherence as well and generally pass the Scotch tape test.

The electrical properties of deposits were investigated for some systems and processing conditions. This is indicated by a ρ in Table 5.1. For pyrolytically deposited metal films the resistivity decreases with increasing laser power and is typically 1 to 5 times higher than the bulk resistivity. Photolytically deposited metal films produced without substrate heating have resistivities that may exceed the corresponding bulk values by a factor of $10\text{-}10^4$. The large differences in electrical properties of pyrolytically and photolytically deposited films originate from the differences in grain sizes and, more importantly, the concentrations of impurities incorporated in the films. When films are being deposited from alkyls or carbonyls, the concentrations of C_xH_y or C_xO_y fragments, which strongly influence the electrical properties, decrease with increasing substrate temperature. This explains the superior electrical properties of pyrolytically deposited films. There are several possible ways of improving the morphology and physical

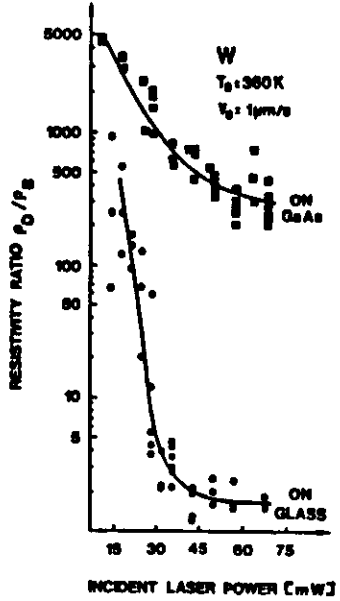

Fig.5.27. Resistivities of laser-deposited W stripes normalized to bulk values as a function of incident power of the 351-364 nm Ar^+ laser output. No buffer gas was used. The precursor gas pressure was $p(W(CO)_6) = 0.05$ mbar (after [5.103])

properties of photodeposited films. One possibility is the uniform heating of the substrate (indicated in Table 5.1 by HS) to a temperature where no dark reaction - or only a negligible one - takes place. Another possibility is the combined twin-beam or single-beam pyrolytic-photolytic technique that has been described in Sects.4.1 and 5.2.2. In this connection it may be illuminating to briefly discuss some resistivity measurements on metal stripes that have been deposited with near UV laser light.

Figure 5.27 shows, for the example of W and two different substrates, the resistivities of stripes as a function of the power of the 350-360 nm Ar^+ laser output [5.103]. The precursor was $W(CO)_6$ without any buffer gas. The most remarkable feature in the figure is the difference in resistivities of W stripes on GaAs and glass substrates. This behavior ultimately originates from the differences in the optical and thermal properties of these substrates. For example, the thermal conductivity of GaAs exceeds that of glass by a factor of 30 to 10, itself depending on the temperature. Therefore, the local laser-induced temperature at a certain laser power will be considerably lower on GaAs than on glass substrates (Sect.2.1.2). Consequently, the relative importance of pyrolytic and photolytic decomposition mechanisms will be quite different for these substrates. The lower laser-induced temperature on GaAs favors the growth of granular films

and, additionally, incorporation of photofragments, such as C, O, CO or CO_2, into the W films. This goes some way towards explaining the great differences in the resistivities. For W, however, the situation is somewhat more complicated. Here, the higher film resistivities measured on GaAs substrates may also originate, in part, from the different metallurgical phases of W that may form at different temperatures (Sect.5.3.1). Even in bulk material, the electrical conductivity of the α-phase, which is formed between 600 and 950 K, exceeds that of the β-phase by a factor of 100 to 300.

There seems to be another possible way of improving the physical properties of photodeposited films. HIGASHI and ROTHBERG [5.4] have recently shown that the CH_3 contamination within Al films photolytically deposited from $Al_2(CH_3)_6$, can be significantly reduced by subsequent ArF laser irradiation in vacuum. After irradiation, the films had similar electrical and optical properties to those deposited at elevated substrate temperatures (see [5.5] and Sect.5.3). These results seem of particular interest and should be further substantiated for other films deposited from alkyls and also from carbonyls. If this observation holds more generally, it would be a unique tool to improve the quality of both photolytically and pyrolytically deposited films. In the latter case this would be of particular relevance in high resolution pyrolytic patterning, which is achieved at low local laser-induced temperatures (Sect.3.5). It may be that the improvement of other laser-deposited materials, as e.g. Al_2O_3, by UV laser irradiation can be explained, at least in part, along similar lines (Sect.5.3.3).

6. Surface Modifications

This chapter deals with laser-induced surface oxidation, nitridation, reduction, metallization and doping. In this processing mode, atoms or molecules (including photofragments) of the adjacent medium either directly combine with atoms or molecules within the solid surface, or they simply diffuse into this surface. Another type of surface modification is the laser-induced depletion of a particular component of the surface, without appreciable etching or evaporation of the solid. In each of these treatments the physical and/or chemical properties of materials' surfaces will be modified. Surface modification, in general, requires (thermal and/or nonthermal) photoexcitation of the substrate, and is therefore performed mainly at normal incidence. Large-area surface modifications are performed with high power CO_2 lasers, excimer lasers, Nd:YAG or Nd:glass lasers, while for local modifications low power cw lasers such as Ar^+ or Kr^+ lasers may be employed.

6.1 Oxidation, Nitridation

Surface oxidation of metals and semiconductors in an oxygen-rich atmosphere is a well-known phenomenon. Clean surfaces of materials like Al, Nb, Si, etc. spontaneously react in air, even at room temperature, to form thin native oxide layers (typically 10-100 Å thick). This thermally activated process is self-terminating, because oxygen diffusion becomes less likely with increasing layer thickness. For many applications (local hardening, chemical passivation, electrical insulation, etc.), it is desirable to increase the thickness of native oxide layers, or to stimulate oxidation on material surfaces that do not spontaneously oxidize in an oxygen environment. A large number of techniques for producing oxide layers on solid surfaces have been investigated. The most commonly used such techniques are thermal oxidation by uniform substrate heating in an oxygen-rich atmosphere and plasma oxidation. Both techniques have their characteristic advantages and disadvantages, which

oxide was Ga_2O_3 + As_2O_5, the laser-formed oxide showed an oxygen deficiency in comparison with the overall formula Ga_2O_3 + As_2O_3. This behavior is not well understood.

Oxidation of various III-V compounds under high intensity visible laser light irradiation has been studied by COHEN et al. [6.23] and by FUKUDA and TAKAHEI [6.20].

Photo-enhanced oxidation of Si and InP in a N_2O atmosphere excited by ArF laser light at parallel and combined perpendicular/parallel incidence has been demonstrated by ZARNANI et al. [6.26,27]. For InP preheated to 685 K, the oxidation rate at parallel incidence was $5 \cdot 10^{-5}$ µm/s (10 mbar N_2O). The growth rate increased with increasing N_2O pressure. This shows the importance of excited oxygen, which is formed according to (2.27). Combined perpendicular/parallel irradiation increased the oxide layer thickness by about 20%. This additional enhancement is due to electron-hole pair generation and possibly also due to direct substrate heating. The composition of the oxide layers contained In_2O_3 and a phosphate, probably $InPO_4$.

c) Oxidation Mechanisms

From the existing literature it is very clear that the photo-enhanced oxidation of semiconductors under visible and UV irradiation is not a purely thermally controlled process. Nonthermal contributions are essential, particularly at low laser irradiances. It seems to be clear also that various different nonthermal mechanisms contribute to the oxidation process and that their relative importance depends on the particular system under investigation and the laser wavelength and irradiance. Among these mechanisms are:

- The migration of photogenerated electrons through the oxide layer. This may result in both the formation of oxygen anions and a strong electric field, which in turn pulls the oxygen ions through the oxide layer. The oxidation rate decreases with increasing oxide layer thickness due to the reduction in field strength. Such a field-assisted diffusion process would at least qualitatively explain the dependence of the oxidation rate, which has been investigated mainly for Si. This mechanism also seems to be essential in the Si-halogen etching reactions that are described in Sect.8.2 [6.65,65].
- For UV and for far UV laser light, the photo-induced formation of oxygen vacancies within the oxygen layer may become important [6.17-19,67,68]. Oxygen-vacancy-related defects increase the mobility and thereby the transport of the oxygen.
- Far UV radiation also increases the formation of active oxygen species (O, ozone). These can be produced either in adlayers or within the ambient

medium. Excited oxygen atoms $O(^1D)$ may directly react with semiconductor surfaces to form oxide layers [6.26,27].

Similar mechanisms are expected also for nitridation reactions.

In summary, one can say that surface oxidation and nitridation result in the formation of films with thicknesses of, typically, 0.1-1 µm. Such films can be produced either by single-step direct writing, or over extended areas of up to several square centimeters. The technique is complementary to laser-induced gas-phase deposition (Sect.5.3), which makes it possible to grow uniform films which are, typically, between 10 and 10^3 times as thick.

6.2 Reduction, Metallization

Just as laser-induced heating of certain materials in an oxygen-rich atmosphere encourages the oxygen to become incorporated in the lattice, specific materials can, in contrast, be persuaded to give up their oxygen to a reducing environment under the appropriate laser-heating conditions. This has been demonstrated for oxidic perovskites, e.g. $BaTiO_3$, $PbTiO_3$, $PbTi_{1-x}Zr_xO_3$ (PZT), $Pb_{1-3y/2}La_yTi_{1-x}Zr_xO_3$ (PLZT) and $SrTiO_3$, by BÄUERLE and co-workers [6.69-73]. These materials are insulators with a band gap of, typically, 3 eV. They are ferroelectric and thereby piezoelectric. It is well known that the physical properties of these materials can be dramatically changed by oven heating of the bulk material, e.g. in H_2 atmosphere at 500 - 1500 K [6.74-79]. This treatment results in the generation of oxygen vacancies and free or quasi-free electrons. The concentration of oxygen vacancies and free electrons increases with increasing reduction temperature and with decreasing oxygen partial pressure. The oxygen vacancies act as shallow donor levels and the originally insulating material becomes an n-type semiconductor. The originally transparent material becomes blue to black, depending on the concentration of vacancies [6.74,75]. Because of the fundamental role of the oxygen ion in connection with the dynamical properties of perovskites, the oxygen vacancies also strongly influence the structural phase transitions (ferroelectic and nonferroelectric) observed in these materials [6.76-83].

Laser light irradiation of oxidic perovskites in a reducing atmosphere can result in local reduction of the material surface [6.70-73,84]. While for sub-band-gap radiation ($h\nu < E_g$) the reduction mechanism is mainly thermal, UV and far UV radiation ($h\nu > E_g$) may directly generate oxygen vacancies and quasi-free electrons. The reduction process is reversible, i.e. on heating the material in an O_2 atmosphere or in air, the reduced (blue to black)

Fig.6.2. Optical micrograph of stripes produced with laser powers P = 75 mW, 125 mW and 190 mW (left to right). The scanning velocity was v_s = 25 µm/s and the hydrogen pressure $p(H_2)$ = 500 mbar. The distance between centers of stripes is 200 µm (after [6.72])

regions vanish. Only a small change in surface morphology is observed. With increasing laser irradiance the degree of reduction increases and the electrical properties of laser-treated regions change from semiconducting to metallic. When the laser intensity is even further increased, beyond a certain value, etching or cutting of the material is observed (Sect.8.3).

Laser-induced reduction and metallization of oxidic perovskites allows single-step conductive patterning of the otherwise insulating materials' surfaces. Metallization has been studied in detail for hot-pressed optically transparent ferroelectric PLZT ceramics [with 9.5 at. % La (y = 0.095) and a Zr:Ti ratio of 65:35 (x = 0.35)] by KAPENIEKS et al. [6.72,73]. The electrical resistivity of the bulk material was > 10^{14} Ωcm.

Figure 6.2 shows an optical micrograph of metallic stripes produced with increasing power (from left to right) of the UV multiple line output of a Kr^+ laser (λ = 337-356 nm) on the surface of a transparent PLZT sample. After laser treatment the sample was rinsed in dilute HNO_3 in order to remove the Pb condensed near the edges of the stripes.

In Fig.6.3, the resistivity per unit length of stripes is plotted versus laser power. The different symbols refer to a freshly prepared sample and a sample annealed at about 1100 K. Initially, both samples show an approximately exponential decrease in resistivity with increasing laser power, and then a decrease in slope in the semilogarithmic plot. For laser powers above about 180 mW, microcracks are occasionally observed in the surface region adjacent to the metal stripe. These cracks have no influence on the electrical conductivity of the stripes. However, when the laser power is increased to above 250-300 mW, cracks that penetrate deeply into the bulk PLZT material underneath the metallic stripe are observed. Therefore, this regime was not investigated in any more detail. The single data points shown in the figure for the same laser power were obtained from resistivity measurements on the same stripe, but for different locations of electrodes. The scattering of data is probably due to inhomogeneities in the transformed material, which may possibly be related to inhomogeneities in the bulk material. The results presented in the following were all obtained with freshly prepared samples.

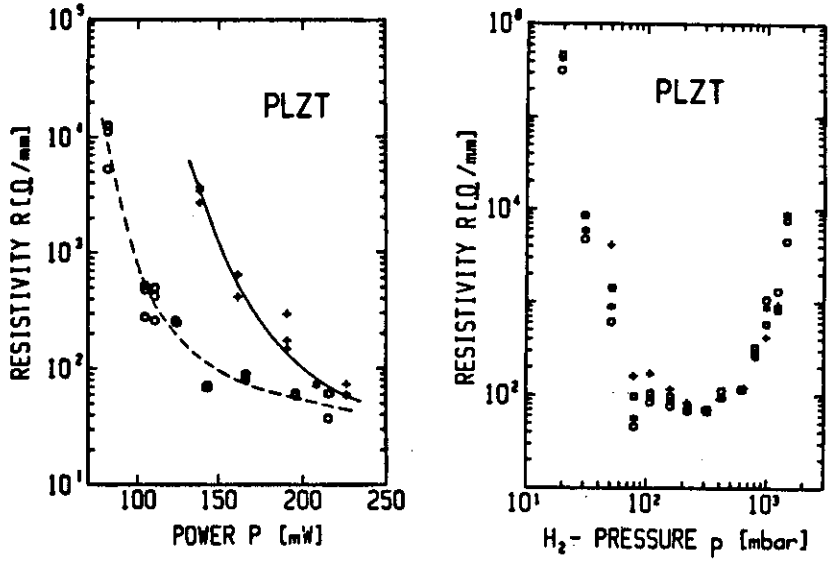

Fig.6.3. Resistivity of laser-processed stripes as a function of laser power with v_s = 25 µm/s and $p(H_2)$ = 500 mbar. o: PLZT 9.5/65/35 freshly prepared; +: Sample annealed at 1100 K (after [6.72])

Fig.6.4 Resistivity of laser-processed stripes as a function of H_2 pressure. P = 200 mW, v_s = 25 µm/s. o: Resistivity measured immediately after laser processing and Cu electrode evaporation; ▪: Resistivity after 20 h; □: After 50 h; +: After annealing the sample at 373 K for 1 h (after [6.72])

Figure 6.4 shows the resistivity of stripes as a function of H_2 pressure for different time intervals of resistivity measurements. Here, each data point represents an average of five resistivity measurements. A pronounced minimum in resistivity for pressures between about 100 and 600 mbar can be observed. It can be seen that ageing influences the resistivity of stripes produced at lower H_2 pressures more strongly than those produced at higher pressures. The dependence of the resistivity of stripes on the scanning velocity is shown in Fig.6.5. Again, a sharp minimum is observed for a certain range of scanning velocities, at otherwise constant parameters. The change in resistivity is about 5 orders of magnitude on both sides. For scanning speeds below about 10 µm/s, scanning electron micrographs show many cracks in the stripes. This explains the broad scattering of data points in this region. At higher scanning velocities, no cracks can be observed and the reproducibility of measurements is within about a factor of two. This is quite satisfactory in view of the wide range of resistivities that can be obtained for different processing parameters.

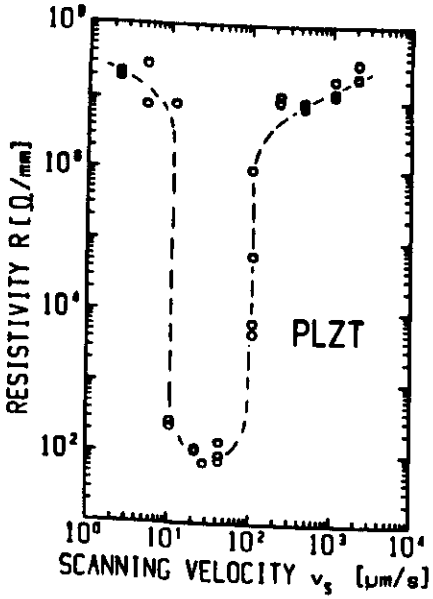

Fig.6.5. Resistivity of stripes as a function of scanning velocity. P = 190 mW, $p(H_2)$ = 500 mbar (after [6.72])

From the foregoing results it has become evident that ranges of optimal processing parameters exist, for which the resistances of stripes are typically of the order of 100 Ω/mm. In these ranges of processing parameters, the stripes have metallic conductivity. This can be concluded from a simple estimate of the specific resistivity of the stripes, which yields values of about 10^{-4} Ω cm.

The conductivity of metallized regions within PLZT surfaces produced by UV laser irradiation in H_2 atmosphere is essentially determined by: the reduction of the material to metallic Pb, Ti and Zr, the evaporation of Pb and, for certain parameters, the cracking of stripes. The evaporation of Pb results in the occurrence of a shallow groove in the middle of the metallic stripe. This local depletion of Pb is consistent with X-ray microanalysis and similar investigations performed on $PbTi_{1-x}Zr_xO_3$ [6.71]. The dependencies of the resistivity shown in the figures can be qualitatively understood in the light of the aforementioned points: An adequate processing time ($\sim 1/v_s$) and a sufficient amount of H_2 are necessary for the metallization of the PLZT surface. On the other hand, if v_s is too small, an increase in Pb evaporation and a subsequent cracking of stripes is observed (Fig.6.5). For high H_2 pressures the mean free path of the evaporating Pb is diminished and the dense Pb vapor attenuates the laser beam intensity. This causes the increase in resistance (Fig.6.4).

The increase in power threshold observed for annealed samples (curve indicated by + symbols in Fig.6.3) can be understood from the shift in band edge caused by the annealing. This shift in band edge is a well-known phenomenon in PLZT. In fact, one can see that the characteristic yellowish color of freshly prepared PLZT is faded out in annealed samples. Because the energy of the laser light is only near the band-gap energy of the PLZT, a small shift in the band edge to higher energies will cause a significant change in absorbed laser power.

Large-area electrodes (0.5x0.5 cm^2) have been prepared in a similar way on PLZT surfaces. These electrodes were characterized by temperature-dependent dielectric measurements performed on samples with different thicknesses (0.1-2 mm) at frequencies from 10 kHz to 10 MHz [6.73,120]. Below 400 K the laser-fabricated contacts led to higher dielectric constants than conventional evaporated Au electrodes. The difference is most pronounced for small sample thicknesses. Thus, in combination with the observed increase in adherence, such laser-processed electrodes could be superior to conventional electrodes in miniaturization problems.

6.2 Doping

This section deals with the doping of semiconductor surfaces. It does not, however, contain any material on the deposition of doped semiconducting films, as this has already been discussed (Chap.5). Laser-induced doping of materials' surfaces takes advantage of the high heating and cooling rates that can be achieved with pulsed lasers or scanned cw lasers (Sect.2.1.1). The short temperature cycles obtained with lasers make it possible to produce very shallow heavily doped layers within solid surfaces. While pulsed lasers are mainly used for large-area (sheet) doping, cw lasers allow direct writing of patterns with lateral dimensions down to the submicrometer level (Sect.4.2). Table 6.2 lists the systems investigated so far.

Laser doping is, in general, performed at normal incidence. The absorbed fluence must be high enough to substantially heat or even melt a thin layer of the substrate surface in order to allow dopant incorporation by high temperature or liquid-phase diffusion. The source of dopant atoms may be a thin layer of an element implanted into or evaporated onto the substrate surface, or adsorbed-, gas-, liquid-, or solid-phase parent molecules, which are photothermally or photochemically decomposed by the laser light. Therefore, laser doping often involves two simultaneous steps: heating or melting of the substrate surface and photodecomposition of the parent

8.3 Inorganic Insulators

Etching of inorganic insulators has been investigated mainly for amorphous SiO_2 (a-SiO_2; often simply denoted by SiO_2), for some glasses of complex composition, for oxidic perovskites such as $BaTiO_3$, $SrTiO_3$, $PbTi_{1-x}Zr_xO_3$, and for ceramic Al_2O_3/TiC (Table 8.1).

8.3.1 SiO_2 - Glasses

Photochemical dry-etching of SiO_2 and SiO_2-rich glasses has been investigated for various reactant molecules that have been dissociated either by single-photon electronic or by multiphoton vibrational excitations. For the molecules investigated, spontaneous etching is zero or negligible (Sect.8.1).

BRANNON [8.59] and LOPER and TARAT [8.65-67] used ArF and KrF excimer lasers to photodissociate CF_2Cl_2, CF_2Br_2 and CF_3Br, CF_3I, CF_3NO and $CO(CF_3)_2$. Interestingly, etching was very efficient for CF_2Cl_2 and CF_2Br_2 (typical etch rates were 0.2-0.5 A/pulse), while the other compounds yielded either very inefficient etching or else none at all. These results seem to suggest that CF_2 radicals interact with the SiO_2 surface more strongly than CF_3 radicals. The reason for the different behavior of these radicals is not understood and the results need to be further verified. Experiments carried out under similar conditions, but with Br_2 and SF_6 as parent gases did not yield any appreciable etching. HIROSE et al. [8.29,30] have investigated the etching of SiO_2 in a mixture of NF_3 and H_2 under ArF excimer laser irradiation. The reaction mechanism suggested was qualitatively described by

$$SiO_2 + NF_3 + H_2 + h\nu(193\ nm) \longrightarrow SiF_4 + NO_2 + N_2O + HF\ . \qquad (8.10)$$

Here, the etch rate was found to increase with H_2 partial pressure. The main reaction products observed were SiF_4, N_2O and NO_2.

Etching of SiO_2 in a Cl_2 atmosphere by visible Ar^+ laser radiation has been investigated by CHUANG et al. [8.8,9,79,80]. Because SiO_2 is transparent within the visible spectral region, laser-induced excitation or heating of the substrate cannot be of great importance. In fact, the etch rate seems to be correlated with the photodissociation yield of the Cl_2 (Sect.2.2.1). For 457.9 nm radiation an etch rate of up to $3\cdot10^{-4}$ µm/s [$p(Cl_2)$ = 133 mbar] was obtained, while the rate was significantly lower for the 514.5 nm laser line, under otherwise identical experimental conditions. The lateral dimensions of etched features were much larger than the focal spot size. For example, for $2w_0$ = 7 µm the diameter of the holes was 50-80 µm, depending on the laser

beam illumination time. This can be explained by the random diffusion of Cl radicals produced within the gas phase (Sect.3.5).

Large-area etching of SiO_2 activated by multiphoton vibrational dissociation (MPD) of CF_3Br and CDF_3 with pulsed CO_2 laser radiation has been reported by STEINFELD et al. [8.86,87]. Because of the high laser intensities necessary for MPD, such experiments can be performed only in the parallel configuration (Fig.4.3). The etch rate achieved with the laser focus 1 mm above the substrate was 0.3 A/pulse. It was proposed that the CF_3 radicals generated in the MPD process react with SiO_2 to form volatile products. This interpretation is in disagreement with the results mentioned above. It remains unclear whether the different observations are related to the differences in optical configuration, photochemistry and/or concentrations of radicals generated in both experiments.

Projection etching of SiO_2-rich glasses by transient heating in a H_2 atmosphere has been demonstrated with ArF laser radiation [8.58]. Gratings with a resolution of about 0.4 µm have been produced. Figure 8.16 shows the etched depth as a function of laser fluence for Pyrex and thermally grown SiO_2 on Si.

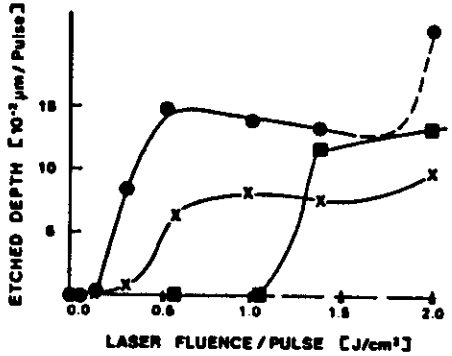

Fig.8.16. Etched depth of various different glasses in H_2 atmosphere as a function of ArF laser fluence. Pyrex: ●: $p(H_2)$ = 266 mbar; x: $p(H_2)$ = 1333 mbar. SiO_2 on Si: ■: $p(H_2)$ = 266 mbar (after [8.58])

8.3.2 Perovskites

Laser-induced etching of oxidic perovskites has been investigated by EYETT et al. [8.14,103-106]. Experiments were performed with visible and UV Ar^+ and Kr^+ laser radiation and with excimer laser radiation. As outlined in Sect.6.2, laser-induced heating of these materials in a reducing atmosphere results in the formation of oxygen vacancies and quasi-free electrons. With increasing laser powers, metallization and, finally, etching occur. The most-detailed investigations on etching have been performed for crystalline

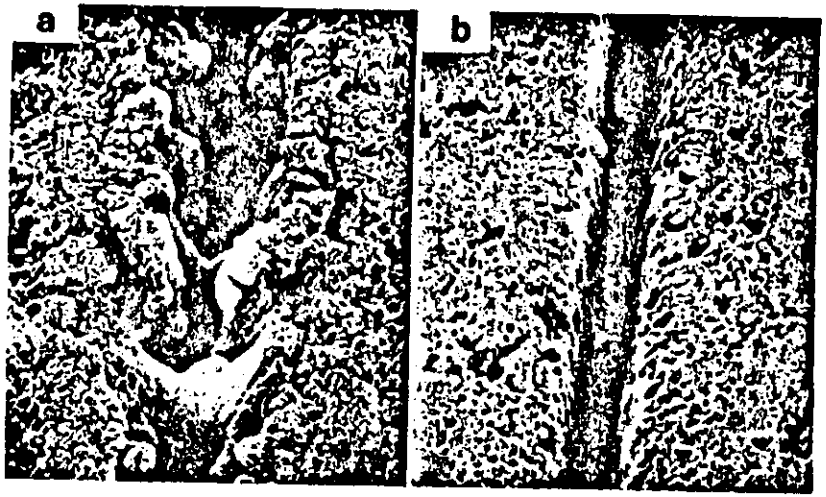

Fig.8.17a,b. Scanning electron micrographs of grooves etched with 647 nm Kr^+ laser radiation in ceramic $PbTi_{1-x}Zr_xO_3$. The ambient medium was (a) air with p(air) = 90 mbar, (b) H_2 with $p(H_2)$ = 90 mbar. P = 0.72 W, $2w_0$ = 18 µm, v_s = 8.4 µm/s (after [8.14])

$BaTiO_3$ and $SrTiO_3$ and for ceramic $BaTiO_3$ and $PbTi_{1-x}Zr_xO_3$ (PZT, PXE) in an H_2 atmosphere. Scanning electron micrographs of grooves produced in PZT with 647 nm Kr^+ laser radiation in air and in an H_2 atmosphere under otherwise identical processing conditions are compared in Figs.8.17a,b. While materials removal in air is very irregular, well-defined structures can be produced in H_2. Additionally, etching thresholds are considerably lower in H_2 than in air. The role of H_2 is interpreted by the local decrease in O_2 partial pressure, which favors efficient local reduction of the material (see Sect.6.2). This has two consequences:

- The local absorption increases strongly and becomes spatially better defined.

- The large number of oxygen vacancies generated favors a local collapse of the perovskite lattice.

Figure 8.18 shows the width and depth of grooves and holes as a function of laser power. The illumination time for the holes was chosen to be equal to the dwell time of the laser beam during etching of grooves, i.e. $t_d = 2w_0/v_s$. For low laser powers, the width is approximately equal to the diameter of the laser focus. For the highest laser powers used, the width increases by a factor of two to three. The etched depth increases continuously but shows a decreasing slope with increasing laser power. The latter observation may

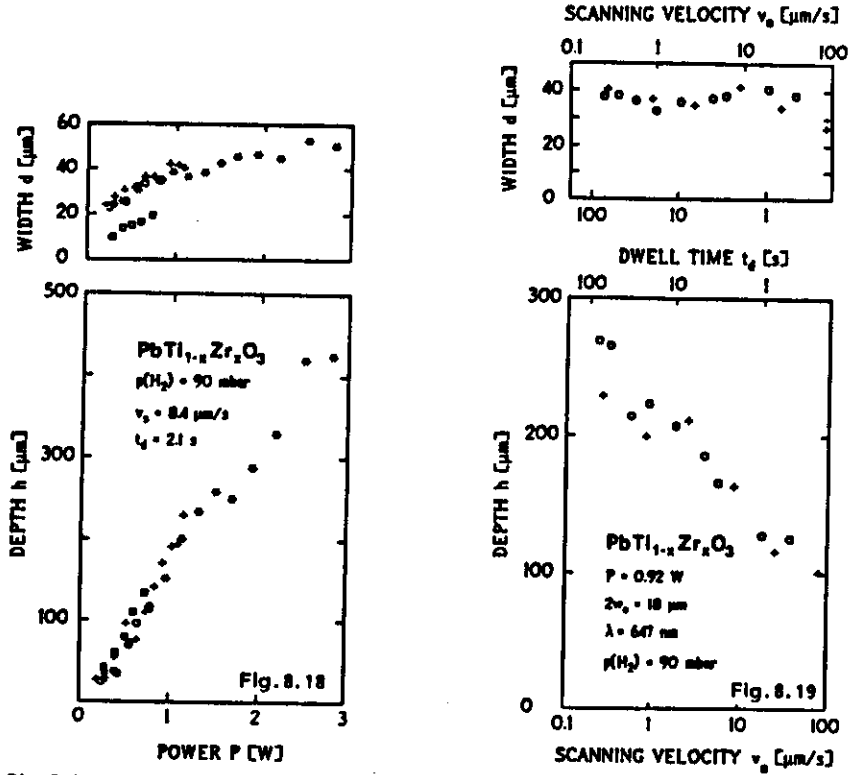

Fig.8.18. Width and depth of grooves and holes etched in ceramic $PbTi_{1-x}Zr_xO_3$ as a function of the incident Kr^+ laser power. +: grooves, $2w_0$ = 18 µm, λ = 647 nm, v_s = 8.4 µm/s. •: grooves, $2w_0$ = 18 µm, λ = 488 nm, v_s = 8.4 µm/s. □: grooves, $2w_0$ = 11 µm, λ = 647 nm, v_s = 8.4 µm/s. o: holes, $2w_0$ = 18 µm, λ = 647 nm, t_d = 2.1 s (after [8.14])

Fig.8.19. Width and depth of grooves and holes etched by 647 nm Kr^+ laser radiation in $PbTi_{1-x}Zr_xO_3$ in a H_2 atmosphere as a function of scanning velocity and laser beam dwell time. +: grooves; o: holes (after [8.14])

result from the diminution of the effective laser power by the material ejected out of the etched groove or hole. At constant power, the etched width stays about constant while the depth increases logarithmically with the dwell time of the laser beam (Fig.8.19). Temperature measurements using visual and photoelectric pyrometry (Sect.4.4) revealed an Arrhenius type behavior of the average etching depth. For temperatures < 1600 K, an apparent activation energy of 41 ± 8 kcal/mole was derived. In this connection it seems interesting to note that the energies of evaporation of pure PbO [8.107] and

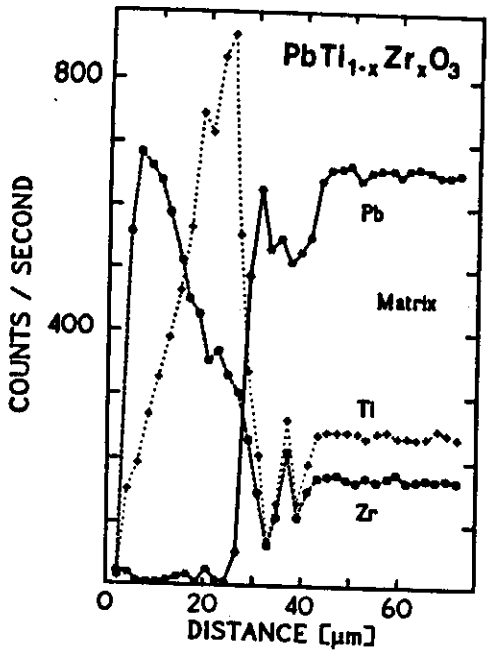

Fig.8.20. Electron-beam-induced X-ray fluorescence signal for Pb, Ti and Zr as a function of the distance from the groove edge. The measurements were made near the surface of the sample, on a V-shaped cross section similar to that shown in Fig.2.9c (after [8.14])

of PbO out of $PbTi_{1-x}Zr_xO_3$ (x = 0.65) [8.108] are 56 kcal/mole and 39 kcal/mole, respectively. The corresponding energies of evaporation of TiO_2 and ZrO_2 are 137 and 170 kcal/mole, respectively [8.107]. This is a hint that the evaporation of PbO is important in the etching process. This conclusion is supported by SEM and electron-beam-induced X-ray fluorescence studies. In a region of about 30-50 μm around the edges of grooves or holes, morphology changes are observed, which are due to a depletion of Pb (Fig.8.20). Beyond the depletion layer, the morphology and chemical composition corresponds to that of bulk PZT. The thickness of the depletion layer depends on the incident laser power. Results similar to those presented in Figs.8.18 and 19 were obtained for the other perovskites investigated.

The etching conditions became quite different, however, when UV laser radiation with an energy exceeding the band-gap energy, E_g, of the perovskite under consideration was used instead of visible laser radiation. Initial experiments were performed with the 337-356 nm multiple line output of the

Kr^+ laser. Up to the highest laser powers available (P < 400 mW), the etch rates were in good agreement with those presented in Fig.8.18, but they were independent of the surrounding atmosphere (H_2 or air). These results can tentatively be explained by the strong increase in the absorption coefficient for photon energies $h\nu > E_g$. Furthermore, experiments with 308 nm XeCl laser radiation have shown that the depletion layer mentioned above can be considerably reduced or even avoided [8.106].

8.4 Organic Polymers

Laser-induced ablation of organic polymers and biological materials can be performed in a vacuum or in a nonreactive atmosphere. As already outlined in Sect.3.4, the process is mainly thermally controlled for IR and visible laser radiation, while direct nonthermal bond breaking seems to dominate for UV radiation below about 200 nm at low to medium laser irradiances. While this section deals mainly with the processing of organic polymers, the technique can be applied also to biological materials that have similar properties.

Table 8.2 summarizes the results currently available on the etching of organic polymers. It can be seen that most of the experiments have been performed in air. Systematic investigations on the influence of a reactive surrounding on the etch rates are still lacking.

Pyrolytic ablation of polymers and biological materials is based on local melting and/or evaporation. The local laser-induced temperature rise can be estimated from the equations presented in Sect.2.1.1. Due to their temperature sensitivity, organic materials become, in general, heavily damaged and/or distorted during pyrolytic processing. While this may be irrelevant in particular applications, such as in large-area cutting for example, the technique does not allow well-defined patterning in the sub-millimeter region. The following discussion will therefore concentrate on *photochemical ablation* (APD). This technique, which opens up a wide variety of new and quite different applications, not only in materials processing but also in medicine, was pioneered by SRINIVASAN and co-workers [8.112-114,116,119,120,125,128-130].

Figure 8.21 shows scanning electron micrographs of two polymers, PMMA and Riston (Du Pont Riston™ is a negative photoresist, which consists of PMMA and other acrylates), that have been irradiated with ArF laser light through mechanical masks. The relatively sharp edges and the high aspect ratios achieved are typical of APD.

- passive reaction system
- diffusive reaction system

Spontaneous Etching

→ etching occurs even without irradiation
→ enhancement due to irradiation
→ example : Al – Cl_2 (Chuang et al.)

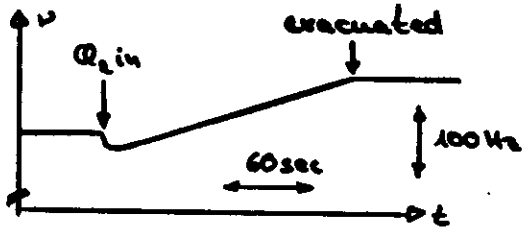

p = 0.013 mbar Cl_2
no irradiation

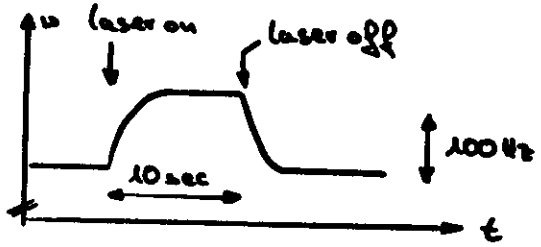

no Cl_2
with laser

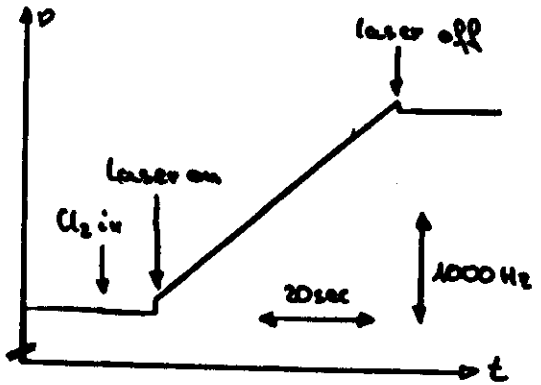

p = 0.013 mbar Cl_2
λ = 337 nm N_2
Φ = 0.12 J/cm²

→ increase p and Φ :

λ = 308 nm XeCl
Φ = 0.3 J/cm²
p = 1.3 mbar

} ω = 30 Å/pulse
= 18 µm/min
at 100 Hz

Passive Reaction Systems

→ formation of a thin passivating layer
typical thickness : 30 Å
→ irradiation : enhanced formation
removal of this surface layer
→ examples : Si , Fe , Mo

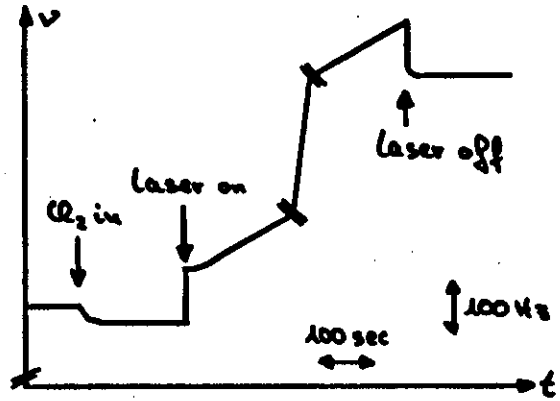

Fe – Cl_2
λ = 337 nm N_2
Φ = 0.12 J/cm²
p = 0.13 mbar Cl_2

→ etch rate ~ vapour pressure of
reaction products

Diffusive Reaction Systems

→ halogen atoms penetrate deeply into the bulk of the solid

→ example : $Ag - Cl_2$

- formation of $AgCl_x$, $0 \leq x < 1$
- $x \to 1$ at long exposures (10^{10} L)
- penetration depth : several 100 Å
- irradiation :
  - generation of Cl atoms (UV light)
  - enhancement of Cl diffusion
  - desorption of AgCl

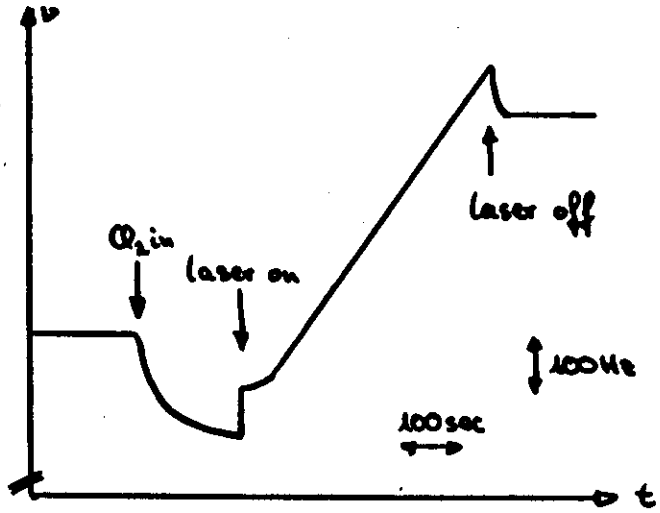

(Chuang et al.)

p = 0.13 mbar Cl_2
λ = 337 nm N_2
Φ = 0.12 J/cm²

Laser-induced chemical dry etching of semiconductors

i) investigated systems

ii) microscopic mechanisms

iii) Si + Cl_2

Laser-induced chemical dry etching of semiconductors

i) investigated systems

ii) microscopic mechanisms

iii) $Si + Cl_2$

Investigated Systems

semiconductors:	etch gases:
Si	Cl_2, Br_2
	XeF_2, SF_6
	COF_2, CF_4, NF_3
	HCl
Ge	Br_2
GaAs	Cl_2, Br_2
	CCl_4, $SiCl_4$
	CF_3Br, CF_3I
	CH_3Br, CH_3Cl
	HBr, HCl
InP	CF_3I
	CH_3Br, CH_3Cl
	CCl_4

Pyrolytic Processes

→ perpendicular incidence

→ absorption of light by
- electron-hole pair generation (VIS, UV)
- free carrier absorption (IR)

→ thermalization between photocarrier system and lattice : ~ 1ps

→ recombination of electron-hole pairs
- Auger recombination : ps ... µs
- surface recombination, recombination via traps, radiative recombination : µs ... ms

→ heating of the lattice : ps ... ns

Effects due to heating:

→ dissociation of parent molecules at the heated surface

$GaAs + CCl_4$ (Takai et al.)

→ diffusion of halogen atoms into the lattice, bond breaking

$Si + Cl$ (this work)

→ desorption of reaction products

$SiCl_4$, SiF_4 : high vapour pressure at T = 300 K

→ $W = W_0 \cdot e^{-\frac{\Delta E}{RT}}$

(Arrhenius law)

Photolytic Processes

→ perpendicular or parallel incidence

→ excitation of gas phase molecules
- electronic excitation, dissociation
  $Cl_2 \longrightarrow 2\,Cl$, $\lambda < 500\,nm$
  $Si + Cl \longrightarrow \ldots$ (Ehrlich et al., this work)
- vibrational excitation
  $SF_6 \longrightarrow SF_6^*$, $\lambda = 10.6\,\mu m$
  $Si + SF_6^* \longrightarrow \ldots$ (Chuang)

→ electronic excitation of the semiconductor
- electron-hole pair generation
- formation of Cl^- or F^- ions
- penetration of ions into the lattice, bond breaking

  Si + Cl (Arikado et al., this work)
  Si + F (Houle et al.)
  GaAs + Cl (Ashby)

→ excitation of the semiconductor - adsorbate system

$2\,SiF_2\,(ads) \longrightarrow Si + SiF_4\uparrow$

$\lambda = 10.6\,\mu m$ (Chuang)

→ $W \sim I^{\gamma}$, $\gamma = 0.3 \ldots 3.5$

- electrons in the conduction band
- photoelectrons
- n-doped material

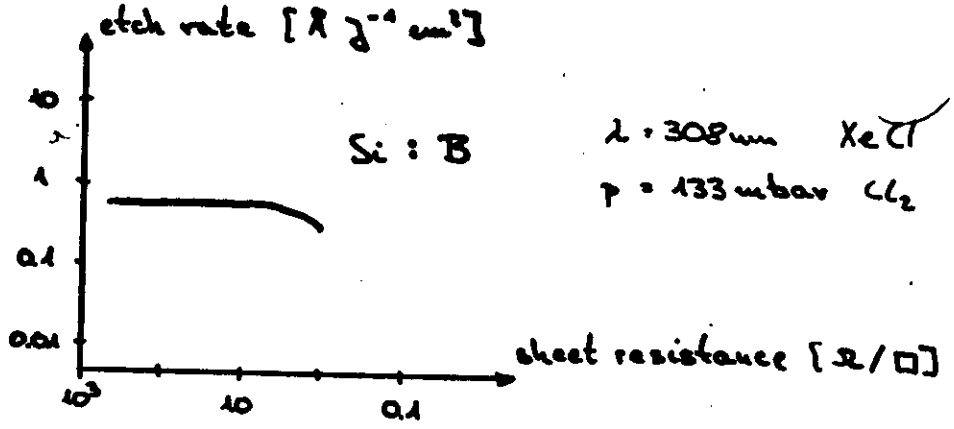

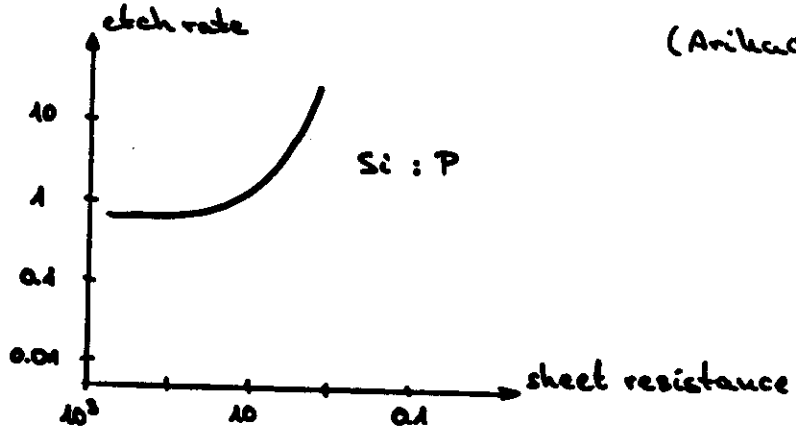

(Arikado et al.)

$Si + Cl_2$

Experimental Setup:

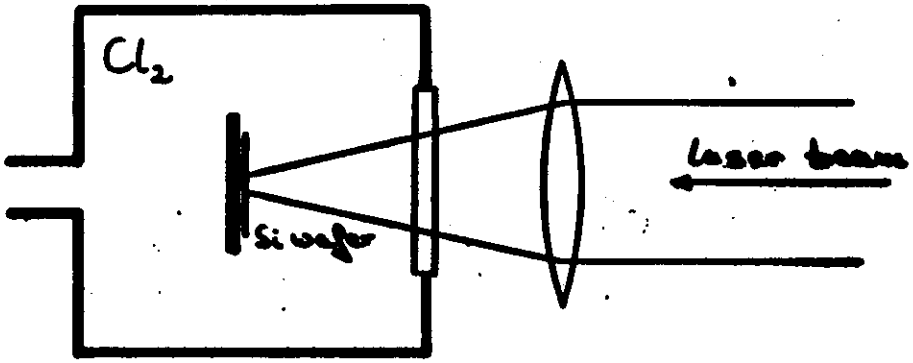

- lasers : excimer laser , 308nm XeCl
  dye laser , 423nm , 583nm
- spot size : 150 · 500 μm^2
  energy densities : $\leq 1.2\ J/cm^2$
- chlorine pressure : $\leq$ 100mbar
- silicon : lightly p-doped
  (100 ... 400 Ω cm)
  100 orientation

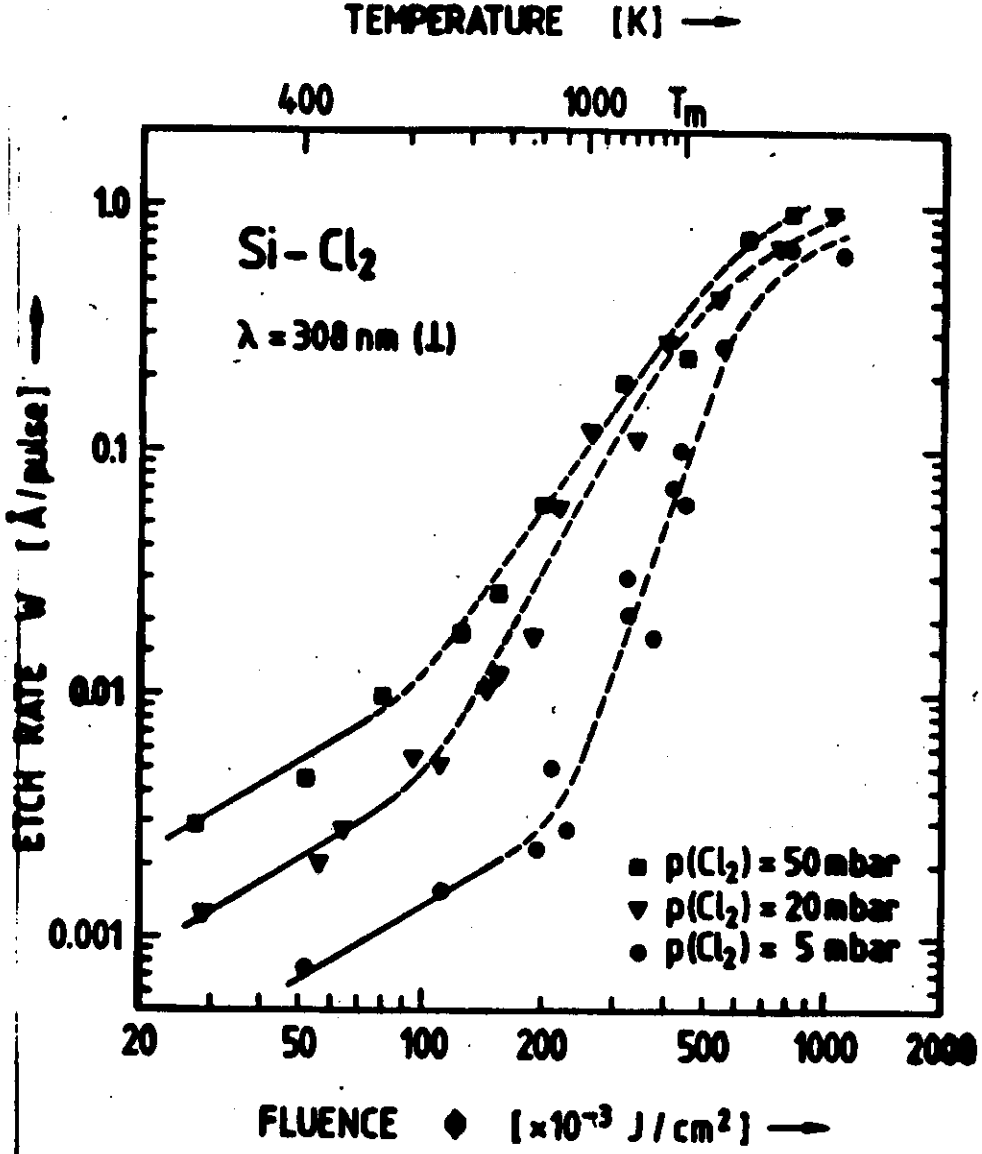

Temperature Calculations

→ one - dimensional calculation

→ heat equation:

$$\frac{\kappa(T)}{D_t(T)} \cdot \frac{\partial T}{\partial t} - \frac{\partial}{\partial z}\left(\kappa(T) \cdot \frac{\partial}{\partial z} T\right) = Q(z,t)$$

$$Q(z,t) = S + I(t) \cdot (1 - R(t)) \cdot \alpha(T) \cdot \exp\left(-\int_0^z \alpha(T(z'))\, dz'\right)$$

→ numerical solution

- material parameters from the literature
- important : temporal pulse profile

$\lambda = 308\,nm$: $\Phi_m = 440\ mJ/cm^2$, $\tau = 11\,ns$

$= 423\,nm$: $= 250\ mJ/cm^2$, $= 7\,ns$

$= 583\,nm$: $= 280\ mJ/cm^2$, $= 11\,ns$

(FWHM)

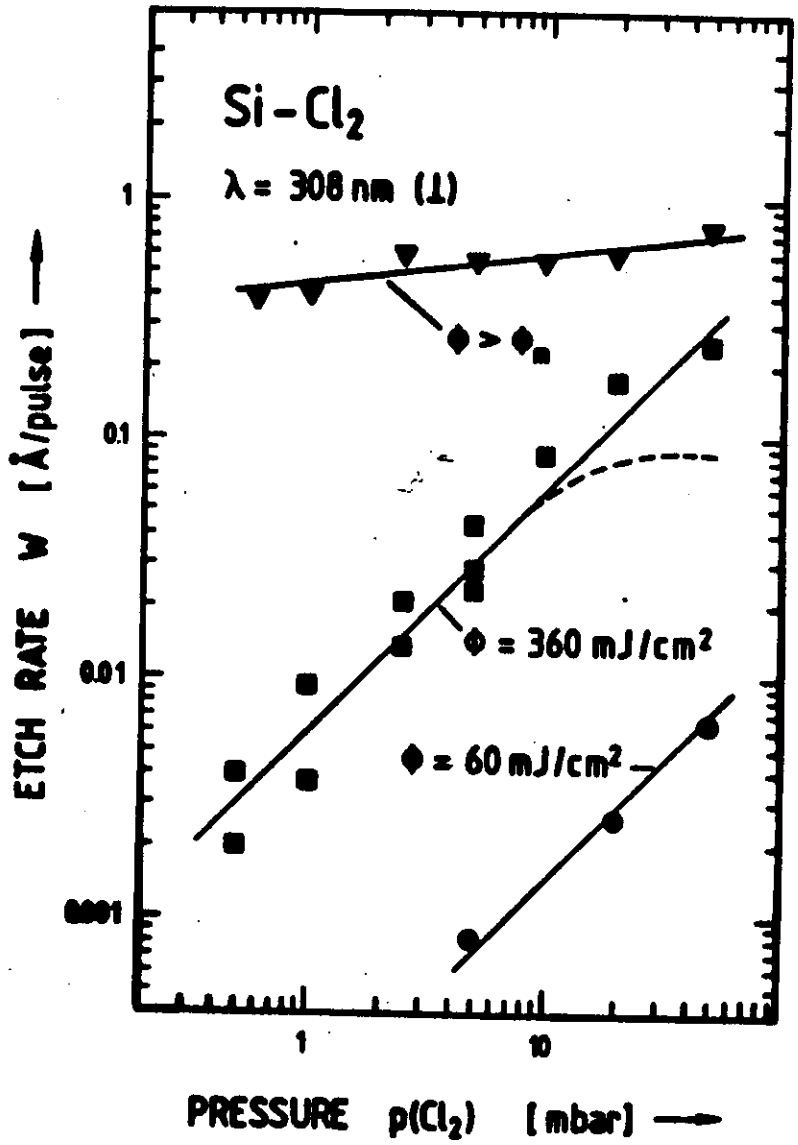

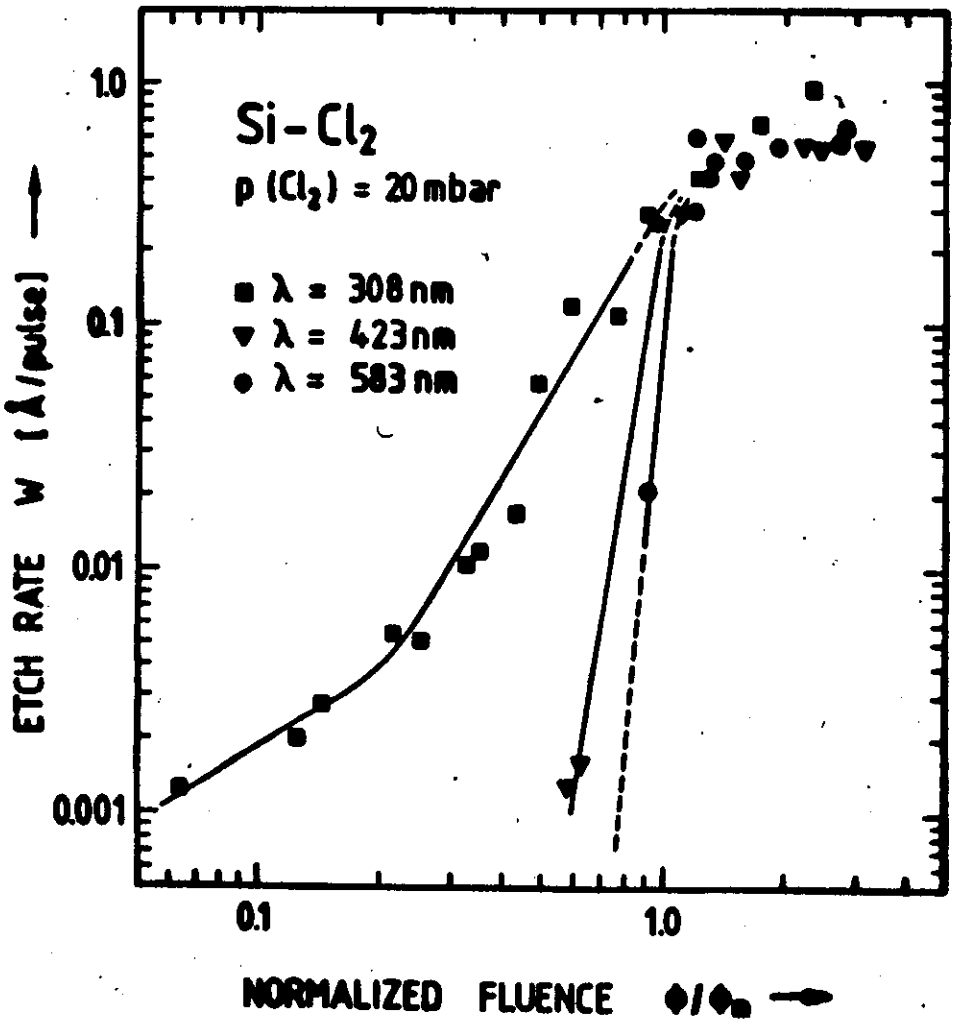

combined irradiation scheme:

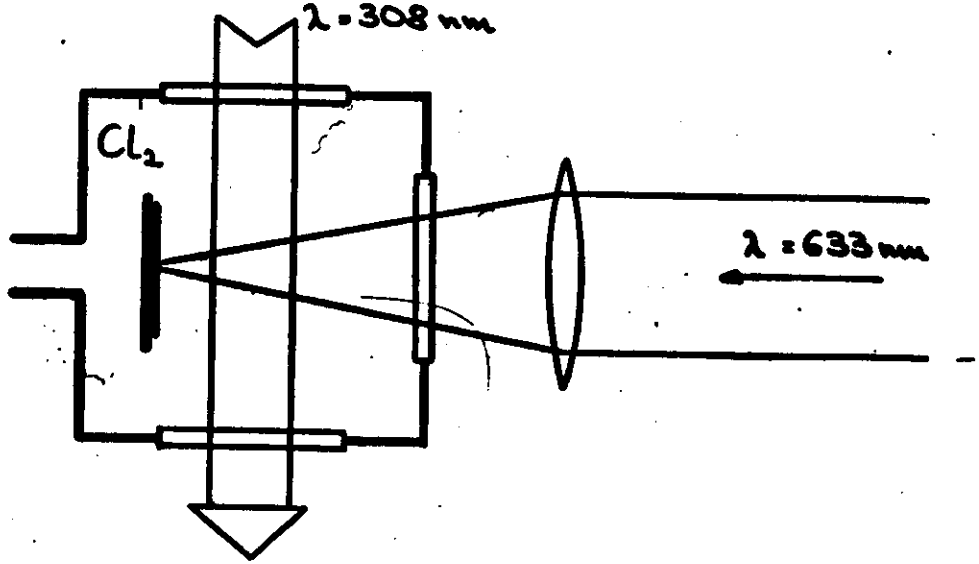

→ photolytic process

→ etch rate increases with
- chlorine atom density
- HeNe laser intensity

→ chlorine atoms in the gas phase
+ photocarriers in the semiconductor
→ etching

Perpendicular irradiation at $\lambda = 308\,nm$:

low laser fluences:

→ high carrier densities n_e
- → Auger recombination
- → $n_e \sim \sqrt[3]{I(t)}$ during the laser pulse

after the pulse: n_e almost independent of laser fluence Φ

→ chlorine atom flux up to ~ 100 ns after the laser pulse essential recombination of Cl atoms: ~ ms

→ chlorine atom flux: $\sim \Phi$

carrier density n_e: slightly dependent on Φ

→ $\omega \sim \Phi$

medium laser fluences:

→ pyrolytic contribution
- facilitates Cl atom penetration into the lattice and Si-Si bond breaking
- thermal desorption of SiCl
- reduced photocarrier diffusion, carrier confinement

Conclusion

$T < T_m$: necessary to etch Si with Cl_2
- Cl atom generation in the gas phase
- excitation of silicon
  - photolytical
  - pyrolytical

$T > T_m$: pyrolytic process involving adsorbed chlorine species